

THESIS / THÈSE

DOCTOR OF SCIENCES

Giant planet dynamical evolution in binary star systems

ROISIN, Arnaud

Award date:
2021

Awarding institution:
University of Namur

[Link to publication](#)

General rights

Copyright and moral rights for the publications made accessible in the public portal are retained by the authors and/or other copyright owners and it is a condition of accessing publications that users recognise and abide by the legal requirements associated with these rights.

- Users may download and print one copy of any publication from the public portal for the purpose of private study or research.
- You may not further distribute the material or use it for any profit-making activity or commercial gain
- You may freely distribute the URL identifying the publication in the public portal ?

Take down policy

If you believe that this document breaches copyright please contact us providing details, and we will remove access to the work immediately and investigate your claim.



UNIVERSITY OF NAMUR

FACULTY OF SCIENCES

NAXYS RESEARCH INSTITUTE

DEPARTMENT OF MATHEMATICS

Giant planet dynamical evolution in binary star systems

Thesis presented by
Arnaud Roisin
for the title
of Doctor of Science

Composition of the Jury:

Aurélien CRIDA
Anne LEMAITRE (President of the Jury)
Anne-Sophie LIBERT (Advisor)
Sean RAYMOND
Jean TEYSSANDIER
Kleomenis TSIGANIS

June 2021

Cover design: ©Presses universitaires de Namur
©Presses universitaires de Namur & Arnaud Roisin
Rue Grandgagnage, 19
B-5000 Namur (Belgium)

Cover picture: Courtesy NASA/JPL-Caltech

Reproduction of this book or any parts thereof, is
strictly forbidden for all countries, outside
the restrictive limits of the law, whatever
the process, and notably photocopies or scanning.

Printed in Belgium.

ISBN: 978-2-39029-146-6

Registration of copyright: D/2021/1881/15

University of Namur
Faculty of Sciences
Rue de Bruxelles, 61
B-5000 Namur (Belgium)

Giant planet dynamical evolution in binary star systems

by Arnaud Roisin

Abstract: The growing population of planets discovered in orbit around one stellar component of a binary system has diverse eccentricities. These discoveries raise the question of their formation and long-term evolution because the stellar companion can strongly affect the planet formation process. In this work, by means of a symplectic integrator designed for binary star systems, we study the dynamical influence of a wide binary companion on the evolution of giant planets during their migration in the protoplanetary disk and their long-term evolution after the dispersal of the disk. In particular, we highlight the importance of the Lidov-Kozai resonance for highly inclined binary companions. In the first part, the effects of the disk gravitational potential and the disk nodal precession induced by the binary companion are discussed. In the second part, the mean motion resonance captures of the planets during the migration phase are studied. We finally show how our work can explain several features of the detected circumprimary planets, such as the high eccentricities and the spin-orbit misalignment.

Evolution dynamique des planètes géantes dans les étoiles binaires

par Arnaud Roisin

Résumé : De plus en plus de planètes évoluant autour d'une étoile d'un système binaire sont découvertes, la plupart d'entre elles avec des excentricités très variées. Ces découvertes soulèvent la question de la formation et de l'évolution à long terme de ces planètes car le companion stellaire peut fortement influencer le processus de formation. Dans ce travail, au moyen d'un intégrateur symplectique développé pour les systèmes binaires, nous étudions l'influence dynamique d'un companion binaire éloigné sur l'évolution de planètes géantes durant leur migration dans le disque protoplanétaire et leur évolution à long terme après la dissipation du disque. En particulier, nous soulignons l'importance de la résonance de Lidov-Kozai pour les companions binaires très inclinés. Dans la première partie, les effets du potentiel gravitationnel et de la précession nodale du disque induite par le companion binaire sont discutés. Dans la deuxième partie, les captures en résonance en moyen mouvement des planètes pendant leur phase de migration sont étudiées. Nous montrons finalement comment notre travail peut expliquer plusieurs caractéristiques des planètes circumprimaires détectées, telles que leurs excentricités élevées et le désalignement spin-orbite.

Ph.D. thesis in Mathematics

Date: 28/06/2021

naXys Research Institute, Department of Mathematics

Advisor: Anne-Sophie LIBERT

*"Does the flap of a butterfly's wings in Brazil
set off a tornado in Texas?"*

EDWARD LORENZ, 1972.

Remerciements

Voici venu le moment d'ajouter la touche finale à ce travail. Ces quelques lignes me permettront d'exprimer ma gratitude envers toutes les personnes qui m'ont fait grandir et ont permis à ce manuscrit d'être ce qu'il est aujourd'hui. Au moment de me plonger dans cette rétrospective, j'espère n'oublier personne.

Je ne pensais pas en arriver là. En particulier, il y a deux ans lorsqu'au sommet du découragement, j'exprime à ma promotrice, Anne-Sophie Libert, mon hésitation à demander mon renouvellement permettant la poursuite de mon doctorat. Ce jour-là, ses mots sont parvenus à me remotiver et à me redonner confiance. Je souhaite la remercier pour son implication dans ma thèse, ses conseils avisés, ses encouragements, ses nombreuses relectures, sa patience, sa gentillesse, sa disponibilité et sa capacité à me focaliser sur les éléments essentiels afin d'éviter les dispersions. Sans elle, ce manuscrit n'existerait pas et ne serait pas ce qu'il est aujourd'hui.

Dans un second temps, je souhaite remercier les membres du jury ayant évalué ce travail. Je pense tout d'abord à Kleomenis Tsiganis, à ses conseils avisés et à sa bienveillance lors de nos discussions. Son équipe et lui-même m'ont accueilli à bras ouverts à Thessalonique pour un stage inoubliable dans le cadre de mon master. Ma gratitude va également à Jean Teyssandier pour notre collaboration ayant débouché sur une publication, ses remarques judicieuses et l'ensemble des réponses qu'il a apportées à mes nombreuses questions. Il a fait preuve de patience et de pédagogie à mon égard. Je souhaite remercier Anne Lemaître d'avoir accepté de présider le jury ainsi que pour ses remarques constructives et l'ensemble des fautes de frappe qu'elle a identifiées. Ses encouragements et ses mots chaleureux le jour de la présentation privée m'ont déstressé. Je suis également reconnaissant à Aurélien Crida d'avoir accepté de faire partie de mon comité d'accompagnement, pour les discussions lors de nos différentes rencontres et pour l'ensemble de ses remarques avisées.

Enfin, je tiens à remercier Sean Raymond d'avoir accepté d'évaluer ma thèse ainsi que pour ses commentaires pertinents. Sa passion lors de ses présentations en summer school pousse à aimer la science et l'astronomie.

J'exprime ma reconnaissance à Sotiris Sotiriadis pour nos discussions sur SyMBA, pour le partage de son travail et pour ses réponses à mes innombrables questions. Il a toujours répondu avec beaucoup de patience et de gentillesse.

Je pense également à ma fructueuse et agréable collaboration avec Mara Volpi ayant engendré une publication comme point d'orgue. Par ailleurs, j'ai éprouvé un réel plaisir à voyager en sa compagnie dans le cadre de conférences ou de summer schools. Sa bonne humeur contagieuse rendait ces séjours particulièrement agréables.

Je ne peux regarder en arrière sans penser au département de mathématique de l'Université de Namur. Il y règne une réelle ambiance familiale où il fait bon vivre en l'absence d'épidémie! C'est toujours un plaisir de partager un moment avec un de ses membres au détour d'un couloir, à l'arsenal ou en salle café. Les secrétaires du département, Alice et Pascale, lui permettent de tourner rond et y facilitent la vie. Merci à Juan pour ses conseils, ses dépannages et son aide avec le cluster. Je ne peux remercier le département sans citer Morgane, Pauline, Julien, Jon, Jérémy, Martin, Alexis, Eve, Ambi, Delphine, Anthony, Riccardo, Manon, François et Joanna avec qui j'ai passé de merveilleux moments que ce soit lors des repas à l'arsenal, des belottes ou lors des soirées lorsqu'elles étaient encore permises!

Je pense également à ma famille et en particulier à mes parents, ma grand-mère, mon frère et Mélanie qui m'ont toujours soutenu et poussé à donner le meilleur de moi-même. Leur présence est un point d'ancrage dans ma vie. Il en va de même pour l'ensemble de mes amis, en particulier Guillaume, Alex, Alice, Sam, Marie, Emilie et Gaëtan qui m'ont permis de passer des moments de détente, de décompresser et de profiter de la vie en oubliant un peu le travail. Merci à Christine et Didier pour le cadre de travail agréable lors du confinement et la relecture de dernière minute.

Une pensée particulière également pour Nicolas avec qui j'ai eu la chance de partager mon bureau. J'ai éprouvé un réel plaisir lors de nos discussions, il a toujours le mot pour rire, un regard avisé sur le sport et une bonne humeur communicative.

Enfin, je remercie Candy pour son soutien, pour l'acceptation de mes longues soirées et nuits de travail l'ayant laissée seule, pour les moments de rire, pour notre complicité, pour tout ce qu'elle est. Sans elle, je ne serais pas aussi épanoui et je n'aurais pas pu arriver jusqu'ici avec sérénité.

Contents

Introduction	1
Contributions	3
Fundings	3
Notation	5
I Preliminary	7
1 Binary star systems	9
1.1 Binary stars	9
1.2 Exoplanets in binary stars	12
1.2.1 Discoveries	12
1.2.2 Distribution	14
1.3 Formation	15
1.3.1 Star formation	16
1.3.2 Planetary system formation	17
1.3.3 Migration	19
1.3.4 Influence of a binary companion	23
1.4 Conclusions	24
2 Symplectic integrator for binary stars	27
2.1 Symplectic integrator	27
2.1.1 Definition	27
2.1.2 Construction	29
2.1.3 Splitting in three parts	32

2.1.4	SyMBA	33
2.1.5	Adaptation to binary stars	35
2.2	Migration code	43
2.2.1	Giant planet migration	44
2.2.2	Influence on the eccentricity and inclination	44
2.2.3	Disk model	47
2.3	Conclusions	48
II One-planet systems		49
3	Evolution of a migrating giant planet in the presence of an inclined binary companion	51
3.1	Introduction	51
3.2	Set-up of the simulations	52
3.3	Results	53
3.3.1	Lidov-Kozai resonance	53
3.3.2	Final distributions	56
3.3.3	Initial conditions leading to Lidov-Kozai resonance	58
3.4	Dynamical analysis	59
3.5	Discussion and conclusions	65
4	Planetary migration in precessing disks	69
4.1	Introduction	69
4.2	Additional effects	70
4.2.1	Disk gravitational potential	70
4.2.2	Disk nodal precession caused by a binary companion	72
4.3	Simulations	81
4.3.1	Parameter set-up	82
4.3.2	Typical example	83
4.3.3	Results	83
4.4	Conclusions	88
III Two-planet systems		91
5	Resonance captures in binary star systems	93
5.1	Introduction	93
5.2	Wide binary stars	94
5.2.1	Simulation set-up	94
5.2.2	Typical examples	95
5.2.3	Parameter distributions	98

5.3	Importance of the Lidov-Kozai effect for two-planet systems . .	110
5.3.1	State of the art	110
5.3.2	Second set of simulations	112
5.3.3	Parameter distributions for $a_B = 250$ AU	113
5.3.4	Limitations of the model	119
5.4	Comparison with observations	120
5.5	Conclusions	122
	Conclusions and Perspectives	125
	A Chaos detector for planetary systems	127
	Bibliography	149

Introduction

For several decades now, human beings have been looking for new habitable planets to find extraterrestrial life or a new home if the conditions for life on Earth continue to deteriorate. Some interest was given to the nearest star to the Sun, Proxima Centauri. It was discovered that this celestial body is one star of the triple star system Alpha Centauri and has two confirmed exoplanets. Nowadays it is estimated that about half of the Sun-like stars are part of multiple star systems. This raises the question of the influence that could have a binary companion on the evolution of planets in binary star systems. Up to now, more than 100 planets have been found orbiting around a star holding a binary companion, allaying our concerns about the strong inhibition that could have a binary companion on the formation of planets.

Planetary formation is a complex and not yet fully understood process that could be disturbed in many stages by a binary companion. During the growing phase of the planetary embryos, the binary companion could lead to a speed increase of the particles resulting in disruptive collisions. The late-stage accretion of terrestrial planets can be disturbed by the binary companion during the collision phase of planetary embryos. The binary companion could also destabilize the planetary system during the migration phase of fully formed planets in the protoplanetary disk.

In this thesis we aim to study the influence of a wide binary companion on the migration of giant planets embedded in a protoplanetary disk. We will pay a particular attention to the so-called Lidov-Kozai resonance that could be induced by the binary companion on the planets. This work is achieved using a symplectic integrator which allows us to study the long-term dynamics of the system, when the protoplanetary disk is dissipated.

The thesis is divided in three parts. In the first one, we briefly review the knowledge about the binary stars and the planets they host discovered

so far. We also introduce some generalities about the formation of planetary systems and we highlight the influence that could have a binary companion on the formation process. In the second chapter, we detail the N -body code developed in this work to study the migration of giant planets in binary star systems.

The second part of the thesis is devoted to the evolution of a single giant planet in a protoplanetary disk. In Chapter 3, we study the influence of the binary companion during the migration phase and the establishment of Lidov-Kozai resonant systems after the dispersal of the disk. Additional physical effects, namely the nodal precession caused by the binary companion on the disk and the disk gravitational potential acting on the planet, are studied in detail in Chapter 4, as well as their impact on the previous results.

The third part deals with systems of two giant planets migrating in the disk. In Chapter 5, we aim to see how the mean-motion resonance captures are impacted by the binary companion. We also explore the final configurations of the planetary systems, long after the disk phase, and analyze our results in light of the characteristics of the planets detected in binary stars. Finally we draw our conclusions and discuss some perspectives.

Contributions

- Binary star systems
 - Roisin, A., and Libert, A.-S., *Evolution of a migrating giant planet in the presence of an inclined binary companion*, *Astronomy & Astrophysics*, 645, A138, 2021, Chapter 3 of the thesis.
 - Roisin, A., Teyssandier, J., and Libert, A.-S., *Planetary migration in precessing disks for S-type binaries*, submitted to *Monthly Notices of the Royal Astronomical Society* in April 2021, Chapter 4 of the thesis.
 - A paper based on Chapter 5 is currently in preparation.
- Single star systems
 - Volpi, M., Roisin, A., and Libert, A.-S., *The 3D secular dynamics of radial-velocity-detected planetary systems*, *Astronomy & Astrophysics*, 626, A74, 2019, Appendix A of the thesis.

Fundings

The PhD thesis was supported by a F.R.S.-FNRS research fellowship. Computational resources have been provided by the Consortium des Equipements de Calcul Intensif, supported by the FNRS-FRFC, the Walloon Region, and the University of Namur (Conventions No. 2.5020.11, GEQ U.G006.15, 1610468 and RW/GEQ2016).

Notation

	Symbol	Meaning
Parameters	a	Semi-major axis
	e	Eccentricity
	i	Inclination
	ω	Argument of the pericenter
	ϖ	Longitude of the pericenter
	Ω	Longitude of the ascending node
	λ	Mean longitude
	M	Mean anomaly
	n	Mean motion
	P	Orbital period
	m	Mass of a body
	m_{sys}	Total mass of the system
	m_{red}	Reduced mass of the system i.e. the mass of the primary star and the planets
	\mathbf{p}	Momenta
	\mathbf{q}	Generalized coordinates
	\mathbf{x}	State vector
	\mathcal{H}	Hamiltonian
	I_n	Identity matrix of order n
	0_n	Null matrix of order n
	\mathbf{r}	Position vector
	\mathbf{v}	Velocity vector
	\mathbf{a}	Acceleration vector

	τ_{mig}	Type-II migration timescale
	τ_{ecc}	Eccentricity damping timescale
	τ_{inc}	Inclination damping timescale
	τ_{LK}	Lidov-Kozai timescale
	τ_{pl}	Planetary interaction timescale
	α	Shakura-Sunyanev viscosity parameter
	h	Aspect ratio of the gas disk
	Σ	Radial surface density of the gas disk
	R_{in}	Inner edge of the gas disk
	R_{out}	Outer edge of the gas disk
	m_{ld}	Local mass of the gas disk
	m_{disk}	Total mass of the gas disk
	r	Distance to the central star
	$b_{3/2}^{(1)}$	Laplace coefficient of the first kind
	$b_{3/2}^{(2)}$	Laplace coefficient of the second kind
	q	Planetary mass ratio
	W	Complex inclination
Units of Measure	AU	Astronomical unit
	yr	Year
	M_{\odot}	Solar mass
	M_{Jup}	Jupiter mass
	$^{\circ}$	Degree
Operator	$\{\cdot, \cdot\}$	Poisson bracket
	T	Linear operator
Abbreviations	CH	Canonical heliocentric
	WB	Wide binary
	LK	Lidov-Kozai
	GP	Gravitational potential
	NP	Nodal precession
	MMR	Mean motion resonance

Part I

Preliminary

Chapter 1

Binary star systems

This chapter provides an overview of the binary star systems hosting a planet, through a description of the characteristics of the binary stars, the distribution of the parameters of the planets as well as the key steps of their formation.

1.1 Binary stars

Today, it is estimated that about half of the Sun-like stars are part of multiple-star systems (Duquennoy and Mayor, 1991; Raghavan et al., 2010). The simplest multiple stars are binary stars that consist of two stars interacting significantly through gravitation. The classification of the binary stars is related to the detection method used (see, e.g., Benacquista, 2012). Note that a binary star could be detected through several methods and therefore belong to multiple categories.

The *visual binaries* are binary stars that are observable with the naked eye or through optical telescope. They should not be confused with double stars that seem close in the sky through the perspective but are actually far from each other and not gravitationally related as shown in Fig. 1.1. A second type of binary stars corresponds to *astrometric binaries* noticed through the gravitational perturbation of their motion, as illustrated in Fig. 1.2. Another type of binary stars is the *spectroscopic binaries* that are spotted thanks to the shift in their light spectrum induced by the Doppler effect. Indeed, when a star is moving toward us, we observe a blueshift while a redshift is observed when the star is moving away. This effect is illustrated in Fig. 1.3. The last type is called *eclipsing binaries* which are detected by the passing of one of the two

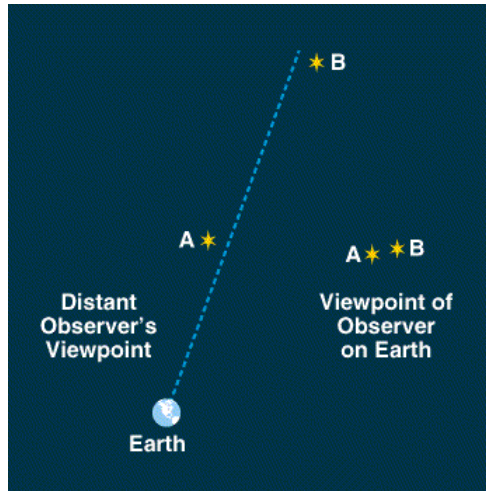


Figure 1.1 – Non-binary double star. Source: https://sites.ualberta.ca/~pogosyan/teaching/ASTRO_122/lect13/lecture13.html

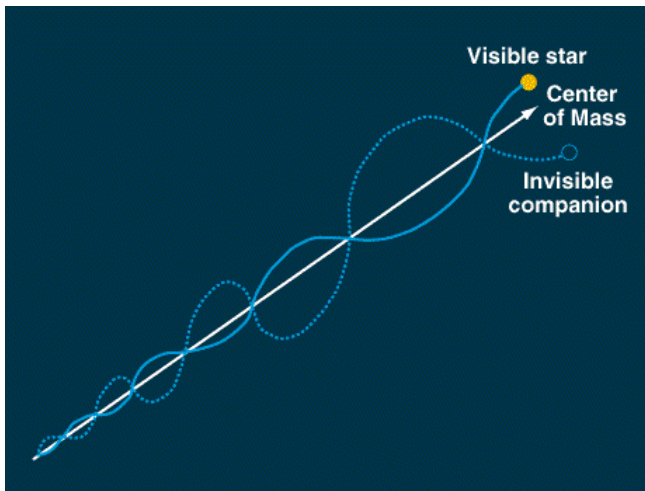


Figure 1.2 – Astrometric binaries. Source: https://sites.ualberta.ca/~pogosyan/teaching/ASTRO_122/lect13/lecture13.html

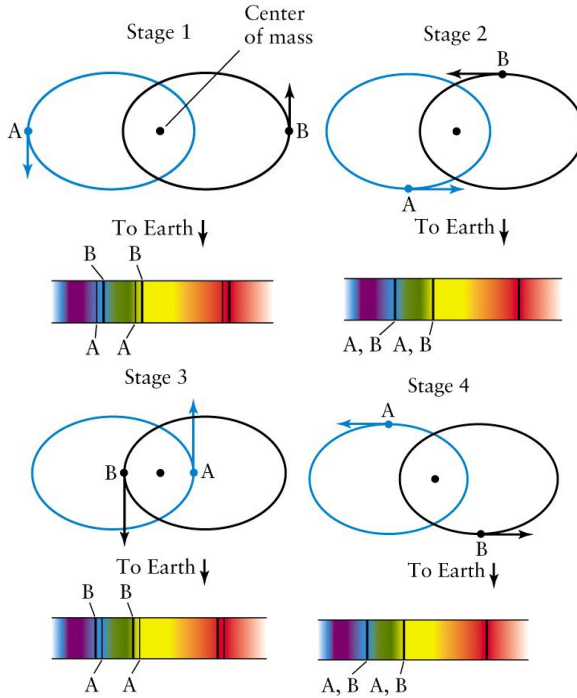


Figure 1.3 – Spectroscopic binaries. Source: https://sites.ualberta.ca/~pogosyan/teaching/ASTRO_122/lect13/lecture13.html

stars in front of the other one leading to a decrease of the light emitted by the eclipsed star. This effect is illustrated in Fig. 1.4.

Note that through their life, stars can be part of a binary star only for a given period of time. Due to an external perturbation, a binary star system could be destabilized into single stars or two single stars could suffer from a close encounter and become gravitationally linked.

A distinction between the binary stars is also made on the separation between the two stars of the binary. If the separation is above a certain value, the binary is called a *wide binary* and if not, a *close binary*. Note that the limit is still under debate. Another way proposed to make the distinction is the analysis of the influence of the binary companion on the motion of the primary star. The influence could even lead to exchange in material. If the interaction is strong, the binary is considered as a close binary, and reversely.

In this work, we will focus on wide binaries with a separation higher than 500 AU. Nevertheless the influence of the binary companion on the planets hosted by the primary star is non-negligible, as we will illustrate in this work.

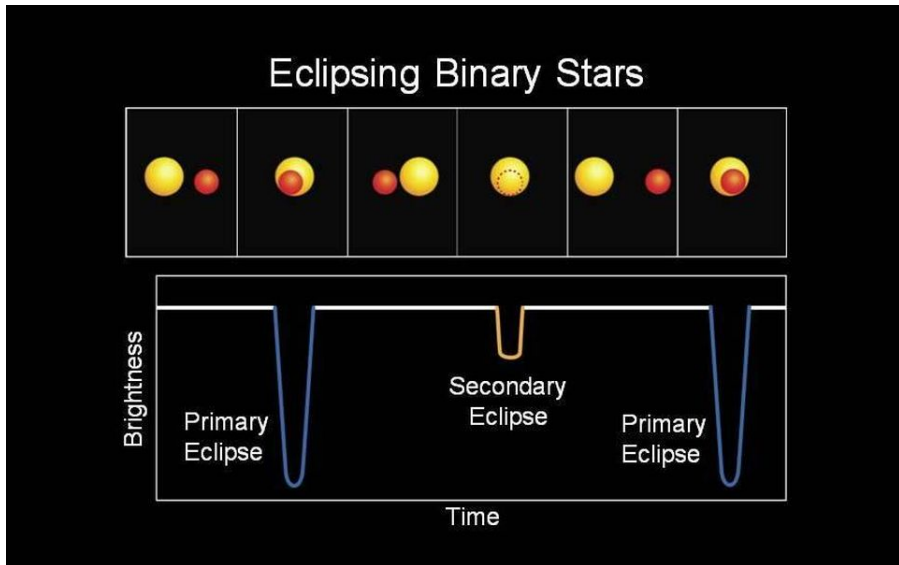


Figure 1.4 – Eclipsing binaries. ©NASA (<https://www.nasa.gov>)

1.2 Exoplanets in binary stars

There are two main types of planets in binary stars, namely the *S-type* (also called circumprimary planet) and *P-type* (also called circumbinary planet). The first one consists in planets moving around one component of the binary star while the second one in planets moving around the two components of the binary star (see Fig. 1.5). In this work, we will focus on S-type planets and we will denote by primary star the component of the binary star hosting the planets.

In this section we describe the extrasolar planets detected in binary stars and discuss their discoveries as well as the distribution of their orbital elements.

1.2.1 Discoveries

Since the first discoveries of giant planets in binary stars during the past decade (e.g., GL86 (Queloz et al., 2000), γ Cephei (Campbell et al., 1988; Hatzes et al., 2003)), their number continues to increase, and today more than 100 S-type planets are known moving around one stellar component (Schwarz et al., 2016). Most of these planets are found in wide binaries with separations larger than 500 AU. Giant planets in wide binaries have slightly higher eccentricities than around single stars (Kaib et al., 2013) and some reported eccentricities are even higher than 0.85.

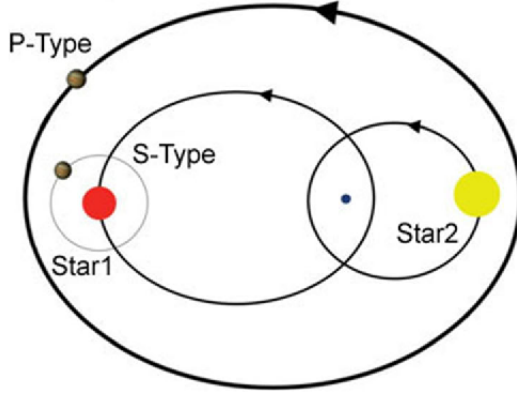


Figure 1.5 – P-type and S-type planets. Source: Schwarz et al. (2016)

Note that the physical and orbital parameters of these planets are subject to observational biases. Indeed, most of the S-type planets in binary stars have been discovered using the transit or the radial-velocity method, as for exoplanets in general. The *transit method* consists in a decay of the star light when the planet passes in front of it, as illustrated for eclipsing binaries in Fig. 1.4, which can be estimated, if we neglect the light flux coming from the transiting body, through

$$\frac{\Delta F}{F} = \left(\frac{R_p}{R_s} \right)^2 \quad (1.1)$$

with F the light flux from the star, ΔF its variation, R_p the radius of the transiting body, and R_s the radius of the observed star. As an example, the relative variation of the solar light flux induced by Jupiter, the Earth and Mars would be $\sim 1.1 \times 10^{-2}$, 8.4×10^{-5} , and 3×10^{-5} , respectively. The spatial telescopes reach nowadays a precision of $\sim 5 \times 10^{-5}$ for TESS and 2×10^{-5} for CHEOPS. Note that the transit method requires the transiting body, the star and the astronomer to be aligned. The probability of such a geometric configuration is given by (see, e.g., Winn, 2010)

$$p_t = \frac{R_s + R_p}{a} \frac{1 + e \sin \omega}{1 - e^2}, \quad (1.2)$$

where a , e and ω are the semi-major axis, eccentricity and longitude of the pericenter of the transiting body. Thus the transit method favors the detection of planets close to their star. More details about this method can be found in Deeg and Alonso (2018). The transit method deduces the size of the planet by comparing the light curve before and during the transit and isolating the quantity in Eq. (1.1). Furthermore, the semi-major axis is deduced from the

period of revolution (i.e., the time between two transits) using the third Kepler law in the case of a single planet system. The *radial velocity method* uses, as for spectroscopic binaries, a shift in the light spectrum of the host star induced by the motion of the star around the center of mass of the system. A well known quantity associated with this technique is the semi-amplitude of the radial velocity K which is given by

$$K = \frac{m_p \sin i}{(m_p + m_s)^{2/3} \sqrt{1 - e^2}} \left(\frac{2\pi G}{P} \right)^{1/3}, \quad (1.3)$$

where i is the (unknown) inclination of the orbital plane of the planet with respect to the plane of the sky, G is the gravitational constant, m_p the mass of the planet, m_s the mass of the star, and P the orbital period of the planet. As an example, the radial velocity semi-amplitude induced by Jupiter and the Earth on the Sun are of order 12m/s and 0.09m/s, respectively. The current detectable limit is reached by ESPRESSO and is of order 0.1m/s. More details about this method can be found in Wright (2018). For both methods, there will be some biases. For example, using the radial velocity method, one will only determine a minimum mass of the planet. Actually, as can be deduced from Eq. (1.3), the mass has to be scaled by the factor $\sin(i)$. On the other hand, using the transit method, it will not be possible to determine the mass and the eccentricity of a single planet, but the radius of the planet will be deduced contrary to the previously discussed method. However, for multi-planet (near-)resonant systems, the planetary masses and eccentricities could be inferred by using TTVs (transit timing variations), which consist in variations in the transit period caused by the gravitational interactions between the planets. More details about this technique can be found in Agol and Fabrycky (2018). Finally, combining both detection methods proves to be interesting to constrain the planetary masses and thus the density of the planets.

1.2.2 Distribution

Using the catalog of Rein (2012) which contains more than 4400 exoplanets (up to 2021), we analyze the distribution of the 187 S-type planets among the 225 planets detected in binary star systems. Their planetary masses range from 9×10^{-4} to 20.6 Jupiter masses with a mean value of 2.5, the semi-major axes from 8×10^{-3} to 177 AU with a mean value of 2.14, and eccentricities from 0 to 0.96 with a mean value of 0.19. The distributions of those orbital elements are shown in Figure 1.6.

Although the sample is quite limited, we see that the orbital elements of the S-type planets are quite diversified. Note that in Fig. 1.6 we restricted the data to planets with a mass higher than 0.5 Jupiter masses. If we compare the

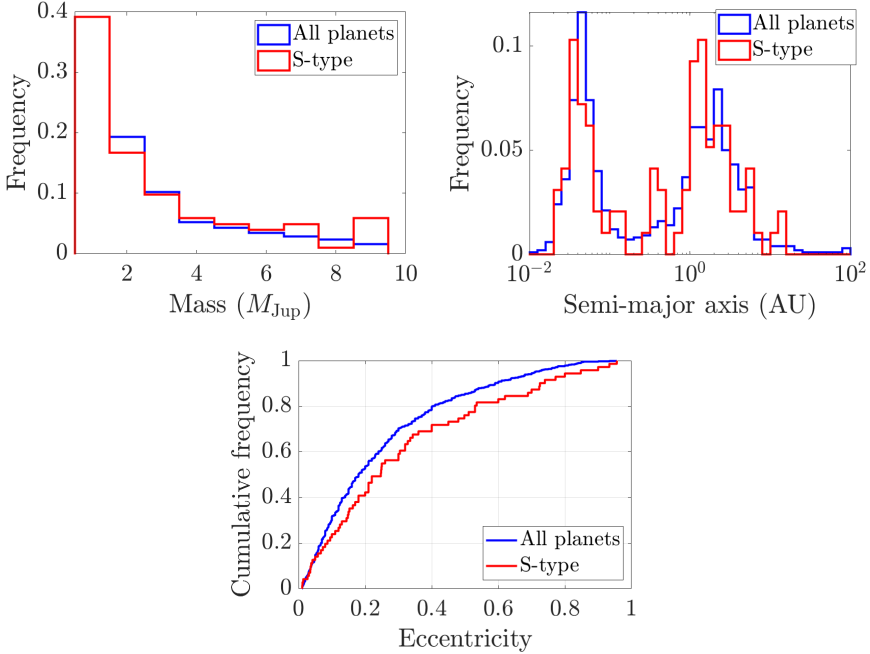


Figure 1.6 – Orbital parameter values of S-type giant planets issued from Rein (2012)

S-type planets (in red) to all the detected exoplanets (in blue), it seems that the S-type planets are more eccentric, since 70% of them have an eccentricity below 0.4 while the percentage increases to 80% for all the exoplanets, as seen on the bottom panel of Fig. 1.6. The top-right panel shows that there is a pile-up of S-type planets around an orbital period of 3-6 days. This is in agreement with the current observations of triple star systems (e.g., Duquennoy and Mayor, 1991; Tokovinin, 1997, 2001, 2014). The planetary masses are very similar in both distributions, as we can see on the top-left panel of Fig. 1.6. The influence of the binary companion on the eccentricity and orbital period distributions could come from the Lidov-Kozai resonance (Lidov, 1962; Kozai, 1962), as it will be discussed later in this work.

1.3 Formation

In this section, we will briefly review the current formation theories for planetary systems, with a particular emphasis on the planetary migration process and the influence of the binary companion.

1.3.1 Star formation

The formation of stars takes place in molecular clouds made of gas and dust. Fig. 1.7 shows the Carina nebula, a typical example of stellar nursery where lots of stars are born. Some regions in the cloud are denser. If the density is sufficient in some place, the cloud will start to collapse since gravitational forces overpass pressure forces. This collapse will result in an increase of density and temperature in the center of the collapsing zone and create a protostar (e.g., Shu et al., 1987; McKee and Ostriker, 2007). The conservation of the total angular momentum of the system leads, since materials accumulate into the protostar, to an increase in the rotation speed of the protostar. It will also result in the formation of a rotated disk made of gas and dust (e.g., Safronov, 1972). As long as gravitational forces of the protostar are stronger than the conservation of angular momentum of the particles forming the disk, it will continue to accrete. At some point the pressure and temperature will be high enough to start thermonuclear fusion and the protostar will start to shine. The star is born. Later on, the gravitational forces will not be sufficient to pursue significantly the accretion and the mass of the star will remain quite constant. More information about the physical processes involved in star formation can be found in Girichidis et al. (2020). At this moment, the disk created through conservation of the angular momentum of the initial cloud has a sufficiently high angular momentum to keep its structure nearly constant for a time sufficient to form planets through processes that we will present in the next sections (e.g., Armitage, 2009).

Regarding binary stars, both stars could follow the same formation scheme but the physical process resulting in the duality of the binary is still under debate. Two main models are currently proposed to explain this duality. The first one is the *turbulent fragmentation model* while the second one is called *disk fragmentation model*. The first scenario argues that turbulences in early collapse region of the star will lead to multiple density zones that will collapse independently to form multiple stars (Goodwin et al., 2004; Fisher, 2004). In the second model, the binary companion was born through accretion in the disk surrounding the primary through gravitational instabilities (Adams et al., 1989). A similar model is also used to explain the formation of giant planets and will be detailed later in the manuscript. We recall that, as mentioned previously, binary stars can undergo dramatic events during their long-term evolution and be disrupted through external perturbers. On the contrary, binary stars could result from the close passage between two stars.



Figure 1.7 – Carina nebula. ©NASA, ESA, and M. Livio and the Hubble 20th Anniversary Team (STScI)

1.3.2 Planetary system formation

The understanding of planet formation is still a challenging process. In this section, we will summarize some key features about planet growth and pay a particular attention on giant planet formation. The formation of giant planets is challenging since it has to be fast enough to form the planets before the dissipation of the gaseous disk and explain their composition mainly made of gas. Currently two main models are considered to explain their formation: the *core accretion model* (Pollack et al., 1996) and the *disk instability model* (Boss, 1997, 2003).

The core accretion model starts by the formation of a solid planet embryo through two main stages. The first stage of planet embryo formation is the most challenging one. The growth from micrometer-size objects to centimeter-size objects is most probably achieved through collisional growth by hit and stick collisions. The further growth is more subject to debate and there is no consensus about the growth up to kilometer-size objects. Indeed, various physical effects are at play at this moment to inhibit further growth of the objects. The first one is that meter-size objects will experience a strong gas drag that will lead them to fall on the star in about 100 years for an object

initially at 1 astronomical unit of its star (Weidenschilling, 1977). Another limitation is that the hit and stick collisions could not work anymore from a certain size level. Some observations in laboratory have shown that millimeter to centimeter-size objects will not grow anymore in mean (Chokshi et al., 1993; Dominik and Tielens, 1997; Gorti et al., 2015; Krijt et al., 2016). Depending on the impact speed and the size of the particles, they are likely to bounce off instead of merging, since at some point they are too little massive to merge through gravitational forces and too massive to merge through electrostatic forces (Wada et al., 2009; Zsom et al., 2010; Birnstiel et al., 2011; Testi et al., 2014). The impact could, if the speed is high enough, even lead to a fragmentation of the particle (Krijt et al., 2015). To solve the problem, another scenario than collisional merging was proposed. In this scenario, planetesimals will appear thanks to self-gravity. This process will happen only if the density is strong enough in some area in the disk. When high density is reached, the particles will collapse through gravitational forces (Goldreich and Ward, 1973; Youdin and Shu, 2002; Johansen et al., 2014). This collapse will be fast enough to overpass the problem of the fall of meter-size objects on their hosting star and also solve the problems with the collisional mechanism. The question of the formation of dense zones remains. Various propositions have been made to explain this concentration and some are presented in Izidoro and Raymond (2018) to which we refer for more details.

In the second stage, the gravitational forces between the planetesimals will play a key role since they will interact together leading to collisions. Through those collisions, the planetesimals will merge and therefore grow. This phase is made of two regimes. In the first regime, called *runaway growth*, the planetesimals collide and coalesce with each other, and the big ones will grow faster than the small ones (Greenberg et al., 1978). When the first planetary embryos are formed, they will start to gravitationally dominate the remaining small planetesimals. From this effect will result the second regime, the *oligarchic growth* (Kokubo and Ida, 1998, 2000; Chambers, 2006). In this regime, the more massive planetary embryos (called "oligarch") will grow through accretion of the planetesimals in their vicinity. Another scenario exists for the second stage of planet embryo formation which assumes that the planetesimals formed continue to accrete dust and gas from the disk. This scenario is referred to as *pebble accretion* (see, e.g., Johansen and Lacerda, 2010; Ormel and Klahr, 2010; Lambrechts and Johansen, 2012; Johansen et al., 2015; Bitsch et al., 2015; Xu et al., 2017; Bitsch et al., 2018, for more details).

Concerning the formation of giant planets, when the planetary embryos are massive enough, they will begin to accrete gas from the disk. At first, the accretion of gas is slow. This phase is called hydrostatic growth since the planet is in quasi-hydrostatic equilibrium at this point. When the mass

of the envelope is comparable to the mass of the central core, a runaway gas accretion starts. At some point, the accretion stops (the exact conditions are still under debate). Afterwards, the planet will contract over time and cool. Note that giant planets most likely form beyond the so-called snowline whose position depends on time and disk accretion rate (Garaud and Lin, 2007; Oka et al., 2011; Morbidelli et al., 2016). This line is the location beyond which the temperature is small enough to have volatile elements such as water, ammonia and methane in solid state. Those elements added to the heavy elements such as rocks, silicates and metals will result in a denser region in solid materials allowing the formation of cores heavy enough to accrete gas. This explains the formation of giant planets beyond the snowline.

For terrestrial planets, after the oligarchic growth phase, one last stage of planet formation takes place called *late-stage accretion* or orderly growth (Chambers and Wetherill, 1998; Raymond et al., 2004). In this stage the mass of the remaining planetesimals is negligible as compared to the total mass of the planetary embryos. This stage is characterized by the collisions between the embryos leading to the formation of the terrestrial planets from their merging. This stage could also be influenced by one or several giant planets previously formed beyond the snowline (Chambers and Cassen, 2002; Levison and Agnor, 2003; Raymond, 2006; Sotiriadis et al., 2018).

The second model for giant planet formation consists in the fragmentation of the disk in planets due to gravitational instabilities coming from the self-gravity of the disk and is close to the scenario presented for the star formation. In both models, the formation of giant planets is fast enough to be carried out within the disk lifetime. The first model is prevalent because the second model requires very massive disks and forms planets far away from their host star. In addition, the formation of Neptune-mass planets is not explained through the disk instability model, as well as the lack of heavy elements in Jupiter and Saturn's atmosphere.

At this point, the newly formed planets are susceptible to migrate through mechanisms that will be described in detail in the next section. In particular, in this work, we will focus on the evolution during the late stage of the gaseous disk and after its dispersal. For further details about the formation of giant planets, we refer for instance to Armitage (2009), Morbidelli et al. (2012), Helled et al. (2014) and D'Angelo and Lissauer (2018).

1.3.3 Migration

In the previous section, we described the formation of planets, more specifically their growth and the establishment of their masses. In this section we will focus our attention on their dynamical evolution in order to understand their

orbit and distance to the host star. Note that the interactions we present in this section can take place while the planets are still growing, in particular during the third phase of the terrestrial planet formation where the giant planets already formed could interact through those effects. As an example, concerning the solar system, the combination of the Grand Tack scenario (Walsh et al., 2012) and the Nice model (Tsiganis et al., 2005; Morbidelli et al., 2005; Gomes et al., 2005) can explain the formation of both the inner and outer regions of our system. The Grand Tack scenario is associated to the migration of the giant planets in the protoplanetary disk, while the Nice model takes place after the dissipation of the disk, when the planetesimals gravitationally interact together and with the planets. In our work, these two epochs (gas migration phase and N -body phase after the disk dispersal) will be investigated for binary star systems.

The interaction of a newly formed planet with the remaining gaseous disk could lead to modifications of the planetary eccentricity and inclination as well as the planetary semi-major axis. The change in the semi-major axis of a planet through its interaction with the disk is known as *migration* and is the result of an angular momentum exchange between the disk and the planet. This exchange is obtained through the action of the gravitational torque between the disk and the planet resulting in a migration for the planet and the launch of spiral waves at the location of the so-called Lindblad resonances in the disk (Goldreich and Tremaine, 1979). The material of the disk present outside of the planet orbit tends to decrease the angular momentum of the planet leading to an inward migration of the planet, while the gas inside its orbit increases its angular momentum resulting in an outward migration. The migration of the planet is the result of the addition of those two effects and the direction will depend on the dominating effect (Goldreich and Tremaine, 1980). Two main types of migration resulting from the interaction between a gaseous disk and a planet exist: the Type-I and Type-II migration. An intermediate regime exists between those two classes and is known as Type-III migration. The distinction between both classes is made based on the mass of the planets and their ability to open a gap in the disk.

In the *Type-I migration*, the planet is not very massive (typically a mass smaller than 10-15 Earth masses). In this case, the influence of the planet on the disk is limited and the planet will let the structure of the disk almost unchanged, as observed in Fig. 1.8a. This regime of migration applies in particular to the giant planet cores and is inward in almost all the disk configurations. Furthermore its timescale is short and mostly shorter than the disk lifetime for planets initially at a few astronomical units of their star. This raises the question of the survivability of the giant planet cores since they seem likely to crash on their host star (Ward, 1997). A lot of studies were made to solve the

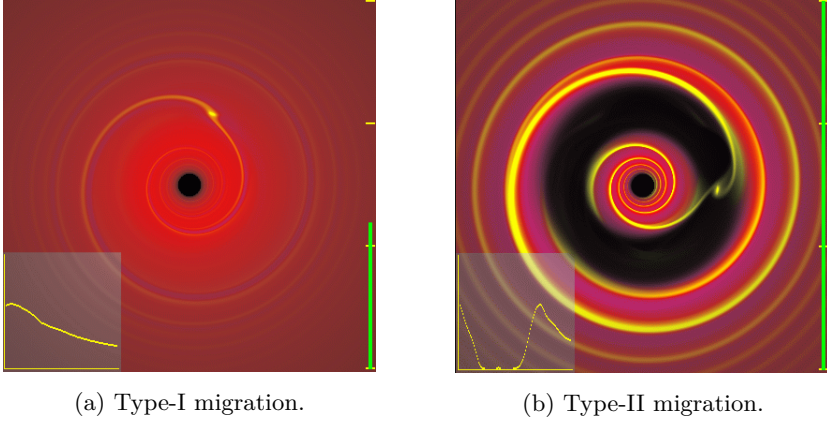


Figure 1.8 – Illustration of the two main regimes of migration from Armitage (2009)

question by slowing down or stopping the Type-I migration. We refer to the review of Baruteau et al. (2014) for more information.

The *Type-II migration* affects giant planets. In this case a gap is opened by the giant planet in its vicinity. A ring is created in the disk around the trajectory of the planet with a small density of material in it. An illustration is presented in Fig. 1.8b. The gap opening comes from the gravitational torque exerted by the planet on the disk. As mentioned previously, the interaction with the inner material pushes the planet to migrate outward and in response the material forming the disk moves inward, reversely the material of the outer disk is pushed outward while the planet moves inward. If the mass of the planet is sufficient, this effect will dominate the viscosity of the disk and tends to spread the disk and open a gap (Lin and Papaloizou, 1986a). At this point, the planet will stay stuck in the gap and will follow the intrinsic motion of the disk. The planet migrates inward at a timescale equal to the viscous accretion timescale (Lin and Papaloizou, 1986b). However if the planet is more massive than the local gas disk, it will slow down the viscous accretion timescale. Note that if the density of the gap is not negligible (for example with a high viscosity of the disk), the migration could be softened and could even result in an outward migration (Crida and Morbidelli, 2007). For more details about migration we refer to the works of Armitage (2009) and Baruteau et al. (2014), for example.

In addition, the disk will also play a key role on the eccentricity and inclination of the planets. Indeed, it has been shown through hydrodynamical simulations that the disk mostly tends to damp the eccentricity and inclination of embedded planets (Cresswell et al., 2007; Moorhead and Ford, 2009; Bitsch

and Kley, 2011). However, for very massive planets, the interaction with the disk can lead to instabilities in the disk and possibly to an excitation of the eccentricity of the planet (Papaloizou et al., 2001). If the planet is inclined with respect to the disk, a coupled evolution of the inclination and eccentricity of the planet can also occur coming from a *Lidov-Kozai resonance* of the planet with the disk. The Lidov-Kozai resonance was first introduced by Lidov (1962) and Kozai (1962) for an asteroid orbiting the Sun under the gravitational influence of Jupiter. In the star-disk-planet case, the disk plays the role of the third body. But, even if it induces large variations in eccentricity and inclination, this effect does not suppress the inclination and eccentricity damping (Terquem and Ajmia, 2010; Teyssandier et al., 2013; Xiang-Gruess and Papaloizou, 2013; Bitsch et al., 2013).

As a consequence of planet migration, in multi-planet systems, captures in a *mean motion resonance* may occur when the period ratio between two planets is close to a fraction of two small integers. As an example, in a 2:1 mean-motion resonance, the outer planet achieves a complete revolution around its star in twice as long as the inner planet does it. While crossing the resonance, the planets can either be trapped in the resonance and then start a coupled migration, or overpass the resonance and keep their proper motion. To ensure a capture in resonance the relative migration timescale between the two planets has to be small enough to let the resonance settle (Snellgrove et al., 2001; Quillen, 2006; Mustill and Wyatt, 2011). The resonant capture also leads to an eccentricity-type resonance that increases the eccentricities of the planets (Peale, 1976) and if the eccentricities are high enough, an increase in inclination may also occur through an inclination-type resonance (Thommes and Lissauer, 2003; Libert and Tsiganis, 2009b, 2011a,b; Teyssandier and Terquem, 2014; Sotiriadis and Libert, 2020).

A last effect that can strongly affect the orbit of the planets is the *planet-planet scattering* (Weidenschilling and Marzari, 1996; Rasio and Ford, 1996; Chatterjee et al., 2008; Jurić and Tremaine, 2008; Beaugé and Nesvorný, 2012). This effect results from the gravitational interaction between the planets. When a close encounter happens between two planets, their gravitational interaction can lead to a chaotic period able to strongly influence their orbits through orbital displacement and excitation of eccentricity and inclination. The instability could even lead to the ejection of a planet from the system. Note that this interaction could happen during the migration phase (Marzari et al., 2010; Lega et al., 2013).

1.3.4 Influence of a binary companion

The question of the formation of planets in binary stars remains open, since the stellar companion can strongly affect the planet formation process. Extensive studies have analyzed the long-term stability and habitability of giant planets detected in binary star systems (e.g., Haghighipour, 2010; Bazsó et al., 2017). The long-term stability has mostly been investigated via numerical N -body simulations, either looking at possible escape of a planet (e.g., Rabl and Dvorak, 1988; Holman and Wiegert, 1999) or using chaos indicators or frequency map analysis (see e.g., Pilat-Lohinger et al., 2003; Marzari and Gallina, 2016). Those works lead to the establishment of some stability criteria. Holman and Wiegert (1999) provided a critical semi-major axis within which planets are stable under the perturbation of a binary companion. Marzari and Gallina (2016) studied the Hill stability criterion (minimum separation between two planets to avoid mutual close encounters, see, e.g., Marchal and Bozis, 1982; Gladman, 1993; Chambers et al., 1996) in the context of binary star systems. Stability criteria were also deduced for hierarchical triple systems (see Eggleton and Kiseleva, 1995; Mardling and Aarseth, 2001; He and Petrovich, 2018, for more details). Planet formation has principally been investigated for close binaries in which giant planets have been detected despite a very strong perturbation of the stellar companion. For S-type planets in wide binaries, owing to a higher stellar separation, it is reasonable to expect that the binary companion would have a more limited (but still significant) impact on the planet formation process.

The different stages of planet formation can be affected by a binary companion (see, e.g., Thébault and Haghighipour, 2015 for a review). Firstly, during the formation of the protoplanetary disk, the disk can be truncated by the stellar companion (Artymowicz and Lubow, 1994; Savonije et al., 1994). Observations have shown that disks in close binaries tend to be less frequent and less massive than around single stars (Kraus and Ireland, 2012). The binary companion could also influence the disk leading to a nodal precession or even a wrap of the disk if the disk is not massive enough to suppress the influence of the binary companion through its self-gravity (Batygin et al., 2011; Zanazzi and Lai, 2017). Secondly, the intermediate stage of kilometer-sized planetesimal accretion is extremely sensitive to stellar companion perturbations (Thébault et al., 2006). The formation of planets in close binaries or in the presence of a massive and inclined distant perturber (inducing the Lidov-Kozai excitations of the protoplanetary disk; e.g., Martin et al., 2014; Fu et al., 2015; Zanazzi and Lai, 2017) is still a theoretical issue, since even moderate dynamical perturbations can generate high-velocity impacts and thus inhibit the formation of planetary embryos (Lissauer, 1993). However, Batygin et al. (2011) showed

that disk self-gravity can be sufficient to suppress the Lidov-Kozai oscillations and maintain orbital coherence and planetary growth in the presence of a massive and inclined distant perturber. The decisive role that disk gravity plays in planetesimal dynamics was also confirmed by Rafikov and Silsbee (2015). Lastly, it was shown that in the late stage of planetary accretion, from Lunar-sized embryos to fully formed planets, the embryo accretion region roughly corresponds to the stability domain (e.g., Quintana et al. (2007)). Haghighipour and Raymond (2007) analyzed the formation of terrestrial planets in close binaries, assuming the existence of a giant planet already formed further out in the disk and a hundred planetary embryos (Moon- to Mars-sized bodies) formed in the region between the primary and the giant planet. These authors showed that planet formation can be efficient in moderately close binary planetary systems, and the final assembly of the planets and their water content strongly depend on the parameters of the stellar companion.

Regarding the formation of giant planet systems in binary stars, much attention was directed toward the formation of hot Jupiters via Lidov-Kozai cycles and tidal friction (e.g., Fabrycky and Tremaine, 2007). In this case, the combination of the two effects leads the giant planet to migrate inward and could explain the observation of hot Jupiters in binary stars. The planet-planet scattering mechanism was considered for Jupiter-mass planets orbiting the central star of a close binary system (Marzari et al., 2005). Several hydrodynamical simulations of giant planets evolving in gas disks were performed for binary systems. Without providing an exhaustive list, we cite the following works. The evolution of planets embedded in circumbinary disks was considered for close binary stars, for instance, in Kley and Haghighipour (2014) for Kepler-38. Xiang-Gruess and Papaloizou (2014), Picogna and Marzari (2015), and Lubow and Martin (2016) studied the evolution of a giant planet-disk system in the presence of an inclined binary companion and found that a substantial misalignment between the orbit of the planet and the disk generally occurs. Finally, Martin et al. (2016) studied the formation of giant planets in Lidov-Kozai resonance with a highly misaligned binary companion, starting from a coplanar planet-disk system configuration.

1.4 Conclusions

In this chapter we presented some generalities about binary stars as well as the distribution of the known S-type planets. In the second part of the chapter, we reviewed the formation of planetary systems from the birth of the stars to the late-stage of planetary formation. A discussion about the influence of the binary companion in the formation of giant planet systems closed the chapter.

In this work, we aim to study the formation and dynamical evolution of giant planet systems influenced by a binary companion, especially during the migration phase of the planets. The next chapter is devoted to the presentation of the code developed to achieve this goal, and in particular the formulas used to model the interaction with the disk.

Chapter 2

Implementation of a symplectic integrator for binary stars

In this chapter we describe the code designed to follow the migration of planets in S-type binaries. We developed a symplectic integrator for S-type binaries that has the advantage of being stable for long-term integration by using the symplectic structure of the problem. The code is described in the first section of the chapter. The second section focuses on the implementation of the Type-II migration and the disk eccentricity and inclination damping acting on the planets during the late-stage formation of planetary systems.

2.1 Symplectic integrator

2.1.1 Definition

A numerical integrator is used to compute numerical approximations to the solution of differential equations or, more generally, partial differential equations. Regarding the N -body problem, the system evolves over time and therefore with time derivatives. In practice, the algorithm performs a time discretization to obtain solutions at specific times based on the state of the system at the previous times. Mathematically, the evolution of the system can be expressed as

$$\mathbf{x}^{(k+1)} = \Phi\left(\mathbf{x}^{(k)}, \mathbf{x}^{(k-1)}, \dots, \mathbf{x}^{(2)}, \mathbf{x}^{(1)}, \mathbf{x}^{(0)}\right), \quad (2.1)$$

where $\mathbf{x}^{(i)}$ is the state of the system at time t_i and $\mathbf{x}^{(0)}$ is the initial state of the system.

For our study, we work with an Hamiltonian formalism, such that the evolution of the system is defined through the Hamiltonian equations

$$\begin{cases} \frac{dq_i}{dt} = \frac{\partial \mathcal{H}}{\partial p_i} \\ \frac{dp_i}{dt} = -\frac{\partial \mathcal{H}}{\partial q_i} \end{cases} \quad i = 1 \dots n, \quad (2.2)$$

where \mathcal{H} is the Hamiltonian of the system, q_i are the generalized coordinates and p_i their conjugated momenta. Note that to preserve the Hamiltonian structure of the problem, every change of coordinates has to be, by definition, canonical. The change from the \mathbf{x} coordinates to the \mathbf{y} coordinates is canonical if and only if the matrix defined by

$$C_{ij} = \frac{\partial y_i}{\partial x_j} \quad (2.3)$$

is symplectic, i.e.,

$$C^T J C = J, \quad (2.4)$$

where J is the antisymmetric matrix

$$J = \begin{pmatrix} 0_n & I_n \\ -I_n & 0_n \end{pmatrix}, \quad (2.5)$$

with I_n the identity matrix of order n , 0_n the null matrix of order n .

In our case, the integrator uses only the state of the system at the preceding time. Consequently, Eq. (2.1) rewrites

$$\left(\mathbf{q}^{(k+1)}, \mathbf{p}^{(k+1)} \right) = \Phi \left(\mathbf{q}^{(k)}, \mathbf{p}^{(k)} \right), \quad (2.6)$$

where $\mathbf{q}^{(k)} = \left(q_1^{(k)}, q_2^{(k)}, \dots, q_n^{(k)} \right)$ and $\mathbf{p}^{(k)} = \left(p_1^{(k)}, p_2^{(k)}, \dots, p_n^{(k)} \right)$, with $q_i^{(k)}$ and $p_i^{(k)}$ the generalized coordinates and the associated momenta at time t_k .

In addition, symplectic integrators have been developed to numerically approximate the evolution of conservative systems, i.e., whose Hamiltonian (equivalent to the total energy of the system) is constant over time:

$$\frac{d\mathcal{H}}{dt} = 0. \quad (2.7)$$

An integrator is symplectic if and only if the Jacobian matrix defined by

$$A_{ij} = \frac{\partial x_i^{(k+1)}}{\partial x_j^{(k)}}, \quad (2.8)$$

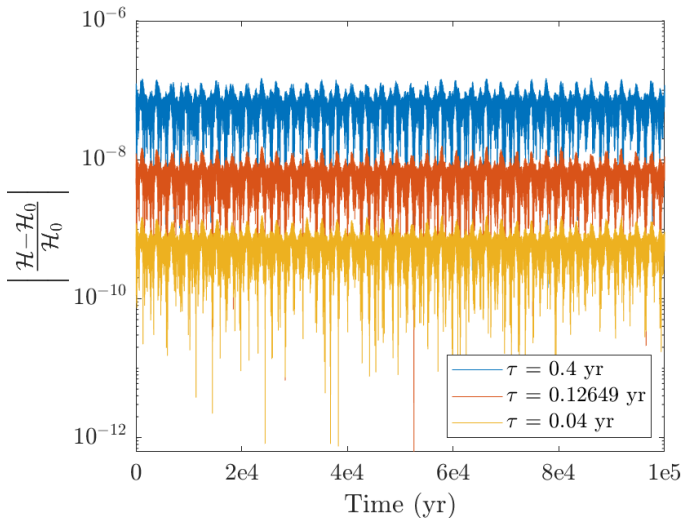


Figure 2.1 – Hamiltonian conservation

with $\mathbf{x}^{(k)} = (\mathbf{q}^{(k)}, \mathbf{p}^{(k)})$, is symplectic (i.e., verifies Eq. (2.4)). As mentioned previously, numerical integrators provide numerical approximate solutions of the problem and do not keep \mathcal{H} exactly constant. However, symplectic integrators are useful since they manage to keep the relative error $\frac{\mathcal{H}_k - \mathcal{H}_0}{\mathcal{H}_0}$ bounded (\mathcal{H}_0 and \mathcal{H}_k are the Hamiltonian at time 0 and at time k , respectively), as it can be observed in Fig. 2.1. More interestingly, the error on the Hamiltonian remains bounded even when adopting relatively big time steps. More details on the error of symplectic integrators (as a function of the integration time step) are given in the next section. To preserve the symplectic structure of the problem, Duncan et al. (1998) prescribed a time step of about 1/20th of the shortest orbital period of the system. Let us recall that many numerical integrators are not suitable for long-term integrations because either they diverge with a big time step due to numerical errors, or they require too much computation time when using a small time step.

2.1.2 Construction

We now present the construction of a symplectic integrator⁽¹⁾. Using Eq. (2.2), we can study the evolution of a quantity f depending on the generalized coordinates and their associated momenta. With the chain rule, we can

(1). Other construction methods were developed, see, e.g., Wisdom and Holman (1991) for a construction based on the Dirac delta function.

express $\frac{df}{dt}$ as

$$\frac{df}{dt} = \sum_{i=1}^n \frac{\partial f}{\partial q_i} \frac{\partial \mathcal{H}}{\partial p_i} - \frac{\partial f}{\partial p_i} \frac{\partial \mathcal{H}}{\partial q_i}. \quad (2.9)$$

Adopting the Poisson bracket, we find

$$\frac{df}{dt} = \{f, \mathcal{H}\}. \quad (2.10)$$

If we assume that there exists a linear operator T associated with the Hamiltonian through the relation $Tf = \{f, \mathcal{H}\}$, Eq. (2.10) becomes the usual differential equation

$$\frac{df}{dt} = Tf \quad (2.11)$$

whose solution is given by

$$f(t) = e^{tT} f(0), \quad (2.12)$$

where $f(0)$ is the initial value of f .

To simplify the calculation of the previous expression, symplectic integrators split the Hamiltonian in several parts that can be solved separately. Most of the time, several parts are chosen to be solved analytically even though it is not necessary. We consider a division of the Hamiltonian in two parts

$$\mathcal{H} = \mathcal{H}_A + \mathcal{H}_B. \quad (2.13)$$

Since Poisson brackets are linear, Eq. (2.10) becomes

$$\frac{df}{dt} = \{f, \mathcal{H}_A\} + \{f, \mathcal{H}_B\}. \quad (2.14)$$

Considering the linear operators T_A and T_B associated with the parts \mathcal{H}_A and \mathcal{H}_B through $T_A f = \{f, \mathcal{H}_A\}$ and $T_B f = \{f, \mathcal{H}_B\}$, respectively, we obtain

$$\frac{df}{dt} = T_A f + T_B f = (T_A + T_B) f, \quad (2.15)$$

whose solution is an exponential function:

$$f(t) = e^{t(T_A + T_B)} f(0). \quad (2.16)$$

The problem will be solved step by step. Using an integration step τ , Eq. (2.16) will be approximated as follows

$$f(t) = e^{t(T_A + T_B)} f(0) = e^{\frac{t}{\tau}(T_A + T_B)} f(0) \approx \Psi\left(\frac{t}{\tau}\right)(f(0)), \quad (2.17)$$

where $\Psi^{(n)}(x)$ stands for the application of $\Psi(x)$ n times and $\Psi(x)$ denotes an approximation of $e^{\tau(T_A + T_B)} x$ based on the Baker-Campbell-Hausdorff (BCH)

formula (Bourbaki, 1972) which switches from a product of exponentials of operators to an exponential of a sum of operators as follows

$$e^A e^B = \exp \left\{ A + B + \frac{1}{2} [A, B] + \frac{1}{12} ([A, [A, B]] - [B, [A, B]]) + \dots \right\}, \quad (2.18)$$

where $[A, B] = AB - BA$. Note that since the linear operators do not commute in general with respect to the multiplication, the use of the BCH formula is needed.

Eq. (2.17) can be written through the recurrence relation:

$$\begin{cases} f(t_{k+1}) = \Psi(f(t_k)) \\ f(t_0) = f_0 \end{cases} \quad k \in \mathbb{N}, \quad (2.19)$$

where f_0 is the initial state of the system and $t_{k+1} = t_k + \tau$. We apply as many steps of recurrence as necessary until the final integration time.

Several combinations of $e^{\tau_1 T_A}$ and $e^{\tau_2 T_B}$ are possible to approximate $e^{\tau(T_A + T_B)}$, leading to different families of symplectic integrators. We will discuss two main families here: the one presented in Laskar and Robutel (2001) and the one presented in Yoshida (1990).

2.1.2.1 Symplectic integrators from Laskar and Robutel (2001)

The approximation of $e^{\tau(T_A + T_B)}$ in Laskar and Robutel (2001) is based on the assumption that the Hamiltonian can be divided in two parts verifying

$$\mathcal{H}_B = \epsilon \mathcal{H}_A \quad (2.20)$$

with

$$\epsilon \ll 1. \quad (2.21)$$

Such a condition is frequently fulfilled in planetary theory. In Laskar and Robutel (2001), they proposed four different approximations of $e^{\tau(\mathcal{H}_A + \mathcal{H}_B)}$:

$$\begin{aligned} \text{SABA}_{2n} & e^{c_1 \tau T_A} e^{d_1 \tau T_B} e^{c_2 \tau T_A} e^{d_2 \tau T_B} \dots e^{d_n \tau T_B} e^{c_{n+1} \tau T_A} e^{d_n \tau T_B} \dots \\ & e^{d_2 \tau T_B} e^{c_2 \tau T_A} e^{d_1 \tau T_B} e^{c_1 \tau T_A} \\ \text{SABA}_{2n+1} & e^{c_1 \tau T_A} e^{d_1 \tau T_B} e^{c_2 \tau T_A} e^{d_2 \tau T_B} \dots e^{c_{n+1} \tau T_A} e^{d_{n+1} \tau T_B} e^{c_{n+1} \tau T_A} \dots \\ & e^{d_2 \tau T_B} e^{c_2 \tau T_A} e^{d_1 \tau T_B} e^{c_1 \tau T_A} \\ \text{SBAB}_{2n} & e^{d_1 \tau T_B} e^{c_2 \tau T_A} e^{d_2 \tau T_B} e^{c_3 \tau T_A} \dots e^{c_{n+1} \tau T_A} e^{d_{n+1} \tau T_B} e^{d_{n+1} \tau T_A} \dots \\ & e^{c_3 \tau T_A} e^{d_2 \tau T_B} e^{c_2 \tau T_A} e^{d_1 \tau T_B} \\ \text{SBAB}_{2n+1} & e^{d_1 \tau T_B} e^{c_2 \tau T_A} e^{d_2 \tau T_B} e^{c_3 \tau T_A} \dots e^{d_{n+1} \tau T_B} e^{c_{n+2} \tau T_A} e^{d_{n+1} \tau T_B} \dots \\ & e^{c_3 \tau T_A} e^{d_2 \tau T_B} e^{c_2 \tau T_A} e^{d_1 \tau T_B} \end{aligned} \quad (2.22)$$

Using Eq. (2.18) and neglecting the terms of order $\mathcal{O}(\epsilon^n)$ with $n \geq 2$ (since ϵ is small), they determined the coefficients c_k and d_k such that the integrators

SABA_{*i*} and SBAB_{*i*} have a local error ⁽²⁾, corresponding to the error made when applying one time step in the integration, of order $\mathcal{O}(\tau^{2i+1}\epsilon)$. Moreover, the global error, corresponding to the error made at the end of the integration, is $\frac{t_{final}}{\tau} \times \text{local error}$, i.e., SABA_{*i*} is of order $\mathcal{O}(\tau^{2i}\epsilon)$.

2.1.2.2 Symplectic integrators from Yoshida (1990)

Yoshida (1990) constructed symplectic integrators based on the leapfrog algorithm corresponding to the following approximation of order 2:

$$e^{\tau(T_A+T_B)} \approx e^{\frac{1}{2}\tau T_A} e^{\tau T_B} e^{\frac{1}{2}\tau T_A} \stackrel{not}{\equiv} Y_2(\tau). \quad (2.23)$$

Note that Y_2 is equivalent to SABA₁ and SBAB₁ (both have the same coefficients as shown in Laskar and Robutel (2001)). Integrators of higher orders are recursively defined as

$$Y_{2n+2}(\tau) = Y_{2n}(z_{1,2n}\tau)Y_{2n}(z_{0,2n}\tau)Y_{2n}(z_{1,2n}\tau), \quad n \in \mathbb{N}. \quad (2.24)$$

Using Eq. (2.18), Yoshida (1990) deduced the coefficients $z_{0,2n}$ and $z_{1,2n}$ such that the symplectic integrator Y_{2n+2} is of order $2n+2$:

$$\begin{cases} z_{0,2n} = \frac{-2^{\frac{1}{2n+1}}}{2 - 2^{\frac{1}{2n+1}}} \\ z_{1,2n} = \frac{1}{2 - 2^{\frac{1}{2n+1}}}. \end{cases} \quad (2.25)$$

For an integration of order $2i$, the symplectic integrators from Laskar and Robutel (2001) require $2i+1$ evaluations of an Hamiltonian, while the symplectic integrators from Yoshida (1990) require 3^i evaluations, which means an exponential increase of operations to reach a better precision. However, this family of symplectic integrators proves to be particularly interesting for systems for which the condition (2.21) is not verified.

2.1.3 Splitting in three parts

The symplectic code SyMBA used in this work (see next section for a full description) relies on the leapfrog integrator common to both families. The Hamiltonian of the N -body problem is divided in three parts

$$\mathcal{H} = \mathcal{H}_A + \mathcal{H}_B + \mathcal{H}_C, \quad (2.26)$$

(2). Note that as precised in Laskar and Robutel (2001), the true order of the error is $\mathcal{O}(\max(\tau^{2i+1}\epsilon, \tau^3\epsilon^2))$ but can be reduced to the previous value if the terms proportional to ϵ^2 are negligible.

and the evolution of $f(t_{k+1})$ is numerically approximated by the expression

$$f(t_{k+1}) = \exp\left(\frac{\tau}{2}T_A\right) \exp\left(\frac{\tau}{2}T_B\right) \exp(\tau T_C) \exp\left(\frac{\tau}{2}T_B\right) \exp\left(\frac{\tau}{2}T_A\right) f(t_k), k \in \mathbb{N}, \quad (2.27)$$

where T_A , T_B and T_C are the linear operators associated to \mathcal{H}_A , \mathcal{H}_B , and \mathcal{H}_C , respectively⁽³⁾. The evolution of the quantity f is obtained by making it evolve under \mathcal{H}_A for half a time step, then under \mathcal{H}_B for the same duration, followed by an evolution under \mathcal{H}_C during a full time step, then again under \mathcal{H}_B for half a time step and finally under \mathcal{H}_A for half a time step. The local error for this integrator is of order $\mathcal{O}((\epsilon_1 + \epsilon_2)\tau^3)$, with $\epsilon_1 = \frac{\mathcal{H}_A}{\mathcal{H}_B + \mathcal{H}_C}$ and $\epsilon_2 = \frac{\mathcal{H}_B}{\mathcal{H}_C}$, leading to a global error of order $\mathcal{O}((\epsilon_1 + \epsilon_2)\tau^2)$. From the expression of the error, we deduce the importance of having

$$\epsilon_1 \ll 1 \quad \text{and} \quad \epsilon_2 \ll 1. \quad (2.28)$$

to get a precise integration of the system. In practice, we will thus require $\mathcal{H}_C \gg \mathcal{H}_B$ and $\mathcal{H}_C \gg \mathcal{H}_A$.

2.1.4 SyMBA

We now detail the code used in this work. First, we present the symplectic integrator SyMBA (Duncan et al., 1998) designed for the integration of a planetary system with a central star (planetary N -body problem). The decomposition of the Hamiltonian is the following

$$\mathcal{H} = \mathcal{H}_{\text{Int}}^{\text{CH}} + \mathcal{H}_{\text{Jump}}^{\text{CH}} + \mathcal{H}_{\text{Kep}}^{\text{CH}} \quad (2.29)$$

with

$$\mathcal{H}_{\text{Kep}}^{\text{CH}} = \sum_{i=2}^N \left(\frac{\|\mathbf{p}_i^{\text{CH}}\|^2}{2m_i} - \frac{Gm_A m_i}{\|\mathbf{r}_i^{\text{CH}}\|} \right), \quad (2.30)$$

$$\mathcal{H}_{\text{Int}}^{\text{CH}} = - \sum_{i=2}^{N-1} \sum_{i < j \leq N} \frac{Gm_i m_j}{\|\mathbf{r}_{ij}\|}, \quad (2.31)$$

and

$$\mathcal{H}_{\text{Jump}}^{\text{CH}} = \frac{1}{2m_A} \left\| \sum_{i=2}^N \mathbf{p}_i^{\text{CH}} \right\|^2, \quad (2.32)$$

where $\mathbf{r}_{ij} = \mathbf{r}_i^{\text{CH}} - \mathbf{r}_j^{\text{CH}}$. Note that the coordinates for the bodies are the canonical heliocentric coordinates. In those coordinates, the position of the bodies is expressed in heliocentric frame while their velocity is expressed in barycentric

(3). To obtain this generalization, SBAB₁ is apply a first time on $\mathcal{H}_A + (\mathcal{H}_B + \mathcal{H}_C)$ and a second time on $\mathcal{H}_B + \mathcal{H}_C$.

coordinates. This choice of mixed coordinates ensures the symplectic structure of the Hamiltonian equations. In this splitting, the biggest part of the Hamiltonian, $\mathcal{H}_{\text{Kep}}^{\text{CH}}$, corresponds to the Keplerian motion of the bodies, while the two other parts are associated with the perturbations of the Keplerian motion.

The Keplerian motion of the bodies is evaluated using Gauss functions f and g . For an Hamiltonian of the form

$$\mathcal{H} = \frac{\|m\mathbf{v}\|^2}{2m} - \frac{\nu m}{\|\mathbf{r}\|}, \quad (2.33)$$

the evolution can be accurately approximated through

$$\begin{cases} \mathbf{r}(t_{k+1}) = f(\nu)\mathbf{r}(t_k) + g(\nu)\mathbf{v}(t_k) \\ \mathbf{v}(t_{k+1}) = \dot{f}(\nu)\mathbf{r}(t_k) + \dot{g}(\nu)\mathbf{v}(t_k) \end{cases} \quad k \in \mathbb{N}. \quad (2.34)$$

More details about this evolution can be found in Danby (1988).

The evolution under the two order parts, $\mathcal{H}_{\text{Int}}^{\text{CH}}$ and $\mathcal{H}_{\text{Jump}}^{\text{CH}}$, can be done analytically since they only depend on the positions (respectively momenta) of the bodies. Indeed, the Hamiltonian equations write

$$\begin{cases} \frac{dr_{l,i}^{\text{CH}}}{dt} = 0 \\ \frac{dp_{l,i}^{\text{CH}}}{dt} = - \frac{\partial \mathcal{H}_{\text{Int}}^{\text{CH}}(\mathbf{r}_1^{\text{CH}}, \mathbf{r}_2^{\text{CH}}, \dots, \mathbf{r}_N^{\text{CH}})}{\partial r_{l,i}^{\text{CH}}} \end{cases} \quad \text{and} \quad (2.35)$$

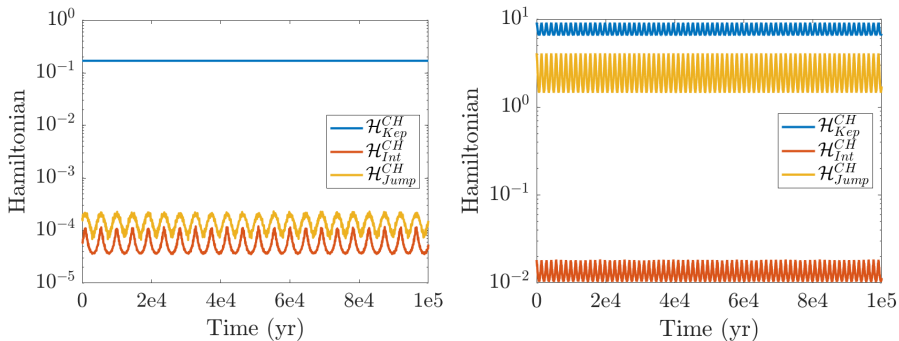
$$\begin{cases} \frac{dr_{l,i}^{\text{CH}}}{dt} = \frac{\partial \mathcal{H}_{\text{Jump}}^{\text{CH}}(\mathbf{p}_1^{\text{CH}}, \mathbf{p}_2^{\text{CH}}, \dots, \mathbf{p}_N^{\text{CH}})}{\partial p_{l,i}^{\text{CH}}} \\ \frac{dp_{l,i}^{\text{CH}}}{dt} = 0 \end{cases} \quad \begin{matrix} i = 1 \dots N \\ l = x, y, z \end{matrix},$$

whose exact solutions are

$$\begin{cases} r_{l,i}^{\text{CH}}(t) = r_{l,i}^{\text{CH}}(0) \\ p_{l,i}^{\text{CH}}(t) = p_{l,i}^{\text{CH}}(0) - t \frac{\partial \mathcal{H}_{\text{Int}}^{\text{CH}}(\mathbf{r}_1^{\text{CH}}, \mathbf{r}_2^{\text{CH}}, \dots, \mathbf{r}_N^{\text{CH}})}{\partial r_{l,i}^{\text{CH}}} \Big|_{(\mathbf{r}_1^{\text{CH}}(0), \mathbf{r}_2^{\text{CH}}(0), \dots, \mathbf{r}_N^{\text{CH}}(0))} \end{cases} \quad \text{and}$$

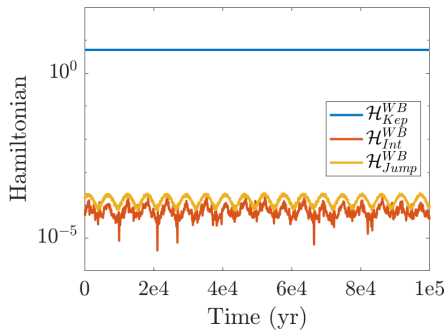
$$\begin{cases} r_{l,i}^{\text{CH}}(t) = r_{l,i}^{\text{CH}}(0) + t \frac{\partial \mathcal{H}_{\text{Jump}}^{\text{CH}}(\mathbf{p}_1^{\text{CH}}, \mathbf{p}_2^{\text{CH}}, \dots, \mathbf{p}_N^{\text{CH}})}{\partial p_{l,i}^{\text{CH}}} \Big|_{(\mathbf{p}_1^{\text{CH}}(0), \mathbf{p}_2^{\text{CH}}(0), \dots, \mathbf{p}_N^{\text{CH}}(0))} \\ p_{l,i}^{\text{CH}}(t) = p_{l,i}^{\text{CH}}(0) \end{cases}$$

$$\begin{matrix} i = 1 \dots N \\ l = x, y, z \end{matrix}, \quad (2.36)$$



(a) Without stellar companion in canonical heliocentric coordinates

(b) With a stellar companion in canonical heliocentric coordinates



(c) With a stellar companion in wide-binary coordinates

Figure 2.2 – Separation of the Hamiltonian

with $\mathbf{r}_i^{\text{CH}} = (r_{x,i}^{\text{CH}}, r_{y,i}^{\text{CH}}, r_{z,i}^{\text{CH}})$ and $\mathbf{p}_i^{\text{CH}} = (p_{x,i}^{\text{CH}}, p_{y,i}^{\text{CH}}, p_{z,i}^{\text{CH}})$. Those solutions highlight the interest of splitting the Hamiltonian in several parts depending only on the positions or momenta of the bodies.

Note that the condition on the parts of the Hamiltonian expressed in Eq. (2.28) is satisfied in the case of a two-planet system, but fails if the outer planet is replaced by a wide binary companion as illustrated in the top panels of Fig. 2.2. To solve this problem, a new set of coordinates was proposed in Chambers et al. (2002), as discussed in the next section.

2.1.5 Adaptation to binary stars

In this section we aim to describe the adaptation made in the integrator for wide binary stars. The wide binary coordinates (hereafter, WB) of Chambers

et al. (2002) are defined such that all the significant terms of the Hamiltonian can be incorporated into a single part of the Hamiltonian, as illustrated in the bottom panel of Fig. 2.2. The positions in the new set of coordinates are expressed by

$$\left\{ \begin{array}{l} \mathbf{r}_A^{\text{WB}} = \frac{m_A \mathbf{r}_A + m_B \mathbf{r}_B + \sum_{j=3}^N m_j \mathbf{r}_j}{m_{\text{sys}}} \\ \mathbf{r}_i^{\text{WB}} = \mathbf{r}_i - \mathbf{r}_A \quad i = 3 \dots N \\ \mathbf{r}_B^{\text{WB}} = \mathbf{r}_B - \frac{m_A \mathbf{r}_A + \sum_{j=1}^N m_j \mathbf{r}_j}{m_{\text{red}}}, \end{array} \right. \quad (2.37)$$

with A the primary star, B the stellar companion on a wide orbit, \mathbf{r}_j^{WB} the position of the j -th body in the new coordinates, \mathbf{r}_j the position of the j -th body in an inertial frame, m_j the mass of the body j , m_{sys} the total mass of the system, and $m_{\text{red}} = m_A + \sum_{i=3}^N m_i$. The conjugate momenta determined by Chambers et al. (2002) using a generating function (to ensure a canonical change of coordinates) are expressed by

$$\left\{ \begin{array}{l} \mathbf{p}_A^{\text{WB}} = \mathbf{p}_A + \mathbf{p}_B + \sum_{j=3}^N \mathbf{p}_j \\ \mathbf{p}_i^{\text{WB}} = \mathbf{p}_i - m_i \left(\frac{\mathbf{p}_A + \sum_{j=3}^N \mathbf{p}_j}{m_{\text{red}}} \right) \quad i = 3 \dots N \\ \mathbf{p}_B^{\text{WB}} = \mathbf{p}_B - m_B \left(\frac{\mathbf{p}_A + \mathbf{p}_B + \sum_{j=3}^N \mathbf{p}_j}{m_{\text{sys}}} \right), \end{array} \right. \quad (2.38)$$

with \mathbf{p}_j^{WB} the momentum of the j -th body in the new coordinates and \mathbf{p}_j the momentum of the j -th body in an inertial frame.

The new Hamiltonian is then splitted into these parts

$$\mathcal{H} = \mathcal{H}_{\text{Kep}}^{\text{WB}} + \mathcal{H}_{\text{Int}}^{\text{WB}} + \mathcal{H}_{\text{Jump}}^{\text{WB}}, \quad (2.39)$$

with

$$\mathcal{H}_{\text{Kep}}^{\text{WB}} = \frac{\|\mathbf{p}_B^{\text{WB}}\|^2}{2\mu_{\text{WB}}} - \frac{Gm_{\text{sys}}\mu_{\text{WB}}}{\|\mathbf{r}_B^{\text{WB}}\|} + \sum_{i=3}^N \left(\frac{\|\mathbf{p}_i^{\text{WB}}\|^2}{2m_i} - \frac{Gm_A m_i}{\|\mathbf{r}_i^{\text{WB}}\|} \right), \quad (2.40)$$

$$\begin{aligned}
\mathcal{H}_{\text{Int}}^{\text{WB}} = & - \sum_{i=3}^{N-1} \sum_{i < j \leq N} \frac{Gm_i m_j}{\|\mathbf{r}_{ij}\|} + Gm_A m_B \left(\frac{1}{\|\mathbf{r}_B^{\text{WB}}\|} - \frac{1}{\|\mathbf{r}_B^{\text{WB}} + \mathbf{s}\|} \right) \\
& + Gm_B \sum_{i=3}^N m_i \left(\frac{1}{\|\mathbf{r}_B^{\text{WB}}\|} - \frac{1}{\|\mathbf{r}_B^{\text{WB}} - \mathbf{r}_i^{\text{WB}} + \mathbf{s}\|} \right),
\end{aligned} \tag{2.41}$$

and

$$\mathcal{H}_{\text{Jump}}^{\text{WB}} = \frac{\left\| \sum_{i=3}^N \mathbf{p}_i^{\text{WB}} \right\|^2}{2m_A}, \tag{2.42}$$

where

$$\mathbf{s} = \frac{\sum_{i=3}^N m_i \mathbf{r}_i^{\text{WB}}}{m_{\text{red}}}, \quad \mathbf{r}_{ij} = \mathbf{r}_i^{\text{WB}} - \mathbf{r}_j^{\text{WB}} \quad \text{and} \quad \mu_{\text{WB}} = \frac{m_B m_{\text{red}}}{m_{\text{sys}}}. \tag{2.43}$$

Note that the first term of $\mathcal{H}_{\text{Int}}^{\text{WB}}$ will be absent for one-planet systems, as it will be the case in Chapters 3 and 4. Using this splitting, the evolution under the different parts of the Hamiltonian is easy. The evolution of the system under $\mathcal{H}_{\text{Kep}}^{\text{WB}}$ is achieved using the formulas from Danby (1988), as in SyMBA. The only difference lies in the definition of ν in Eq. (2.34). In SyMBA, comparing $\mathcal{H}_{\text{Kep}}^{\text{WB}}$ with Eq. (2.33) leads to a value of $\nu = m_A$ for the planets, but for the binary companion, ν becomes equal to m_{sys} considering that

$$\begin{cases} \mathbf{p}_A^{\text{WB}} = m_a \mathbf{v}_A^{\text{WB}} \\ \mathbf{p}_i^{\text{WB}} = m_i \mathbf{v}_i^{\text{WB}} \\ \mathbf{p}_B^{\text{WB}} = \mu_{\text{WB}} \mathbf{v}_B^{\text{WB}}, \end{cases} \quad i = 3 \dots N \tag{2.44}$$

with \mathbf{v}_A^{WB} , \mathbf{v}_i^{WB} , and \mathbf{v}_B^{WB} the velocity of the primary star, the i -th planet and the binary companion, respectively. The evolution under the two other parts of the Hamiltonian, namely $\mathcal{H}_{\text{Int}}^{\text{WB}}$ and $\mathcal{H}_{\text{Jump}}^{\text{WB}}$, can be achieved using Eq. (2.36), since $\mathcal{H}_{\text{Int}}^{\text{WB}}$ only depends on the positions and $\mathcal{H}_{\text{Jump}}^{\text{WB}}$ on the momenta. To use those equations, one needs the derivatives of the Hamiltonian:

$$\begin{aligned}
- \frac{\partial \mathcal{H}_{\text{Int}}^{\text{WB}}}{\partial r_{l,i}^{\text{WB}}} = & - \sum_{j=3, j \neq i}^N \left[\frac{Gm_i m_j}{\|\mathbf{r}_{ij}\|^3} (r_{l,i}^{\text{WB}} - r_{l,j}^{\text{WB}}) \right] - \frac{Gm_A m_B m_i}{m_{\text{red}}} \left[\frac{r_{l,B}^{\text{WB}} + s_l}{\|\mathbf{r}_B^{\text{WB}} + \mathbf{s}\|^3} \right] \\
& - Gm_B \sum_{k=3}^N \left[\frac{m_k m_i (r_{l,B}^{\text{WB}} - r_{l,k}^{\text{WB}} + s_l)}{m_{\text{red}} \|\mathbf{r}_B^{\text{WB}} - \mathbf{r}_k^{\text{WB}} + \mathbf{s}\|^3} \right] + Gm_B \frac{m_i (r_{l,B}^{\text{WB}} - r_{l,i}^{\text{WB}} + s_l)}{\|\mathbf{r}_B^{\text{WB}} - \mathbf{r}_i^{\text{WB}} + \mathbf{s}\|^3},
\end{aligned} \tag{2.45}$$

$$\begin{aligned}
-\frac{\partial \mathcal{H}_{\text{Int}}^{\text{WB}}}{\partial r_{l,B}^{\text{WB}}} &= Gm_A m_B \left(\frac{r_{l,B}^{\text{WB}}}{\|\mathbf{r}_B^{\text{WB}}\|^3} - \frac{r_{l,B}^{\text{WB}} - s_l}{\|\mathbf{r}_B^{\text{WB}} - \mathbf{s}\|^3} \right) \\
&\quad + Gm_B \sum_{k=3}^N m_k \left(\frac{r_{l,B}^{\text{WB}}}{\|\mathbf{r}_B^{\text{WB}}\|^3} - \frac{r_{l,B}^{\text{WB}} - r_{l,k}^{\text{WB}} - s_l}{\|\mathbf{r}_B^{\text{WB}} - \mathbf{r}_k^{\text{WB}} - \mathbf{s}\|^3} \right), \quad (2.46)
\end{aligned}$$

and

$$\frac{\partial \mathcal{H}_{\text{Jump}}^{\text{WB}}}{\partial p_{l,i}^{\text{WB}}} = \frac{1}{m_A} \left[\sum_{j=3}^N p_{l,j}^{\text{WB}} \right] \quad \begin{array}{l} i = 1 \dots N \\ l = x, y, z \end{array}. \quad (2.47)$$

More details about the calculations can be found in Roisin (2017).

2.1.5.1 Close encounters between the planets

A problem arises in the case of close encounters between the planets, as explained for SyMBA in Duncan et al. (1998). Indeed, a close encounter leads to a big increase of $\mathcal{H}_{\text{Int}}^{\text{WB}}$ since it contains a term proportional to the inverse of the distance between the planets. This problem is also present in binary systems. Hence, we adopted the solution proposed by Duncan et al. (1998) adapted for binary stars. The idea is to add the problematic term of $\mathcal{H}_{\text{Int}}^{\text{WB}}$ in $\mathcal{H}_{\text{Kep}}^{\text{WB}}$, such that $\mathcal{H}_{\text{Int}}^{\text{WB}}$ remains small enough to preserve an accurate integration. The new splitting is then

$$\mathcal{H} = \mathcal{H}_{\text{Jump}}^{\text{WB}} + \mathcal{H}_{\text{IntNE}}^{\text{WB}} + \left(\mathcal{H}_{\text{IntE}}^{\text{WB}} + \mathcal{H}_{\text{Kep}}^{\text{WB}} \right), \quad (2.48)$$

where

$$\mathcal{H}_{\text{IntE}}^{\text{WB}} = - \sum_{i=3}^{N-1} \sum_{i < j \leq N} \left(\frac{Gm_i m_j}{\|\mathbf{r}_{ij}\|} H(\|\mathbf{r}_{ij}\|) \right) \quad (2.49)$$

and

$$\begin{aligned}
\mathcal{H}_{\text{IntNE}}^{\text{WB}} &= \mathcal{H}_{\text{Int}}^{\text{WB}} - \mathcal{H}_{\text{IntE}}^{\text{WB}} \quad (2.50) \\
&= - \sum_{i=3}^{N-1} \sum_{i < j \leq N} \left(\frac{Gm_i m_j}{\|\mathbf{r}_{ij}\|} (1 - H(\|\mathbf{r}_{ij}\|)) \right) \\
&\quad + Gm_A m_B \left(\frac{1}{\|\mathbf{r}_B^{\text{WB}}\|} - \frac{1}{\|\mathbf{r}_B^{\text{WB}} + \mathbf{s}\|} \right) \\
&\quad + Gm_B \sum_{i=3}^N m_i \left(\frac{1}{\|\mathbf{r}_B^{\text{WB}}\|} - \frac{1}{\|\mathbf{r}_B^{\text{WB}} - \mathbf{r}_i^{\text{WB}} + \mathbf{s}\|} \right), \quad (2.51)
\end{aligned}$$

with

$$H(r) = \begin{cases} 0 & \text{if } r > r_{\text{crit}} \\ 1 & \text{if not.} \end{cases} \quad (2.52)$$

The quantity r_{crit} is the critical distance for two bodies under which they will be considered as having a close encounter. The evolution under $\mathcal{H}_{\text{IntNE}}^{\text{WB}}$ can be achieved using Eq. (2.36) and the derivative

$$\begin{aligned}
-\frac{\partial \mathcal{H}_{\text{IntNE}}^{\text{WB}}}{\partial r_{l,i}^{\text{WB}}} &= - \sum_{j=3, j \neq i}^N \left[\frac{Gm_i m_j}{\|\mathbf{r}_{ij}\|^3} (r_{l,i}^{\text{WB}} - r_{l,j}^{\text{WB}}) H(\|\mathbf{r}_{ij}\|) \right] \\
&- \frac{Gm_A m_B m_i}{m_{\text{red}}} \left[\frac{r_{l,B}^{\text{WB}} + s_l}{\|\mathbf{r}_B^{\text{WB}} + \mathbf{s}\|^3} \right] - Gm_B \sum_{k=3}^N \left[\frac{m_k m_i (r_{l,B}^{\text{WB}} - r_{l,k}^{\text{WB}} + s_l)}{m_{\text{red}} \|\mathbf{r}_B^{\text{WB}} - \mathbf{r}_k^{\text{WB}} + \mathbf{s}\|^3} \right] \\
&+ Gm_B \frac{m_i (r_{l,B}^{\text{WB}} - r_{l,i}^{\text{WB}} + s_l)}{\|\mathbf{r}_B^{\text{WB}} - \mathbf{r}_i^{\text{WB}} + \mathbf{s}\|^3} \quad l = x, y, z. \quad (2.53)
\end{aligned}$$

Note that close encounters between a planet and the wide binary are unlikely and not considered here.

The evolution under $\mathcal{H}_{\text{IntE}}^{\text{WB}} + \mathcal{H}_{\text{Kep}}^{\text{WB}}$ is more tricky since it depends on both the position and the associated momentum of the bodies. Duncan et al. (1998) proposed to split the Hamiltonian with respect to the order of magnitude of the different terms and to adapt the time step to keep a good accuracy of the integration (since the error is proportional to the ratio between the parts of the Hamiltonian and to the square of the time step). Thus, $\mathcal{H}_{\text{IntE}}^{\text{WB}}$ is expressed as $\sum_{i=0} \mathcal{H}_{\text{IntE},i}^{\text{WB}}$ with $\mathcal{H}_{\text{IntE},i}^{\text{WB}}$ an order of magnitude smaller than $\mathcal{H}_{\text{IntE},i+1}^{\text{WB}}$. We then compute the following approximation:

$$\begin{aligned}
&\exp \left(\tau \left[\sum_{i=0} T_{\text{IntE},i}^{\text{WB}} + T_{\text{Kep}}^{\text{WB}} \right] \right) \\
&\approx \exp \left(\frac{\tau}{2} T_{\text{IntE},0}^{\text{WB}} \right) \exp \left(\tau \left[\sum_{i=1} T_{\text{IntE},i}^{\text{WB}} + T_{\text{Kep}}^{\text{WB}} \right] \right) \exp \left(\frac{\tau}{2} T_{\text{IntE},0}^{\text{WB}} \right) \quad (2.54)
\end{aligned}$$

$$\begin{aligned}
&\approx \exp \left(\frac{\tau}{2} T_{\text{IntE},0}^{\text{WB}} \right) \left\{ \exp \left(\frac{\tau}{2n} T_{\text{IntE},1}^{\text{WB}} \right) \exp \left(\frac{\tau}{n} \left[\sum_{i=2} T_{\text{IntE},i}^{\text{WB}} + T_{\text{Kep}}^{\text{WB}} \right] \right) \right. \\
&\quad \left. \exp \left(\frac{\tau}{2n} T_{\text{IntE},1}^{\text{WB}} \right) \right\}^n \exp \left(\frac{\tau}{2} T_{\text{IntE},0}^{\text{WB}} \right) \quad (2.55)
\end{aligned}$$

$$\begin{aligned}
&\approx \exp \left(\frac{\tau}{2} T_{\text{IntE},0}^{\text{WB}} \right) \left\{ \exp \left(\frac{\tau}{2n} T_{\text{IntE},1}^{\text{WB}} \right) \left\{ \exp \left(\frac{\tau}{2n^2} T_{\text{IntE},2}^{\text{WB}} \right) \right. \right. \\
&\quad \left. \left. \exp \left(\frac{\tau}{n^2} \left[\sum_{i=3} T_{\text{IntE},i}^{\text{WB}} + T_{\text{Kep}}^{\text{WB}} \right] \right) \exp \left(\frac{\tau}{2n^2} T_{\text{IntE},2}^{\text{WB}} \right) \right\}^n \exp \left(\frac{\tau}{2n} T_{\text{IntE},1}^{\text{WB}} \right) \right\}^n \\
&\quad \exp \left(\frac{\tau}{2} T_{\text{IntE},0}^{\text{WB}} \right) \quad (2.56)
\end{aligned}$$

⋮

with $T_{\text{IntE},i}^{\text{WB}}$ and $T_{\text{Kep}}^{\text{WB}}$ the linear operators associated with $\mathcal{H}_{\text{IntE},i}^{\text{WB}}$ and $\mathcal{H}_{\text{Kep}}^{\text{WB}}$, respectively. The evolution under $T_{\text{IntE},i}^{\text{WB}}$ is straightforward since it only depends on the position of the bodies. In practice, instead of splitting $T_{\text{IntE},i}^{\text{WB}}$, Duncan et al. (1998) proposed to split the derivatives:

$$-\frac{\partial \mathcal{H}_{\text{IntE}}^{\text{WB}}}{\partial r_{l,i}^{\text{WB}}} = \sum_{c=0} \left[-\frac{\partial \mathcal{H}_{\text{IntE},c}^{\text{WB}}}{\partial r_{l,i}^{\text{WB}}} \right], \quad (2.57)$$

where

$$-\frac{\partial \mathcal{H}_{\text{IntE},c}^{\text{WB}}}{\partial r_{l,i}^{\text{WB}}} = - \sum_{j=3, j \neq i}^N \left[\frac{Gm_i m_j}{\|\mathbf{r}_{ij}\|^3} \left(r_{l,i}^{\text{WB}} - r_{l,j}^{\text{WB}} \right) f_c(\|\mathbf{r}_{ij}\|) (1 - H(\|\mathbf{r}_{ij}\|)) \right] \quad l = x, y, z. \quad (2.58)$$

The partition function, f_c , is defined as

$$f_c(\|\mathbf{r}_{ij}\|) = \begin{cases} \bar{f}_c(\|\mathbf{r}_{ij}\|) - \bar{f}_{c-1}(\|\mathbf{r}_{ij}\|) & \text{if } i \in \mathbb{N}_0 \\ \bar{f}_0(\|\mathbf{r}_{ij}\|) & \text{if } i = 0, \end{cases} \quad (2.59)$$

where

$$\bar{f}_c(\|\mathbf{r}_{ij}\|) = \begin{cases} 1 & \text{if } \|\mathbf{r}_{ij}\| \geq R_c \\ g\left(\frac{R_c - \|\mathbf{r}_{ij}\|}{R_c - R_{c+1}}\right) & \text{if } R_{c+1} \leq \|\mathbf{r}_{ij}\| < R_c \\ 0 & \text{if } \|\mathbf{r}_{ij}\| < R_{c+1}, \end{cases} \quad (2.60)$$

with R_i ($i \in \mathbb{N}_0$) the boundary distances to split the problem with respect to the order of magnitude of the different parts and the function g defined as (Rauch and Holman, 1999)

$$g(r) = \frac{1}{2} \left[1 + \tanh\left(\frac{2r-1}{r(1-r)}\right) \right]. \quad (2.61)$$

The flowchart of the code for binary stars is given in Fig. 2.3. The left side of the diagram describes the classical integrator and the right side manages the close encounters between the planets.

2.1.5.2 Close encounters with the central star

A problem also arises for a close perihelion passage. In this case, $\mathcal{H}_{\text{Jump}}^{\text{WB}}$ will become of the same order as $\mathcal{H}_{\text{Kep}}^{\text{WB}}$ because of the high velocity (hence high momentum) of the body at perihelion. To overcome this problem we applied the

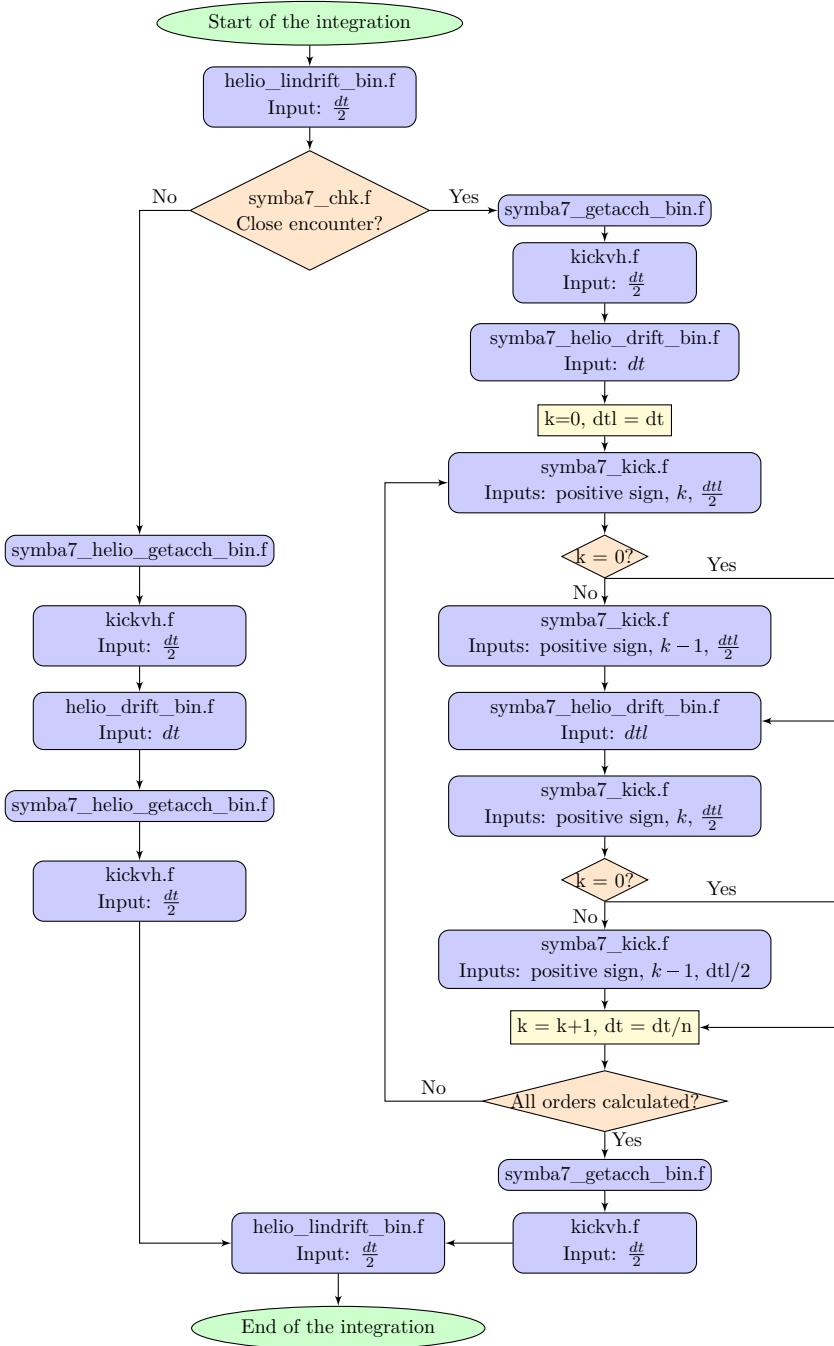


Figure 2.3 – Flowchart of the code for wide binary stars

solution proposed by Levison and Duncan (2000), adapted for binary systems. It consists in smoothly including $\mathcal{H}_{\text{Jump}}^{\text{WB}}$ in $\mathcal{H}_{\text{Kep}}^{\text{WB}}$. The new splitting is then

$$\mathcal{H} = \mathcal{H}_{\text{KepSP}}^{\text{WB}} + \mathcal{H}_{\text{Int}}^{\text{WB}} + \mathcal{H}_{\text{JumpSP}}^{\text{WB}}, \quad (2.62)$$

where

$$\begin{aligned} \mathcal{H}_{\text{KepSP}}^{\text{WB}} = & \frac{\|\mathbf{p}_B^{\text{WB}}\|^2}{2\mu_{\text{WB}}} - \frac{Gm_{\text{sys}}\mu_{\text{WB}}}{\|\mathbf{r}_B^{\text{WB}}\|} + \sum_{i=3}^N \left(\frac{\|\mathbf{p}_i^{\text{WB}}\|^2}{2m_i} - \frac{Gm_A m_B}{\|\mathbf{r}_i^{\text{WB}}\|} \right) \\ & + \frac{1}{2m_A} \left\| \sum_{i=3}^N \mathbf{p}_i^{\text{WB}} \right\|^2 F^{\text{WB}} \left(\|\mathbf{r}_3^{\text{WB}}\|^2, \|\mathbf{r}_4^{\text{WB}}\|^2, \dots, \|\mathbf{r}_N^{\text{WB}}\|^2 \right) \end{aligned} \quad (2.63)$$

and

$$\mathcal{H}_{\text{JumpSP}}^{\text{WB}} = \frac{1}{2m_A} \left\| \sum_{i=3}^N \mathbf{p}_i^{\text{WB}} \right\|^2 \left[1 - F^{\text{WB}} \left(\|\mathbf{r}_3^{\text{WB}}\|^2, \|\mathbf{r}_4^{\text{WB}}\|^2, \dots, \|\mathbf{r}_N^{\text{WB}}\|^2 \right) \right], \quad (2.64)$$

where (Levison and Duncan, 2000)

$$F^{\text{WB}} \left(\|\mathbf{r}_3^{\text{WB}}\|^2, \|\mathbf{r}_4^{\text{WB}}\|^2, \dots, \|\mathbf{r}_N^{\text{WB}}\|^2 \right) = 1 - \prod_{i=3}^N \left[1 - \tilde{f}^{\text{WB}} \left(\|\mathbf{r}_i^{\text{WB}}\|^2 \right) \right] \quad (2.65)$$

with

$$\tilde{f}^{\text{WB}} \left(\|\mathbf{r}_i^{\text{WB}}\|^2 \right) = \begin{cases} 1 & \text{if } \|\mathbf{r}_i^{\text{WB}}\|^2 < R_1^2 \\ 10 \left(\frac{R_2^2 - \|\mathbf{r}_i^{\text{WB}}\|^2}{R_2^2 - R_1^2} \right)^3 - 15 \left(\frac{R_2^2 - \|\mathbf{r}_i^{\text{WB}}\|^2}{R_2^2 - R_1^2} \right)^4 \\ \quad + 6 \left(\frac{R_2^2 - \|\mathbf{r}_i^{\text{WB}}\|^2}{R_2^2 - R_1^2} \right)^5 & \text{if } R_1^2 < \|\mathbf{r}_i^{\text{WB}}\|^2 < R_2^2 \\ 0 & \text{if } \|\mathbf{r}_i^{\text{WB}}\|^2 > R_2^2, \end{cases} \quad (2.66)$$

and R_1 and R_2 the boundary limits for the transition region. The evolution under those two new parts of the Hamiltonian can no longer be performed by analytical calculation, and a Bulirsch-Stoer integration (see, e.g. Press et al., 1992) for the new Hamiltonian equations is achieved:

$$\begin{cases} \frac{dr_{l,i}^{\text{WB}}}{dt} = \frac{1}{m_A} \left[\sum_{j=3}^N p_{l,j}^{\text{WB}} \right] \left[1 - F^{\text{WB}} \left(\|\mathbf{r}_3^{\text{WB}}\|^2, \|\mathbf{r}_4^{\text{WB}}\|^2, \dots, \|\mathbf{r}_N^{\text{WB}}\|^2 \right) \right] \\ \frac{dp_{l,i}^{\text{WB}}}{dt} = \frac{r_{l,i}^{\text{WB}}}{m_A} \left\| \sum_{j=3}^N \mathbf{p}_j^{\text{WB}} \right\|^2 \frac{\partial \left[\tilde{f}^{\text{WB}} \left(\|\mathbf{r}_i^{\text{WB}}\|^2 \right) \right]}{\partial \|\mathbf{r}_i^{\text{WB}}\|^2} \prod_{j=3, j \neq i}^N \left[1 - \tilde{f}^{\text{WB}} \left(\|\mathbf{r}_j^{\text{WB}}\|^2 \right) \right] \end{cases} \quad \begin{matrix} i = 3 \dots N \\ l = x, y, z \end{matrix} \quad (2.67)$$

for the evolution under $\mathcal{H}_{\text{JumpSP}}^{\text{WB}}$ and

$$\left\{ \begin{array}{l} \frac{dr_{l,i}^{\text{WB}}}{dt} = \frac{p_{l,i}^{\text{WB}}}{m_i} + \frac{1}{m_A} \left[\sum_{j=3}^N p_{l,j}^{\text{WB}} \right] F^{\text{WB}} \left(\|\mathbf{r}_3^{\text{WB}}\|^2, \|\mathbf{r}_4^{\text{WB}}\|^2, \dots, \|\mathbf{r}_N^{\text{WB}}\|^2 \right) \\ \frac{dp_{l,i}^{\text{WB}}}{dt} = \frac{Gm_A m_i}{\|\mathbf{r}_i^{\text{WB}}\|^3} r_{l,i}^{\text{WB}} + \frac{r_{l,i}^{\text{WB}}}{m_A} \left\| \sum_{j=3}^N \mathbf{p}_j^{\text{WB}} \right\|^2 \\ \frac{\partial \left[\tilde{f}^{\text{WB}} \left(\|\mathbf{r}_i^{\text{WB}}\|^2 \right) \right]}{\partial \|\mathbf{r}_i^{\text{WB}}\|^2} \prod_{j=3, j \neq i}^N \left[1 - \tilde{f}^{\text{WB}} \left(\|\mathbf{r}_j^{\text{WB}}\|^2 \right) \right] \end{array} \right. \quad \begin{array}{l} i = 3 \dots N \\ l = x, y, z \end{array}, \quad (2.68)$$

for the evolution under $\mathcal{H}_{\text{KepSP}}^{\text{WB}}$ with

$$\frac{\partial \left[\tilde{f}^{\text{WB}} \left(\|\mathbf{r}_i^{\text{WB}}\|^2 \right) \right]}{\partial \|\mathbf{r}_i^{\text{WB}}\|^2} = \left\{ \begin{array}{ll} -30 \frac{\left(R_2^2 - \|\mathbf{r}_i^{\text{WB}}\|^2 \right)^2}{\left(R_2^2 - R_1^2 \right)^3} + 60 \frac{\left(R_2^2 - \|\mathbf{r}_i^{\text{WB}}\|^2 \right)^3}{\left(R_2^2 - R_1^2 \right)^4} & \\ -30 \frac{\left(R_2^2 - \|\mathbf{r}_i^{\text{WB}}\|^2 \right)^4}{\left(R_2^2 - R_1^2 \right)^5} & \text{if } R_1^2 < \|\mathbf{r}_i^{\text{WB}}\|^2 < R_2^2 \\ 0 & \text{if not.} \end{array} \right. \quad (2.69)$$

Note that the evolution of the binary companion is not affected by close perihelion passage in our study. In addition, if there are both a close encounter between planets and a close perihelion passage, the two solutions can be combined and the system evolves under $\mathcal{H}_{\text{IntE}}^{\text{WB}} + \mathcal{H}_{\text{KepSP}}^{\text{WB}}$, $\mathcal{H}_{\text{IntNE}}^{\text{WB}}$, and $\mathcal{H}_{\text{JumpSP}}^{\text{WB}}$.

2.2 Migration code

In the code, we also implemented the Type-II migration of giant planets in the protoplanetary disk. The migration is mimicked by a suitable Stokes-type drag force added in the equations of motion of the planets. Instead of a simplistic K-prescription, we adopted the damping formulas for eccentricity and inclination provided by the 3D hydrodynamical simulations of protoplanetary disks with embedded high-mass planets of Bitsch et al. (2013). These formulas were previously used in the PhD thesis of S. Sotiriadis on the formation of extrasolar systems around single stars (Sotiriadis, 2017) and are described in detail in the following.

2.2.1 Giant planet migration

The migration of giant planets in the Type-II regime, due to angular momentum exchange with the disk, is on a similar timescale as the viscous accretion time. However, when the mass of the planet is comparable to the mass of the material in its vicinity, the migration rate scales with the ratio of the planetary mass over the local disk mass (Ivanov et al., 1999; Nelson et al., 2000; Crida and Morbidelli, 2007). Thus, the acceleration of the migrating planet is given by (Papaloizou and Larwood, 2000)

$$\mathbf{a}_{\text{mig}} = -\frac{\mathbf{v}_{\text{pl}}}{\tau_{\text{mig}}}, \quad (2.70)$$

with \mathbf{v}_{pl} the velocity of the migrating planet and τ_{mig} the timescale for Type-II regime (disk-dominated case and planet-dominated case, see Sotiriadis et al. (2017) for more details)

$$\tau_{\text{mig}} = \frac{2}{3}\alpha^{-1}h^{-2}\Omega_{\text{pl}}^{-1} \times \max\left\{1, \frac{m_{\text{pl}}}{(4\pi/3)\Sigma(r_{\text{pl}})r_{\text{pl}}^2}\right\}, \quad (2.71)$$

with $\alpha = 0.005$ the classical value for the Shakura-Sunyaev viscosity parameter (Shakura and Sunyaev, 1973), $h = 0.05$ the disk aspect ratio, $\Omega_{\text{pl}}^{-1} = 2\pi a_{\text{pl}}^{(-3/2)}$ the orbital frequency of the planet, a_{pl} the semi-major axis of the planet, m_{pl} the mass of the planet, r_{pl} the distance of the planet to the host star, and $\Sigma \propto r^{-\gamma} = r^{-0.5}$ the surface density profile of the disk. Unless otherwise stated, in the simulations, we fix the disk inner and outer edges to $R_{\text{in}} = 0.05$ AU and $R_{\text{out}} = 30$ AU. The local disk mass will be considered as the mass of the disk between $0.2a_{\text{pl}}$ and $2.5a_{\text{pl}}$. The code also includes a smooth transition in the gas-free inner cavity using an hyperbolic tangent function $\tanh\left(\frac{r-R_{\text{in}}}{\Delta r}\right)$ where $\Delta r = 0.001$ AU, following Matsumoto et al. (2012).

2.2.2 Influence on the eccentricity and inclination

To estimate the damping of the disk on the planetary eccentricity, a possibility is to use the K-prescription (Tanaka and Ward, 2004)

$$\frac{\dot{e}}{e} = -K \left| \frac{\dot{a}}{a} \right|, \quad (2.72)$$

where K is an arbitrary parameter, generally assumed between 1 and 100. However, through hydrodynamical simulations, Bitsch et al. (2013) determined new formulas for the influence of the disk on the eccentricity and inclination without this arbitrary parameter. They fitted the evolution of a massive giant

planet in the disk to obtain approached analytical formulas for the eccentricity and inclination damping.

The eccentricity damping function depends on the planet mass m_{pl} (expressed in Jupiter mass), the eccentricity e_{pl} and the inclination i_{pl} (in degrees), and is given by (Bitsch et al., 2013)

$$\frac{de}{dt}(m_{\text{pl}}, e_{\text{pl}}, i_{\text{pl}}) = -\frac{m_{\text{ld}}}{0.025m_A} \left(a_e \left[i_{\text{pl}} + \frac{m_{\text{pl}}}{3} \right]^{-2b_e} + c_e i_{\text{pl}}^{-2d_e} \right)^{-\frac{1}{2}} + 12.65 \frac{m_{\text{pl}} m_{\text{ld}}}{m_A^2} e_{\text{pl}} \exp \left(- \left[\frac{i_{\text{pl}}}{m_{\text{pl}}} \right]^2 \right), \quad (2.73)$$

with a_{pl} the semi-major axis of the planet, m_{ld} the local mass of the disk, m_A the mass of the central star, and with coefficients

$$a_e = 80e_{\text{pl}}^{-2} \exp \left\{ -e_{\text{pl}}^2 \frac{m_{\text{pl}}}{0.26} \right\} 15^{m_{\text{pl}}} (20 + 11m_{\text{pl}} - m_{\text{pl}}^2), \quad (2.74)$$

$$b_e = 0.3m_{\text{pl}}, \quad (2.75)$$

$$c_e = 450 + 2^{m_{\text{pl}}}, \quad (2.76)$$

and

$$d_e = -1.4 + \frac{\sqrt{m_{\text{pl}}}}{6}. \quad (2.77)$$

To include the damping in the code, we converted it in an acceleration according to the formula (Papaloizou and Larwood, 2000)

$$\mathbf{a}_{\text{ecc}} = -2 \frac{(\mathbf{v}_{\text{pl}} \cdot \mathbf{r}_{\text{pl}}) \mathbf{r}_{\text{pl}}}{\|\mathbf{r}_{\text{pl}}\|^2 \tau_{\text{ecc}}}, \quad (2.78)$$

where \mathbf{v}_{pl} and \mathbf{r}_{pl} are the velocity and the position of the planet, respectively, and

$$\tau_{\text{ecc}} = \left| \frac{e_{\text{pl}}}{de/dt} \right|. \quad (2.79)$$

The damping function for inclination is given, in degrees per orbit, by

$$\frac{di}{dt}(m_{\text{pl}}, e_{\text{pl}}, i_{\text{pl}}) = -\frac{m_{\text{ld}}}{0.025m_A} \left(a_i i_{\text{pl}}^{-2b_i} \exp \left(\frac{-(i_{\text{pl}}/g_i)^2}{2} \right) + c_i \left[\frac{i_{\text{pl}}}{40} \right]^{-2d_i} \right)^{-\frac{1}{2}}, \quad (2.80)$$

with

$$a_i = 1.5 \times 10^4 (2 - 3e_{\text{pl}}) m_{\text{pl}}^3, \quad (2.81)$$

$$b_i = 1 + \frac{m_{\text{pl}} e_{\text{pl}}^2}{10}, \quad (2.82)$$

$$c_i = \frac{1.2 \times 10^6}{(2 - 3e_{\text{pl}}) \left(5 + e_{\text{pl}}^2 [m_{\text{pl}} + 2]^3 \right)}, \quad (2.83)$$

$$d_i = -3 + 2e_{\text{pl}}, \quad (2.84)$$

and

$$g_i = \sqrt{\frac{3m_{\text{pl}}}{e_{\text{pl}} + 0.001}}. \quad (2.85)$$

In both formulas (2.73) and (2.80), the time is expressed in orbital period. As mentioned in Sotiriadis et al. (2017), there is a problem when $2 - 3e_{\text{pl}} < 0$. Indeed, in this case, a_i and c_i become negative and the square root of a negative number has to be computed. In this case we adopted the solution proposed in Sotiriadis et al. (2017) and the value of $2 - 3e_{\text{pl}}$ is set to 10^{-5} .

As with the eccentricity, we converted the damping in terms of acceleration (Papaloizou and Larwood, 2000)

$$\mathbf{a}_{\text{inc}} = -2 \frac{(\mathbf{v}_{\text{pl}} \cdot \mathbf{k}) \mathbf{k}}{\tau_{\text{inc}}}, \quad (2.86)$$

where \mathbf{k} is the unitary vertical vector and

$$\tau_{\text{inc}} = \left| \frac{i_{\text{pl}}}{di/dt} \right|. \quad (2.87)$$

When considering planetary systems with two or more planets (Chapter 5), only the outer planet is assumed to migrate, as in Libert and Tsiganis (2009b) and Sotiriadis et al. (2017). As a result, the influence of the disk on the planets is modelled by

$$\mathbf{a}_{\text{disk}} = \mathbf{a}_{\text{mig}} + \mathbf{a}_{\text{ecc}} + \mathbf{a}_{\text{inc}} \quad (2.88)$$

for the outer planet and

$$\mathbf{a}_{\text{disk}} = \mathbf{a}_{\text{ecc}} + \mathbf{a}_{\text{inc}} \quad (2.89)$$

for the other planets. The evolutionary equation of the velocity is thus

$$\mathbf{v}(t_{k+1}) = \mathbf{v}(t_k) + \tau \mathbf{a}_{\text{disk}}, \quad (2.90)$$

where τ is the time step.

The evolution is implemented symmetrically in SyMBA in the same way as in Lee and Peale (2002):

$$f(t_{k+1}) = E_{\text{disk}}\left(\frac{\tau}{2}\right) \exp(T\tau) E_{\text{disk}}\left(\frac{\tau}{2}\right) f(t_k), \quad (2.91)$$

where T is the linear operator associated to the Hamiltonian \mathcal{H} of the N -body system without the disk and $E_{\text{disk}}(\cdot)$ is the evolution due to the disk. In practice, we will apply the evolution due to the disk for a half time step, then the evolution of the N -body system for a full time step and again the evolution due to the disk for another half time step.

2.2.3 Disk model

Following Sotiriadis et al. (2017), we use an exponential decay for the disk, where we decrease its mass exponentially through the evolution of the system, with a dispersal time of around 1 Myr. The surface density profile Σ is given by

$$\Sigma(r) = \Sigma_0 r^{-\gamma} \quad (2.92)$$

with Σ_0 evolving during the simulation through the equation

$$\Sigma_0(t) = \Sigma_0(0) e^{-\frac{t}{T_0}}, \quad (2.93)$$

where T_0 is a fixed parameter. The total mass of the disk is then given by

$$m_{\text{disk}}(t) = m_{\text{disk}}(0) e^{-\frac{t}{T_0}}, \quad (2.94)$$

where $m_{\text{disk}}(0)$ is the initial mass of the disk. The disk will be considered as dissipated and the interaction will then be neglected when

$$\left| \frac{dm_{\text{disk}}(t)}{dt} \right| = m_{\text{disk}}(0) \frac{e^{-\frac{t}{T_0}}}{T_0} \quad (2.95)$$

is smaller than a critical value fixed to $10^{-9} m_A/\text{yr}$ in our simulations.

More complex disk models exist, taking into account the accretion of the disk onto the star and/or the photoevaporation by radiation from the central star. We refer to Williams and Cieza (2011); Armitage (2019) for more details. Since we aim to study the influence on the planetary evolution of a binary companion rather than the influence of the disk model, the consideration of more complex disk mass decays is left for further work.

2.3 Conclusions

In this chapter we presented the symplectic integrator for wide binary star systems used in this study. We also introduced formulas for the Type-II migration of the planets in the protoplanetary disk as well as the disk eccentricity and inclination damping acting on the planets.

Using this code, we will investigate in the next chapter the migration of a single planet under the perturbation of a wide binary companion to see how the disk and binary effects compete during the protoplanetary disk phase and influence the long-term dynamical evolution of the planet.

Part II

One-planet systems

Chapter 3

Evolution of a migrating giant planet in the presence of an inclined binary companion

3.1 Introduction

In this chapter, we perform a dynamical study of the influence of a wide binary companion on the evolution of a single giant planet migrating in the protoplanetary disk in the Type-II regime. We particularly focus on how the Lidov-Kozai resonance articulates with the planetary migration when the stellar companion is highly inclined. Using the symplectic N -body code presented in Chapter 2, including eccentricity and inclination damping formulas to properly model the influence of the disk during the migration of the planet, we carry out 3200 numerical simulations with different initial eccentricity and inclination values of the binary companion. We follow the evolution of the giant planet when embedded in the protoplanetary disk and pursue the analysis well after the dispersal of the disk.

The chapter is organized as follows. In Section 3.2, the initial settings of the simulations are described. In Section 3.3, we present the results of the simulations by describing typical planetary evolutions as well as the final parameter distributions for the planet. In order to dynamically characterize the planetary evolutions, the results are discussed using a quadrupolar Hamiltonian approach in Section 3.4. Finally, our conclusions are given in Section 3.5.

3.2 Set-up of the simulations

In this chapter, we focus on the evolution of a giant planet embedded in a protoplanetary disk undergoing Type-II migration around one of the two stars of a wide binary star system (S-type planet). We denote with subscripts 0 for the central star, and B for the binary companion. The initial parameters of the simulations are described in the following.

Let us recall that for our study we adapted the SyMBA N -body code (Duncan et al., 1998) to wide binaries by following the strategy of Chambers et al. (2002), based on a new set of coordinates (wide-binary coordinates). Since we focus here on one-planet systems, we do not consider the part of the code designed for close encounters presented in Section 2.1.5.1 as well as the planetary interactions modeled through the first term of Eq. (2.41). The N -body code also includes the Type-II migration of the giant planet caused by the angular momentum exchange with the protoplanetary gas disk (Goldreich and Tremaine, 1979), mimicked by a suitable Stokes-type drag force added in the equations of motion. Regarding the damping of the planetary eccentricity and inclination caused by the disk, we adopted the damping formulas of Bitsch et al. (2013) achieved by three-dimensional hydrodynamical simulations of protoplanetary disks with embedded high-mass planets. The analytical formulas depend on the local mass disk, planetary mass, eccentricity, and inclination evaluated throughout the integration. These formulas are conceived for planets between $1 M_{\text{Jup}}$ and $10 M_{\text{Jup}}$ (where M_{Jup} denotes the mass of Jupiter). We note that it is rather unclear if a highly inclined planet continues to migrate on a viscous accretion timescale. Nevertheless, we adopted this recipe since, when initially embedded in the disk, the planet only occasionally reached high inclination with respect to the disk plane during the protoplanetary disk phase (only a few simulations are concerned and only for a very brief period of time). No inclination damping is applied when $i < 0.5^\circ$. For more details about the code, we refer to Chapter 2.

The initial disk mass in our simulations is fixed to $8 M_{\text{Jup}}$ and decreases exponentially through the evolution of the system, with a dispersal time of ~ 1 Myr. The self-gravity of the disk is not considered in this chapter.

The time step of our simulations is fixed to 0.001 yr during the migration phase and 0.01 yr after the dispersal of the disk, since the evolution of the system is then characterized by secular effects. The simulations are followed for 100 Myr.

The initial orbital elements and masses for the planet and the binary star adopted in the simulations are summarized in Table 3.1. These are expressed in the disk plane reference frame. The wide binary companion has a mass of $1 M_\odot$ and is located at 500 AU. The planetary mass m , eccentricity e , inclination

Table 3.1 – Initial parameters of the simulations. The orbital elements are associated with heliocentric coordinates with respect to the disk plane.

	Central star	Planet	Binary companion
mass	$1 M_{\odot}$	$U[1;5] M_{\text{Jup}}$	$1 M_{\odot}$
a (AU)		15	500
e		$U[0.001;0.01]$	$10^{-5}, 0.1, 0.3, 0.5$
i ($^{\circ}$)		$U[0.01;0.1]$	$10^{-5}, 10, 20, 30, 40,$ 50, 60, 70
Ω ($^{\circ}$)		10^{-5}	10^{-5}
ω ($^{\circ}$)		$U[0;180]$	10^{-5}
M ($^{\circ}$)		10^{-5}	10^{-5}

i , and argument of the pericenter ω follow a uniform distribution. For the binary companion, we considered four values of the eccentricity e_B (namely $10^{-5}, 0.1, 0.3$, and 0.5) as well as eight values of the inclination i_B (from $\sim 0^{\circ}$ up to 70°). In total, by picking randomly 100 values for each uniform distribution, we carried out 3200 simulations. The dynamical evolutions observed in the simulations are presented in the next section.

3.3 Results

In this section, we describe in detail the long-term evolutions of the planets as well as their orbital characteristics at the end of the simulations. Particular attention is given to the capture in the Lidov-Kozai resonance in the case of highly inclined binary companions.

3.3.1 Lidov-Kozai resonance

In our simulations, a strong influence of the wide binary companion is observed on the evolution of the planet embedded in the protoplanetary disk, especially for highly inclined binary companions for which the Lidov-Kozai mechanism comes into play (Lidov, 1962; Kozai, 1962). When referred to the invariant plane orthogonal to the total angular momentum of the system (also called the Laplace plane), the planet in a Lidov-Kozai resonant state exhibits coupled variations in eccentricity and inclination as well as a libration of the pericenter argument around $\pm 90^{\circ}$. We note that the large orbital variations associated with the Lidov-Kozai resonance take place in a coherent way such that the long-term stability of the system is assured. A typical example of a Lidov-Kozai evolution is shown in Fig. 3.1, for an inclination $i_B = 70^{\circ}$ of the

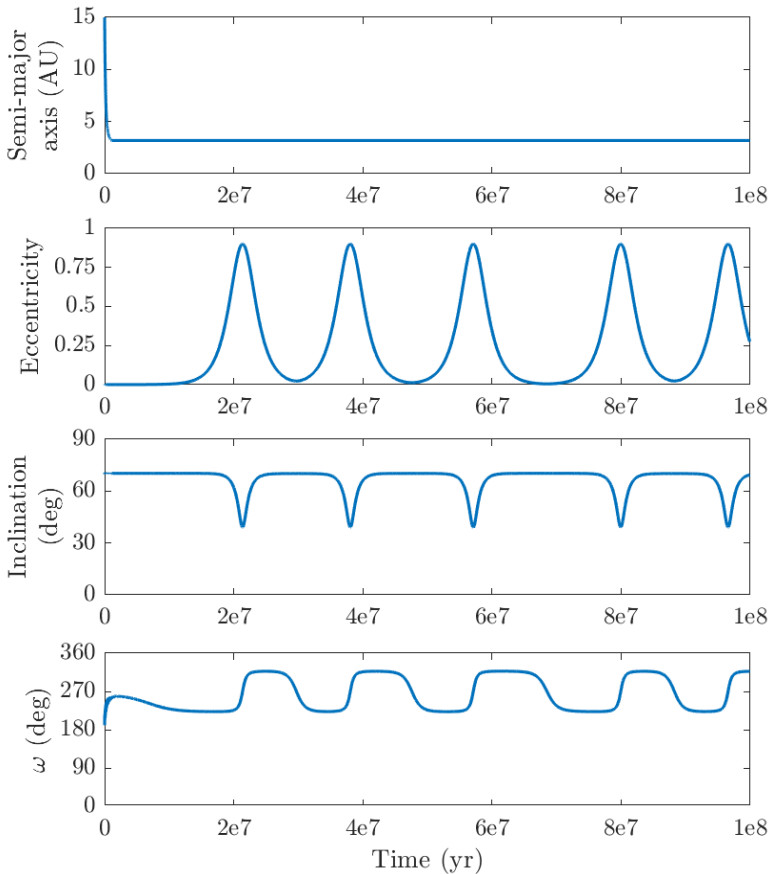


Figure 3.1 – Typical evolution of a Lidov-Kozai resonant system (libration of the pericenter argument in the invariant plane reference frame). The initial parameters are $m = 2.02 M_{\text{Jup}}$, $\omega = 16^\circ$, $e_B = 0.3$, and $i_B = 70^\circ$.

binary companion with respect to the disk plane. This inclination value is higher than the critical value $\arccos \sqrt{3/5} \approx 39.23^\circ$ introduced by Kozai (1962) for the restricted three-body problem. After the migration phase, the planet is rapidly captured in a Lidov-Kozai resonance, as indicated by the libration of the pericenter argument observed in the last panel of Fig. 3.1, and high eccentricity and inclination variations are observed.

It is important to note that the libration of the pericenter argument in the invariant plane reference frame is the proper criteria for the identification of the Lidov-Kozai resonant regime among the simulations (Libert and Tsiganis, 2009b). High eccentricity and inclination variations can also be observed when the planet is not in a Lidov-Kozai resonant state, as shown in Fig. 3.2. While

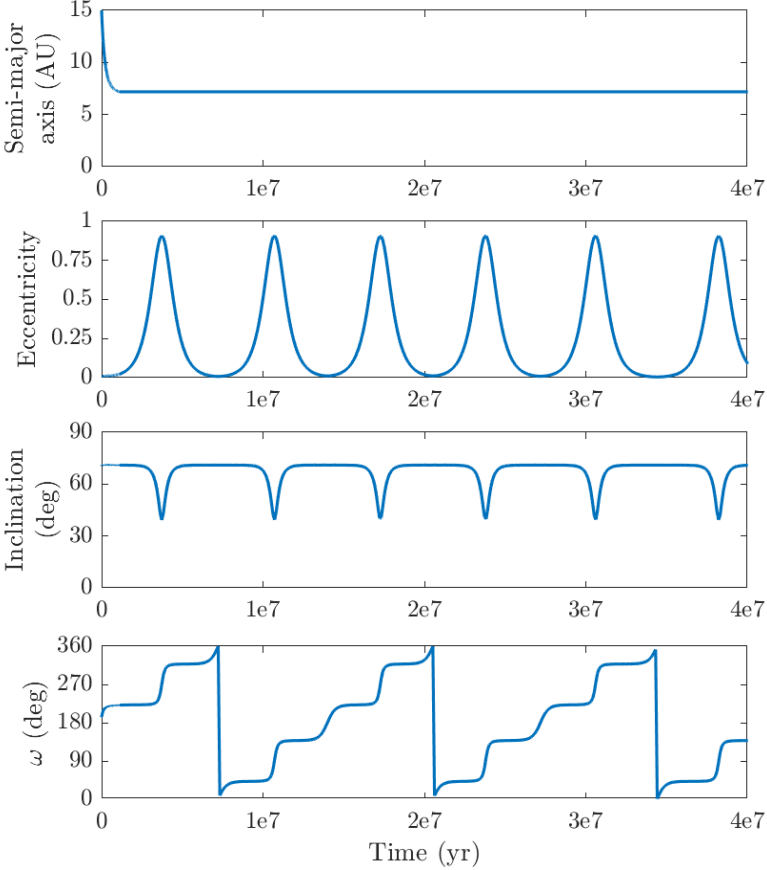


Figure 3.2 – Typical evolution of a planet that undergoes high eccentricity and inclination variations, while not in a Lidov-Kozai resonance (circulation of the pericenter argument in the invariant plane reference frame). The initial parameters are $m = 4.34 M_{\text{Jup}}$, $\omega = 13^\circ$, $e_B = 10^{-5}$, and $i_B = 70^\circ$.

the planet does experience large variations in eccentricity and inclination, the argument of the pericenter circulates (see the last panel of Fig. 3.2). For this reason, all the dynamical evolutions displayed in the following are presented in the invariant plane reference frame.

Note that, in practice, a planet will be considered here as locked in the Lidov-Kozai resonance if a libration of the argument of the pericenter is observed at the end of the simulation during three Lidov-Kozai cycles (for the calculation of the period, see, e.g. Innanen et al. (1997)) or, in case it exceeds the timescale of the simulation, during the last 8×10^7 yr.

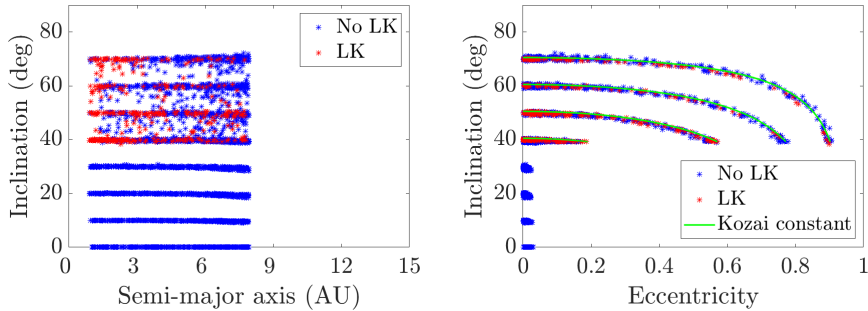


Figure 3.3 – Inclination of the planets as a function of the semi-major axis (left panel) and the eccentricity (right panel) at the end of the simulations (100 Myr). The planets evolving in the Lidov-Kozai resonance are drawn in red.

3.3.2 Final distributions

In this section, we describe the orbital parameters of the planets at the end of the simulations (i.e., 100 Myr). We recall that all the planetary orbital parameters are given in the invariant plane reference frame. Fig. 3.3 shows the planetary inclination as a function of the semi-major axis and the eccentricity. The color code indicates if the planet is in a Lidov-Kozai resonance state at the end of the evolution.

As seen in the left panel of Fig. 3.3, all the planets end up with a semi-major axis that is smaller than 10 AU as a result of the Type-II migration of the planets during the protoplanetary disk phase. The planets found locked in a Lidov-Kozai resonant state (red stars) all have an inclination (with respect to the invariant plane) that is higher than $\sim 40^\circ$, which comes as no surprise considering the critical value of 39.23° for the establishment of the Lidov-Kozai resonance. Nevertheless, the highly inclined planets are not all in a Lidov-Kozai resonant state at the end of the simulations, as shown by the color code.

The critical inclination value is even more obvious in the right panel of Fig. 3.3, where the planetary inclinations are presented jointly with the eccentricities. While a pile-up around low eccentricities is observed at low planetary inclinations, high eccentricities are only associated with inclinations above $\sim 40^\circ$. However, although the Lidov-Kozai resonance could contribute to the excitation of the planetary eccentricities, we note that only a small fraction of the planets evolves in a Lidov-Kozai resonance at the end of the simulations. The percentages of final Lidov-Kozai resonant evolutions found among the 3200 simulations are given in Table 3.2, for each initial inclination value of the binary companion. Let us remark that the percentages of resonance captures are

Table 3.2 – Percentages of systems in a final Lidov-Kozai resonant state, for the different inclinations of the binary companion i_B .

i_B ($^\circ$)	Lidov-Kozai (%)
≤ 30	0
40	43
50	50
60	26
70	25

slightly lower when the simulations do not include the disk phase. It seems to indicate that the migration in the disk promotes the establishment of Lidov-Kozai resonant systems. Additionally, we note that the values in eccentricity and inclination displayed in Fig. 3.3 follow particular curves (green lines) whose trend will be discussed in Section 3.4.

Since the argument of the pericenter plays a key role in the Lidov-Kozai mechanism, we therefore pay particular attention to this angle in the following. Fig. 3.4 shows the normalized distribution of the argument of the pericenter of the planets at the end of the simulations. We clearly observe two pile-ups around 90° and 270° . Interestingly, the highest peaks are found at the borders of the two pile-ups, namely for pericenter arguments close to 45° , 135° , 225° , and 315° . In the left panel of Fig. 3.4, the systems in a Lidov-Kozai resonance belong to the pile-ups at 90° and 270° , as expected. In the right panel of Fig. 3.4, the color code of the histogram refers to the initial inclination values of the binary companion i_B . We can deduce from the plot that the pile-ups are formed by the highly inclined binary companions ($i_B \geq 40^\circ$), since the normalized frequencies of the pericenter arguments for planets with a binary companion initially below 40° are almost uniformly distributed.

Finally, in Fig. 3.5, we present the inclination of the planet as a function of the argument of the pericenter, at the end of the simulation, with the same color codes as in Fig. 3.4. We note the existence of two arc-shaped curves. The Lidov-Kozai resonant systems mainly lie around these two curves, as observed in the left panel. In the right panel, we see that the two arc-shaped curves mostly correspond to planets with highly inclined binary companions. We note that the accumulations observed at the borders of the two pile-ups in the histograms of Fig. 3.4 can be connected with the particular shape of these curves. The edges of the arc-shaped curves are nearly parallel to the y -axis and thus more systems are gathered at the edges rather than in the central part of the curves (i.e., around 90° and 270°) when considering parts of the x -axis of the same length.

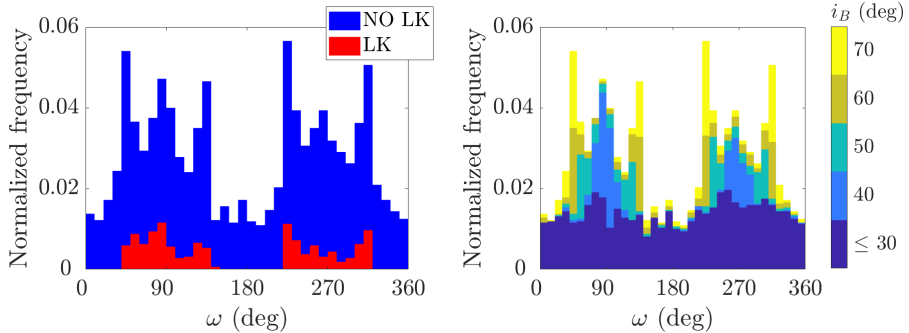


Figure 3.4 – Normalized distribution of the pericenter argument of the planet, at the end of the simulation (100 Myr). The color codes refer to planets evolving in the Lidov-Kozai resonance in the left panel (red color) and to the initial inclination of the binary companion i_B in the right panel.

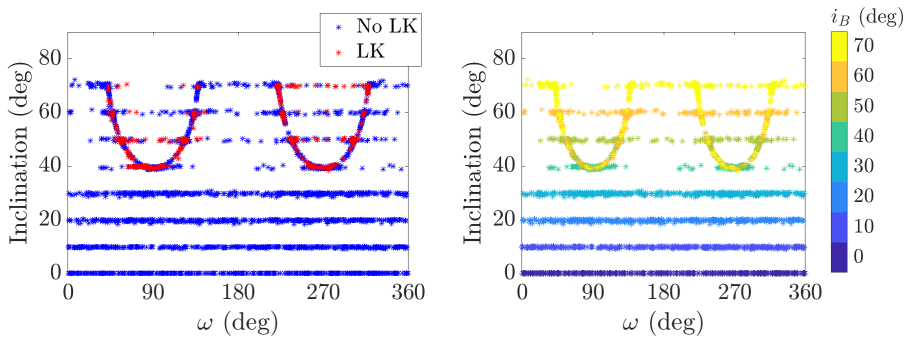


Figure 3.5 – Inclination of the planet as a function of the argument of the pericenter, at the end of the simulation (100 Myr). The color codes refer to planets evolving in the Lidov-Kozai resonance in the left panel (red color) and to the initial inclination of the binary companion i_B in the right panel.

3.3.3 Initial conditions leading to Lidov-Kozai resonance

We might wonder whether it is possible to identify the initial planetary orbital elements leading to a Lidov-Kozai resonant state for the planet. As can be deduced from Table 3.2, approximately 36% of the planets with a binary companion inclined at more than 40° end up trapped in a Lidov-Kozai resonance at the end of the simulation. A statistical analysis of the initial parameters of these systems was performed, but no trend was observed. In particular, the initial values of the pericenter argument of the planets captured in the Lidov-Kozai resonance follow an uniform distribution. This is further illustrated in

the evolutions of Fig. 3.1 and Fig. 3.2, which have close initial values of the arguments of pericenter but different resonant behaviors.

Moreover, we carried out a study of the specific time of the capture in the Lidov-Kozai resonance. We present in Fig. 3.6 the same plot as in the left panel of Fig. 3.5, but for different times. The top panel shows the planetary inclination versus the pericenter argument values at half of the disk lifetime (0.55 Myr), the middle panel at the dispersal of the disk (1.1 Myr) and the bottom panel at the end of the simulation (100 Myr). We clearly see the accumulation of the planets around the arc-shaped curves through time. Interestingly, the planets firstly gather in the left part of the curves (i.e., around a pericenter argument of 45° and 135°) during the disk phase and spread along the curves in a second phase.

3.4 Dynamical analysis

In this section, we give a dynamical interpretation of the arc-shaped curves observed in Fig. 3.5. To describe the dynamics of the migrating planets, we draw phase portraits of a simplified Hamiltonian formulation and follow the trajectory of the planets on this portrait until their final location.

Following the work of Bataille et al. (2018), we used a quadrupolar Hamiltonian approach (i.e., the dominating terms of the secular Hamiltonian) that has one degree of freedom and states as follows:

$$\mathcal{H} = - \left(5 - 3 \frac{h^2}{\cos^2 i} \right) (1 - 3 \cos^2 i) + 15 \left(1 - \frac{h^2}{\cos^2 i} \right) (1 - \cos^2 i) \cos(2\omega). \quad (3.1)$$

Since the angular momentum of the wide binary orbit is much greater than that of the planetary orbit, the dimensionless angular momentum of the planet $h = \sqrt{1 - e^2} \cos i$ is nearly constant and is usually referred to as the Kozai constant. For a given value of the Kozai constant, phase portraits of the dynamics can be drawn, consisting of level curves of the Hamiltonian in the plane (ω, e) (or equivalently (ω, i)).

For a low value of the inclination of the binary companion, the Hamiltonian curves in the plane (ω, e) are nearly straight lines. An example of such an evolution is shown in Fig. 3.7, for an inclination of 30° for the companion star. In the left panel, we see that no significant eccentricity and inclination variation is observed during the long-term evolution of the planet. This evolution is overplotted on the phase portrait given in the right panel of Fig. 3.7. The time evolution is indicated by the color scale, while the initial planetary parameters are denoted with a magenta star symbol. The value of the Kozai constant h used to compute the phase portrait is fixed to the mean value of h after the

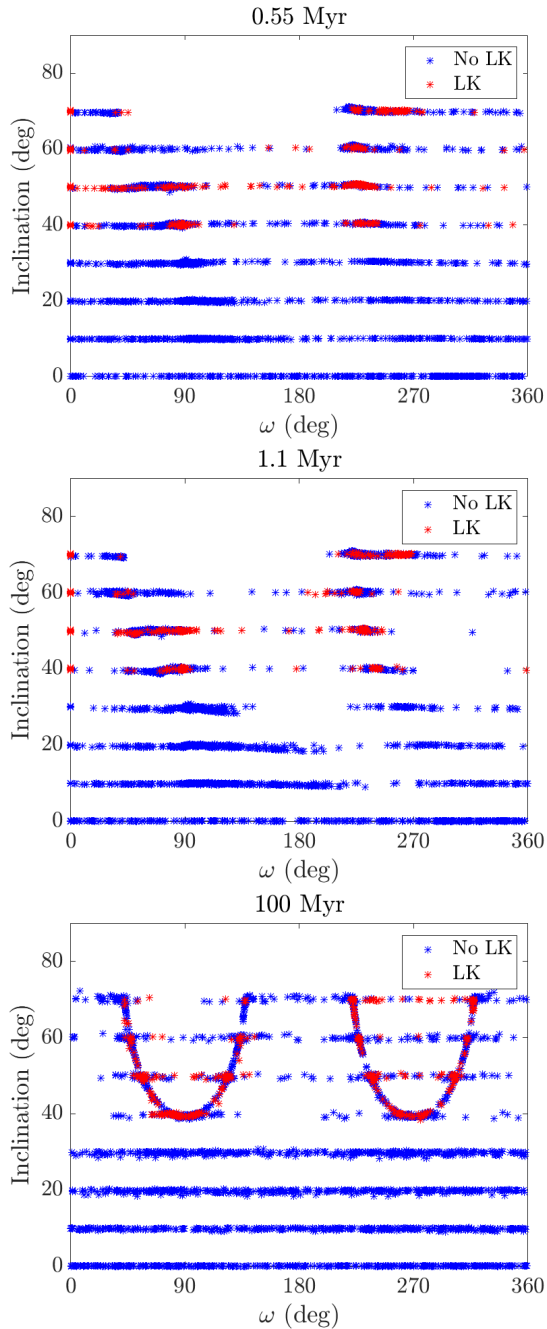


Figure 3.6 – Same as Fig. 3.5, for different times: 0.55 Myr (half of the disk lifetime) in the top panel, 1.1 Myr (dispersal of the disk) in the middle panel, and 100 Myr (end of the simulation) in the bottom panel.

migration phase. Thus, at the beginning (dark blue points), the planetary evolution can depart from the Hamiltonian curves represented on the phase portrait (since the system is dissipative owing to the migration), but after the migration phase the trajectory of the planet evolves on a fixed level curve of the analytical model. In Fig. 3.7, the planet follows a quasi-straight line of constant Hamiltonian, as expected.

For systems with a highly inclined companion ($i_B \geq 40^\circ$), the phase space shows the Lidov-Kozai resonance islands that strongly influence the dynamical behavior of the planet. Two typical dynamical outcomes are observed in the simulations and these are both illustrated in Fig 3.8. In the top panel, we show the phase portrait for the system of Fig. 3.1, for which a capture around the Lidov-Kozai equilibrium around 90° takes place. The evolution of the system of Fig. 3.2 is represented on the phase space of the bottom panel. No capture in the Lidov-Kozai resonance is observed, and the planet evolves around the two islands with its pericenter argument circulating. Finally, we note that in both cases the planets spend time in libration or circulation around the Kozai equilibria. This gives an explanation for the arc-shaped curves observed in the final distribution of the simulations in Fig. 3.5.

Having a careful look to the two phase spaces of Fig. 3.8, one could expect that the points along the horizontal lines inside the two arc-shaped curves in Fig. 3.5 are associated with Lidov-Kozai resonant motion (red color). The blue points on the horizontal lines correspond to planets that alternate between phases of Lidov-Kozai resonant captures and phases of circulation around the islands. An example of such an evolution is represented on Fig. 3.9. The planet is first captured around the island centred on $\omega = 90^\circ$ at the dispersal of the disk, then after some cycles leaves the resonance to circulate around the islands, before being captured again around the second island centred on $\omega = 270^\circ$, and finally alternates between these two evolutions.

Finally, we show that the trend observed in the right panel of Fig. 3.3 can be explained by the conservation of the Kozai constant (green curves). Indeed, for a given value of the Kozai constant, the ranges of possible eccentricity and inclination values for the planet are fixed by the relation $h = \sqrt{1 - e^2} \cos i$. Here the Kozai constant is evaluated at the dispersal of the disk and has been approximated by the quantity $\cos i_B$, since in this work the disk tends to circularize the planetary orbit and to keep it in the disk through eccentricity and inclination damping.

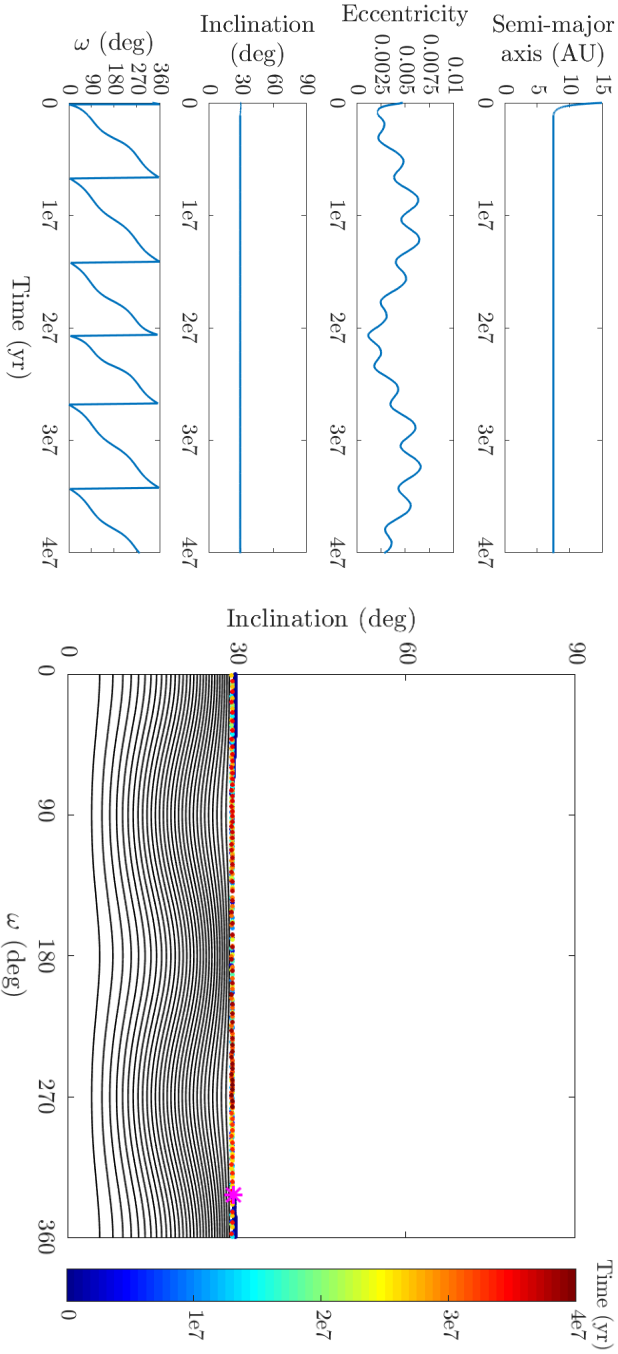


Figure 3.7 – Left panel: Typical evolution of a planet in the presence of a binary companion with an inclination lower than 40° . Right panel: Phase portrait of the evolution. The initial parameters are $m = 4.6 M_{\text{Jup}}$, $\omega = 152^\circ$, $e_B = 0.1$, and $i_B = 30^\circ$.

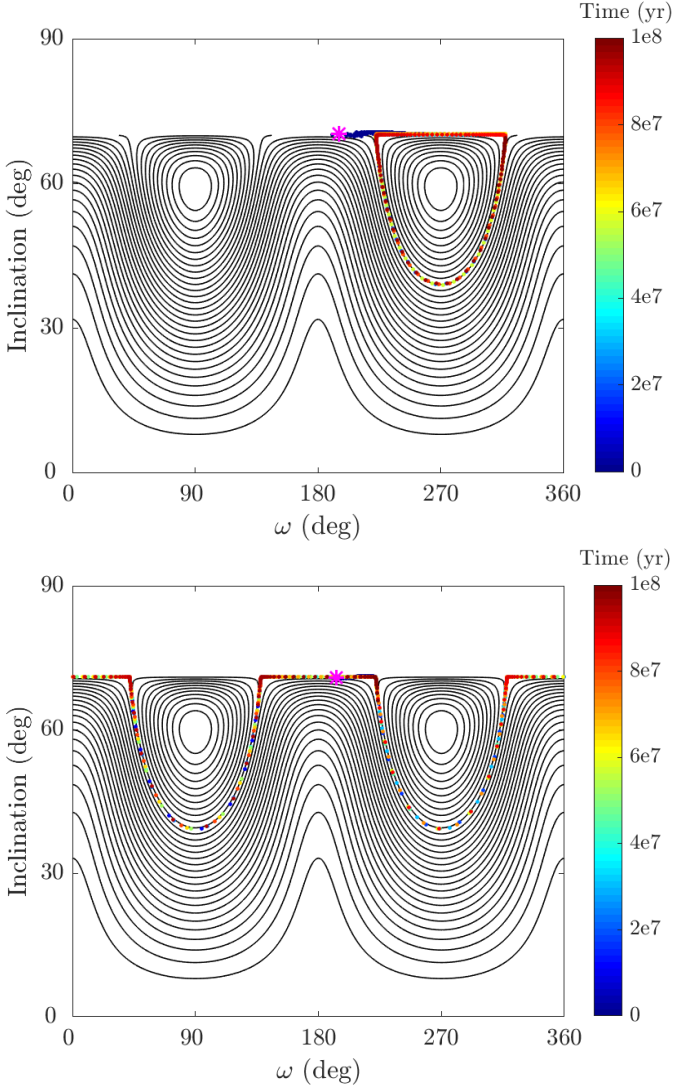


Figure 3.8 – Phase portraits of different planetary evolutions in the presence of a binary companion at $i_B = 70^\circ$. Top: Lidov-Kozai resonant evolution from Fig. 3.1. Bottom: non Lidov-Kozai resonant evolution from Fig. 3.2.

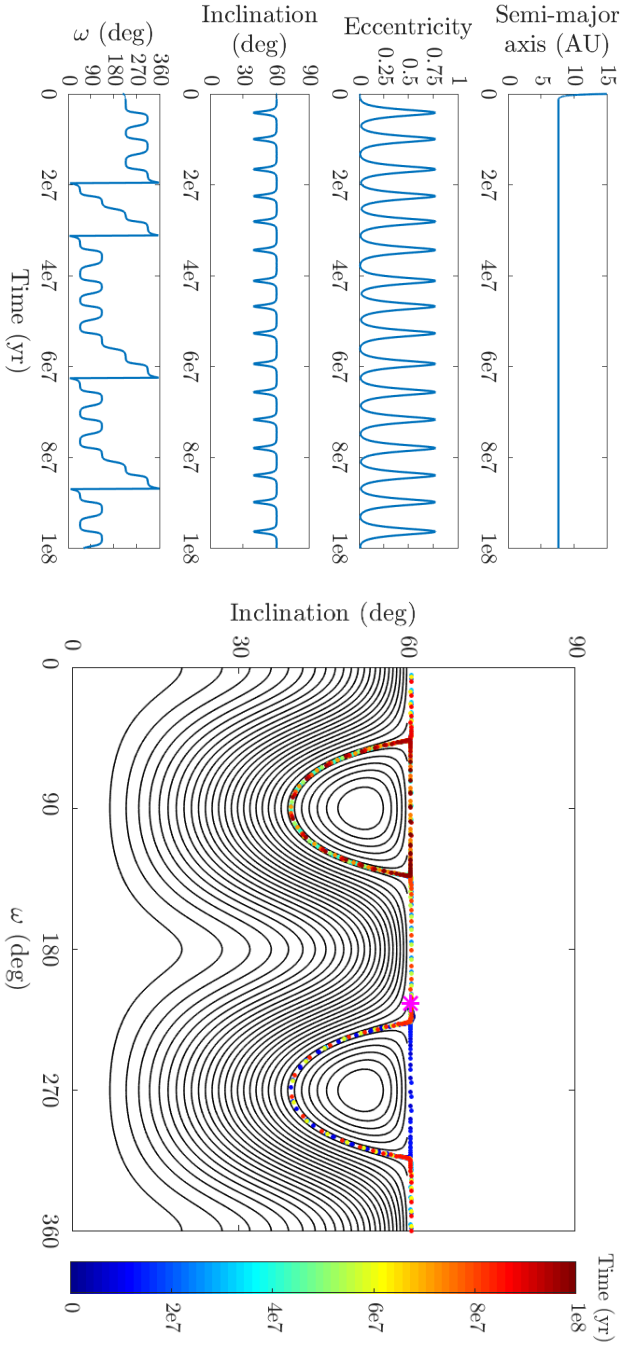


Figure 3.9 – Left panel: typical evolution of a planet alternating between resonance capture and circulation. Right panel: phase portrait of the evolution. The initial parameters are $m = 4.74 M_{\text{Jup}}$, $\omega = 35^\circ$, $e_B = 0.1$, and $i_B = 60^\circ$.

3.5 Discussion and conclusions

In this chapter, we studied the dynamical influence of a wide binary companion on the migration of a single giant planet in the protoplanetary disk. By varying the eccentricity and inclination of the binary companion as well as the physical and orbital parameters of the planet, we carried out 3200 numerical N -body simulations of the migrating planet and carefully analyzed the orbital configuration of the planets after 100 Myr.

As a consequence of the Lidov-Kozai mechanism, the influence of the wide binary companion is strong for highly inclined companions even during the disk phase. We showed that the orbital parameters of the planets at the end of the simulations gather around two arc-shaped curves in the plane (ω, e) . We noticed that only about 36% of the planets with a highly inclined binary companion ($i_B \geq 40^\circ$) end up in a Lidov-Kozai resonant state (with the libration of the pericenter argument). Nevertheless, the non resonant evolutions are strongly influenced by the Lidov-Kozai resonance and present high eccentricity and inclination variations associated with a circulation around the Lidov-Kozai islands. Using an analytical quadrupolar Hamiltonian approach, we realized phase portraits in which the different dynamical evolutions can easily be observed.

It is important to note that in this chapter we neglected the influence of the companion star on the disk, in particular, the induced nodal precession of the disk. To study the robustness of our results, and in particular the impact that nodal precession could have, we ran several tests by considering different migration rates and eccentricity and inclination damping rates as well as a location of the planet initially outside the disk. The results of these tests are summarized in Fig. 3.10 which shows, for the different tests, the same analysis as in Fig. 3.5, namely, the planetary inclination as a function of the argument of the pericenter at the end of the simulation, in which the color code indicates the initial inclination of the binary companion i_B . In the top panels, the planets are initially inside the disk plane ($i = 0^\circ$), while the planets have an initial inclination of $i = 20^\circ$ with respect to the disk plane in the bottom panels. Three modifications for the planetary migration are considered. In the left panels, the migration rates and eccentricity and inclination damping rates are unchanged. In the middle panels, the Type-II migration rate is scaled by the factor $\cos(i)$. In the right panels, no eccentricity and inclination damping are included. Thus, in total, six tests were realized, each one consisting in 3200 simulations, as previously detailed. As observed in Fig. 3.10, the modifications performed have no significant impact on the results and the arc-shaped curves are present in each test.

These extra simulations make us confident in the robustness of the results presented in this chapter. We obtained similar outcomes when changing the

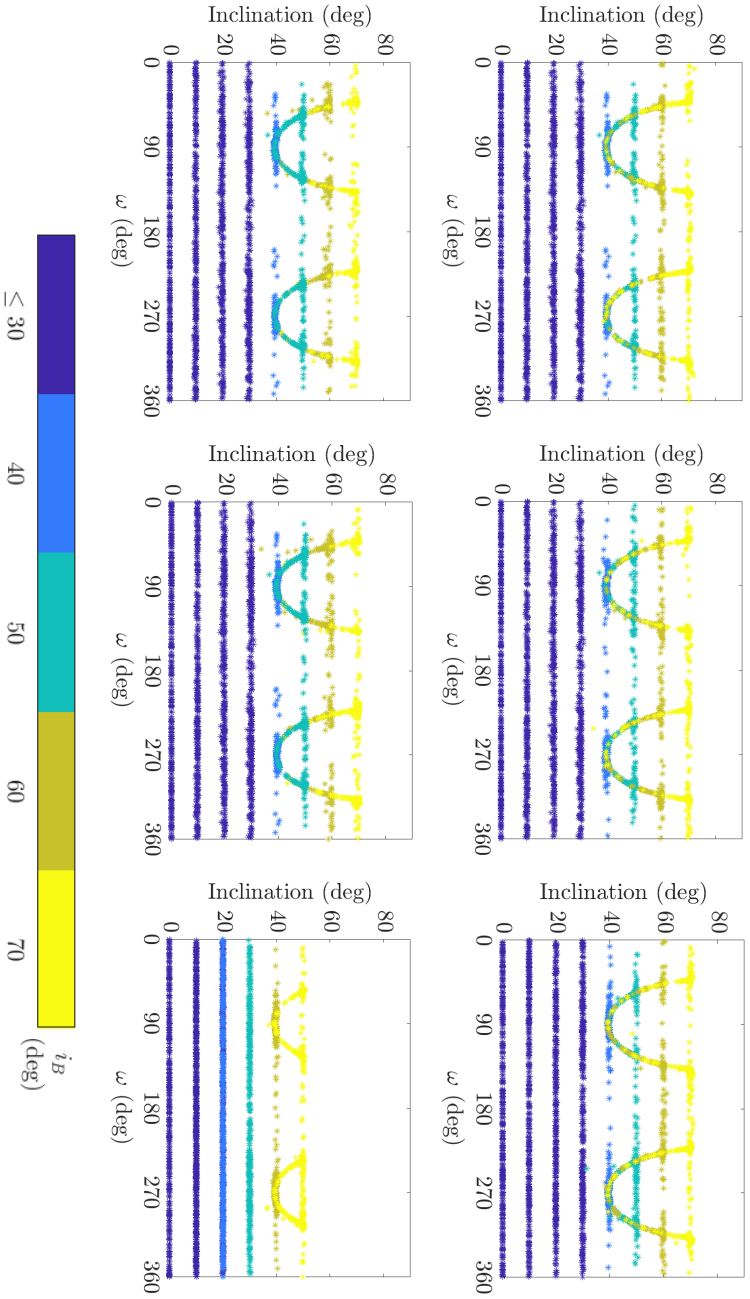


Figure 3.10 – Same as Fig. 3.5 for different migration and damping rates. Rates are shown unchanged in the left panels, Type-II migration rate scaled by the factor $\cos(i)$ indicated in the middle panels, and no eccentricity and inclination damping considered in the right panels. Two initial inclination values of the planet with respect to the disk plane are also shown (i fixed to 0° in the top panels and 20° in the bottom panels).

planetary inclination and, therefore, the mutual inclination between the planet and the disk. Therefore, we believe that the addition of the nodal precession of the disk caused by the binary star, inducing a change in the mutual inclination, does not significantly modify the long-term evolution of the planets.

In this work, we did not include additional effects due to the disk and the binary that are likely to have a significant impact on the evolution of the planet. Aside from the nodal precession of the disk caused by the binary star mentioned hereabove, we did not consider the apsidal and nodal precessions caused by the gravitational potential of the disk, which could dominate over the precession induced by the binary star (e.g., Zanazzi and Lai (2018b)). Also, the general relativity and the stellar oblateness could compete or suppress the Lidov-Kozai effect. The study of the influence of the nodal precession of the disk induced by the binary companion as well as the one of the disk potential will be deeply investigated in the next chapter.

Chapter 4

Planetary migration in precessing disks for S-type binaries

4.1 Introduction

In the previous chapter, we discussed the influence of a wide binary companion on the evolution of a giant planet migrating in the disk. This preliminary work neglected two potentially significant effects related to the disk, that is the disk gravitational potential acting on the planet and the nodal precession induced by the binary companion on the disk. The purpose of the present chapter is to study the influence of these effects on the previous results, in particular on the capture of the systems in the Lidov-Kozai resonance.

The gravitational potential exerted by a disk on an inclined planet was previously studied for a flat disk by Terquem and Ajmia (2010). They reported Lidov-Kozai cycles (associated with high values of the eccentricity) for a planet whose inclination is smaller than the critical angle value identified for an outer perturber in Lidov (1962) and Kozai (1962). The effects of disk warping on the planetary inclination was considered in Terquem (2013), where it was shown that the gravitational potential in 3D wrapped disks generally leads to the precession of the planet and could in some cases increase the planetary eccentricity. Teyssandier et al. (2013) considered frictional forces from 3D disk leading to eccentricity and inclination damping in addition to disk gravitational potential for inclined planets. They observed Lidov-Kozai cycles exerted by the disk on the planet for inclination value as small as 20° .

The precession of the disk caused by a binary companion was studied in Batygin et al. (2011), using both a Gauss's averaging method and an alterna-

tive method based on the Laplace-Lagrange secular theory, following the idea from Levison and Morbidelli (2007), and consisting in dividing the disk in several annuli. Further studies were carried out combining various effects, such as accretion, magnetic star-disk interaction, and solar winds, to explain the misalignment between the stellar spin axis and the disk angular momentum (see, e.g., Batygin and Adams, 2013; Lai, 2014; Spalding and Batygin, 2014). The nodal precession was also studied including disk warping in Zanazzi and Lai (2018a) and a migrating planet in Zanazzi and Lai (2018b).

When the disk mass decreases exponentially with time, as it is the case here, the analytical solution of Murray and Dermott (1999) and Batygin et al. (2011) for the disk nodal precession is not convenient (see Section 4.2.2.1) and we have developed here new approximate formulas for the evolution of the disk inclination and longitude of the ascending node suitable for a rigidly precessing disk perturbed by a wide binary companion.

The chapter is organized as follows. In Section 4.2, we describe the N -body code used for the simulations and derive formulas for the disk gravitational potential acting on the planet and the nodal precession induced by the binary companion on the disk. Section 4.3 presents the results of the simulations by emphasizing the influence of the two newly added effects on the evolution of the planet during the disk phase. Finally, our results are summarized in Section 4.4.

4.2 Additional effects

In this section, we focus on two physical effects that were neglected in the previous chapter, namely the disk gravitational potential acting on the giant planet (Section 4.2.1) and the nodal precession induced by the binary companion on the disk (Section 4.2.2) and show how they were implemented in our N -body code.

4.2.1 Disk gravitational potential

We first start by considering the gravitational potential that a disk exerts on a planet. We assume that the disk is flat and axisymmetric. The potential it exerts on a planet can be written in spherical coordinates as (see, e.g., Terquem and Ajmia, 2010)

$$\Phi(r, \varphi, \theta) = -G \int_{R_{\text{in}}}^{R_{\text{out}}} \Sigma(\tilde{r}) \tilde{r} \int_0^{2\pi} \frac{d\tilde{\varphi} d\tilde{r}}{\sqrt{r^2 + \tilde{r}^2 - 2r\tilde{r} \cos(\tilde{\varphi}) \sin(\theta)}}, \quad (4.1)$$

where (r, φ, θ) correspond to the spherical coordinates of the planet, Σ is the disk surface density, R_{in} and R_{out} are the inner and outer edges of the disk,

and G is the gravitational constant. Following Huré and Hersant (2011), the potential can be expressed as

$$\Phi(r, \varphi, \theta) = -2G \int_{R_{\text{in}}}^{R_{\text{out}}} \Sigma(\tilde{r}) \sqrt{\frac{\tilde{r}}{r \sin(\theta)}} k K(k) d\tilde{r}, \quad (4.2)$$

where $K(k)$ is the complete elliptic integral of first kind:

$$K(k) = \int_0^{\pi/2} \frac{d\tilde{\varphi}}{\sqrt{1 - k^2 \sin^2(\tilde{\varphi})}} \quad (4.3)$$

with k between 0 and 1 and equal, in our case, to

$$k = 2 \sqrt{\frac{r \tilde{r} \sin(\theta)}{r^2 + \tilde{r}^2 + 2r\tilde{r} \sin(\theta)}}. \quad (4.4)$$

To implement the potential in the code and preserve the symmetry of the integration scheme, we converted it to an acceleration in Cartesian heliocentric coordinates, which leads to the following expression

$$\begin{aligned} \frac{d^2 x}{dt^2} &= -\sin(\theta) \cos(\varphi) \frac{\partial \Phi}{\partial r} - \cos(\theta) \cos(\varphi) \frac{1}{r} \frac{\partial \Phi}{\partial \theta} \\ \frac{d^2 y}{dt^2} &= -\sin(\theta) \sin(\varphi) \frac{\partial \Phi}{\partial r} - \cos(\theta) \sin(\varphi) \frac{1}{r} \frac{\partial \Phi}{\partial \theta} \\ \frac{d^2 z}{dt^2} &= -\cos(\theta) \frac{\partial \Phi}{\partial r} + \sin(\theta) \frac{1}{r} \frac{\partial \Phi}{\partial \theta}, \end{aligned} \quad (4.5)$$

where

$$\begin{aligned} \frac{\partial \Phi}{\partial r} &= \frac{G}{r} \int_{R_{\text{in}}}^{R_{\text{out}}} \Sigma(\tilde{r}) \sqrt{\frac{\tilde{r}}{r \sin(\theta)}} k \left[K(k) - \frac{\tilde{r}^2 - r^2}{R^2} E(k) \right] d\tilde{r} \\ \frac{\partial \Phi}{\partial \theta} &= G \int_{R_{\text{in}}}^{R_{\text{out}}} \Sigma(\tilde{r}) \cot(\theta) \sqrt{\frac{\tilde{r}}{r \sin(\theta)}} k \left[K(k) - \frac{\tilde{r}^2 + r^2}{R^2} E(k) \right] d\tilde{r} \end{aligned} \quad (4.6)$$

with $R^2 = r^2 + \tilde{r}^2 - 2r\tilde{r} \sin(\theta)$ and $E(k)$ the complete elliptic integral of the second kind:

$$E(k) = \int_0^{\pi/2} \sqrt{1 - k^2 \sin^2(\tilde{\varphi})} d\tilde{\varphi}. \quad (4.7)$$

In order to evaluate the complete elliptic integrals, we used the approximation given by Abramowitz and Stegun (1972). The other integrals are calculated using the Romberg's method presented in Press et al. (1992). A divergence can arise in Eq. (4.6) when $R = 0$, that is, when the planet is exactly in the plane of the disk. In reality, massive planets tend to open a gap in disks, and the

gravitational interaction at this location is reduced (even when the planet is on an inclined orbit with respect to the disk midplane, see, e.g., Bitsch et al., 2013). In order to prevent R^2 from becoming 0, we simply replaced it by $R^2 + 10^{-6}$. Note that we also tried splitting the disk into two parts, one extending from R_{in} to $r - \Delta_{\text{gap}}/2$ and one from $r + \Delta_{\text{gap}}/2$ to R_{out} (where Δ_{gap} represents the gap width). We also tested the effect of removing the component of the potential within the Hill sphere of the planet. Both prescriptions did not significantly alter our results and we kept the simplest prescription mentioned above.

In this section we have evaluated the gravitational force exerted by the disk on the planet. On the other hand, the planet is also exerting a force on the disk. In particular, we are interested in this chapter in planets whose orbits can potentially be strongly inclined with respect to the disk midplane. Such planets could in principle create a warp in the disk. A linear calculation by Teyssandier et al. (2013) showed that the back-reaction of the planet on the disk exerts only a small torque and can be neglected.

4.2.2 Disk nodal precession caused by a binary companion

The second effect studied in this chapter is the disk response to the perturbation from a binary star companion. We describe how the numerical approximation is constructed in Section 4.2.2.1, while an analytical validation is performed in Section 4.2.2.2. Note that the approximation found here is only appropriate for rigidly precessing disks perturbed by a wide binary companion.

4.2.2.1 Construction of a numerical approximation

Our purpose is to determine formulas for the evolution of the inclination and longitude of the ascending node of the disk. The formulas deduced here are consistent only if the disk maintains an uniform inclination. This condition can be fulfilled when the disk self-gravity is considered (see Batygin et al., 2011, and our Fig. 4.1). The formulas are expressed with respect to the initial plane of the disk.

We followed the method of Batygin et al. (2011) based on Levison and Morbidelli (2007). This method consists in splitting the disk in several massive self-gravitating rings adjacent to one another, and modelling their interaction using the classical Laplace-Lagrange secular theory. This assumes that the disk is dominated by its self-gravity, as opposed to internal pressure forces (in that case, see, e.g., Larwood et al., 1996; Zanazzi and Lai, 2018a). Note that we suppose that the disk (and thus each individual ring) remains circular and therefore rings do not overlap with each others, preventing orbital crossing (see

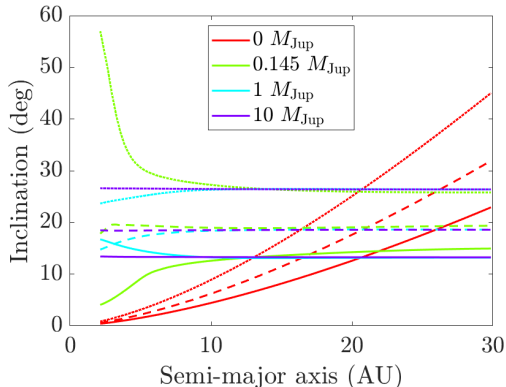


Figure 4.1 – Time evolution of the inclination of the disk as a function of the semi-major axis, for different disk masses (in the initial disk plane reference frame). The color code refers to the different masses and the line type to different times. The solid line stands for $t=0.5$ Myr, the dashed line for $t=0.75$ Myr and the dotted line for $t=1$ Myr. The inclination of the binary i_B is fixed to 60° .

Batygin et al., 2011).

The Hamiltonian of a given ring j is expressed by (see Murray and Dermott, 1999):

$$\mathcal{H}_j = \frac{1}{2} B_{jj} i_j^2 + \sum_{k=1, k \neq j}^{N+1} B_{jk} i_j i_k \cos(\Omega_j - \Omega_k) \quad (4.8)$$

with k being the indice of the different rings (note that we consider the binary companion as the $N+1$ -th ring), i_k the inclination and Ω_k the longitude of the node of the k -th ring. The coefficients are given by

$$B_{jj} = -\frac{n_j}{4} \sum_{k=1, k \neq j}^{N+1} \frac{m_k}{m_A + m_j} \alpha_{jk} \bar{\alpha}_{jk} b_{3/2}^{(1)}(\alpha_{jk}) \quad (4.9)$$

$$B_{jk} = \frac{n_j}{4} \frac{m_k}{m_A + m_j} \alpha_{jk} \bar{\alpha}_{jk} b_{3/2}^{(1)}(\alpha_{jk}) \quad (4.10)$$

with n_j the mean motion of j -th ring, m_j the mass of the j -th ring, m_A the mass of the central star, and $b_{3/2}^{(1)}$ the Laplace coefficient of the first kind. Note that $\bar{\alpha}_{jk}$ is equal to α_{jk} if the perturbation is external and to 1 otherwise. In our model, the thickness of the disk is not considered. More information about the modifications needed to take it into account can be found in Hahn (2003).

To simplify the resolution, Murray and Dermott (1999) proposed the fol-

lowing change of coordinates

$$\begin{aligned} q_j &= i_j \cos(\Omega_j) \\ p_j &= i_j \sin(\Omega_j) \end{aligned} \quad (4.11)$$

and the Hamiltonian can then be rewritten

$$\mathcal{H}_j = \frac{1}{2} B_{jj} (p_j^2 + q_j^2) + \sum_{k=1, k \neq j}^{N+1} B_{jk} (p_j p_k + q_j q_k). \quad (4.12)$$

The evolution of the different rings is obtained by solving the Hamiltonian equations. For a disk with a constant mass, an analytical solution can be found in Murray and Dermott (1999) and Batygin et al. (2011). However, for a decreasing mass model of the disk, as it is the case here, the use of the analytical solution is inappropriate, since the matrix B evolves with time and should be evaluated at each step, which is very time-consuming. For this reason, we aimed to derive approximate formulas for the evolution of the disk inclination and longitude of the ascending node when perturbed by a binary star.

To do so, we ran several simulations at constant disk mass. Our fiducial case used as a point of comparison is a system with a binary star consisting of two Sun-like stars with a separation of 1000 AU and an inclination with respect to the initial plane of the disk $i_B (= i_{N+1})$ of 60° , a disk with a constant mass of $10 M_{\text{Jup}}$, an inner edge at 2 AU, an outer edge at 30 AU and a disk surface density proportional to $r^{-0.5}$. Firstly, we tested the influence of the disk mass. Ten different masses for the disk were considered, namely 0, 0.145, 0.3, 0.5, 0.7, 1, 5, 8, 10, 20 M_{Jup} ⁽¹⁾. Fig. 4.1 displays the state of the disk at three different times (0.5, 0.75, and 1 Myr) for four different disk masses. We used a division of the disk in 100 annuli. We also ran simulations with different numbers of annuli between 20 and 1000 and obtained the same results. This confirms that the number of annuli seems not to significantly impact the results, as indicated in Batygin et al. (2011). When the disk is massive, there is no visible influence of the disk mass on the evolution of the inclination and the longitude of the ascending node and we conclude that for our chosen range of parameters, self-gravity efficiently maintains rigid precession throughout the disk. As seen in Batygin et al. (2011) and on Fig. 4.1, when the disk has no mass, its rigidity is not preserved since there is no self-gravity to allow communication between the different rings of the disk. Note that when the disk mass is small, the disk has some non-uniform motion close to the inner edge. Hydrodynamical effects (radial pressure force and viscous diffusion) that were not considered here can help the disk to maintain the uniform motion as

(1). In our simulations, 0.145 M_{Jup} is the disk mass at which the disk is considered to be fully dissipated.

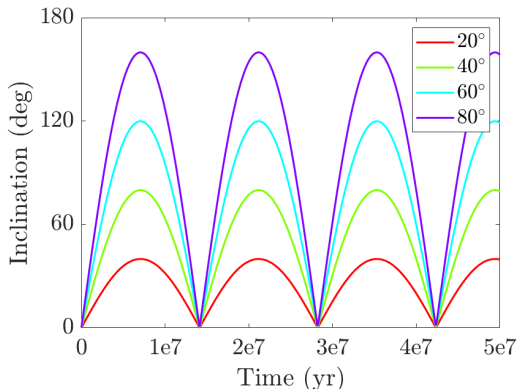


Figure 4.2 – Inclination of the mid-point ring of the disk as a function of time for various inclinations of the binary companion i_B . All the inclinations are expressed with respect to the initial plane of the disk.

discussed for instance in Papaloizou and Terquem (1995) and Larwood et al. (1996). From now, we will therefore consider the disk as having an uniform motion and display all results for the ring that is at a radius half-way between the inner and outer edges of the disk.

Secondly, we tested the influence of the inclination of the binary companion i_B by considering four different values: 20, 40, 60, and 80°. We used a constant disk mass model and carried on the evolution up to 5×10^7 yr. We show in Fig. 4.2 the time evolution of the inclination of the mid-point ring of the disk. Since the disk precesses around the total angular momentum of the system (which is very close to the binary angular momentum vector), the disk inclination varies between 0 and twice the initial inclination of the binary with respect to the initial disk plane. This explains why the inclination in Fig. 4.2 follows the absolute value of a sinus with an amplitude equal to twice the inclination of the binary companion (see Section 4.2.2.3 for details). Our interpolated formula for the inclination of the disk with respect to the initial plane of the disk i_d will therefore have the form

$$i_d(t) = 2i_B |\sin(2\pi f_d t)|, \quad (4.13)$$

with f_d the frequency of the sinusoidal function.

Thirdly, we run additional simulations with the longitude of the ascending node of the binary companion Ω_B set to 20, 40, 60, and 80°. We observe in

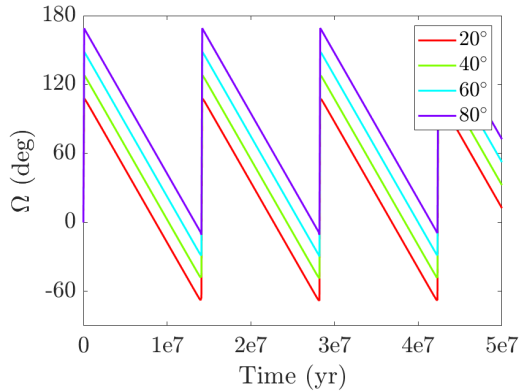


Figure 4.3 – Longitude of the ascending node of the mid-point ring of the disk as a function of time for various longitudes of the ascending node of the binary companion.

Fig. 4.3 that the maximum value of Ω_d is $\Omega_B + \frac{\pi}{2}$ in radians⁽²⁾.

We also notice in Fig. 4.3 the linearly decreasing evolution of the longitude of the ascending node of the disk with a period equal to the one of the inclination of the disk. Our formula for the longitude of the ascending node of the disk in the initial disk plane reference frame can therefore be written in the following way:

$$\Omega_d(t) = \frac{\pi}{2} + \Omega_B - (2\pi f_d t \bmod \pi). \quad (4.14)$$

The modulo represents the variation of 180° for the longitude of the ascending node observed in Fig. 4.3. This restriction comes from the choice of the reference frame and is further detailed in Section 4.2.2.3. A more natural choice of reference frame would be the plane of the binary companion, which almost coincides with the invariant Laplace plane. However, the damping formulas for the eccentricities and inclinations of the planets migrating in the disk from

(2). Note that this value can also be deduced from the expression of the mutual inclination i_{mut} between the disk and the binary companion, rewritten as

$$\Omega_d(t) = \arccos\left(\frac{\cos(i_{\text{mut}}) - \cos(i_B)\cos(i_d(t))}{\sin(i_d(t))\sin(i_B)}\right) + \Omega_B$$

and evaluated at $t = 0$. Since, in $t=0$, we have $i_d = 0$, $i_B = i_{\text{mut}}$ and

$$\lim_{t \rightarrow 0} \frac{1 - \cos(i_d(t))}{\sin(i_d(t))} = 0,$$

it can easily be shown that

$$\lim_{t \rightarrow 0} \Omega_d(t) = \frac{\pi}{2} + \Omega_B.$$

Table 4.1 – Parameters set for the determination of f_d .

Parameters	values
a_B (AU)	500, 1000, 2000
R_{in} (AU)	0.1, 0.5, 2
R_{out} (AU)	20, 30, 40
m_B (M_{\odot})	0.5, 1, 2

Bitsch et al. (2013) implemented in our N -body code have been designed for the initial disk plane reference frame, which explains this choice.

We now need to determine the expression of the precession frequency f_d . A parametric study was carried out to investigate the influence on the frequency f_d of different parameters: the mass of the binary m_B and the semi-major axes of the binary a_B , the inner edge R_{in} , and the outer edge R_{out} . The values considered in the study are displayed in Table 4.1. Note that we did not notice any impact of the inner edge of the disk on the frequency f_d . From this parametric study, we found that the best approximation for f_d is given by

$$f_d = 0.2145 \left(\frac{R_{\text{out}}}{1 \text{ AU}} \right)^{3/2} \left(\frac{a_B}{1 \text{ AU}} \right)^{-3} \left(\frac{m_B}{1 M_{\odot}} \right). \quad (4.15)$$

As we will see in Section 4.2.2.2, this scaling with the different relevant quantities is a consequence of the secular interactions and can also be derived analytically.

To test the precision of our approximate formulas, we show a comparison of the evolution of the disk when using the Hamiltonian formulation (4.12) and our approximation (4.13)-(4.14), in the case of an exponentially decreasing disk mass. The following system parameters are considered for the simulation: $m_A = m_B = 1 M_{\odot}$, $R_{\text{in}} = 2 \text{ AU}$, $R_{\text{out}} = 30 \text{ AU}$, $a_B = 1000 \text{ AU}$, $i_B = 60^\circ$, $\Omega_B = 50^\circ$, an initial disk mass of $8 M_{\text{Jup}}$, a disk surface profile density proportional to $r^{-0.5}$, and $T_0 = 2.8 \times 10^5 \text{ yr}$. The evolution of the inclination and the longitude of the ascending node of the disk is displayed in Fig. 4.4 (top panels), with stars representing the formulation (4.12), while solid lines show our approximation (4.13)-(4.14). The two models are in good agreement, as shown by the relative error displayed in the bottom panel (relative error below 1% during the whole disk lifetime).

To summarize, in this section we numerically found formulas for the evolution of the inclination (Eq. (4.13)) and longitude of the ascending node (Eq. (4.14)) of a rigidly precessing disk perturbed by a distant binary companion (expressed with respect to the initial plane of the disk).

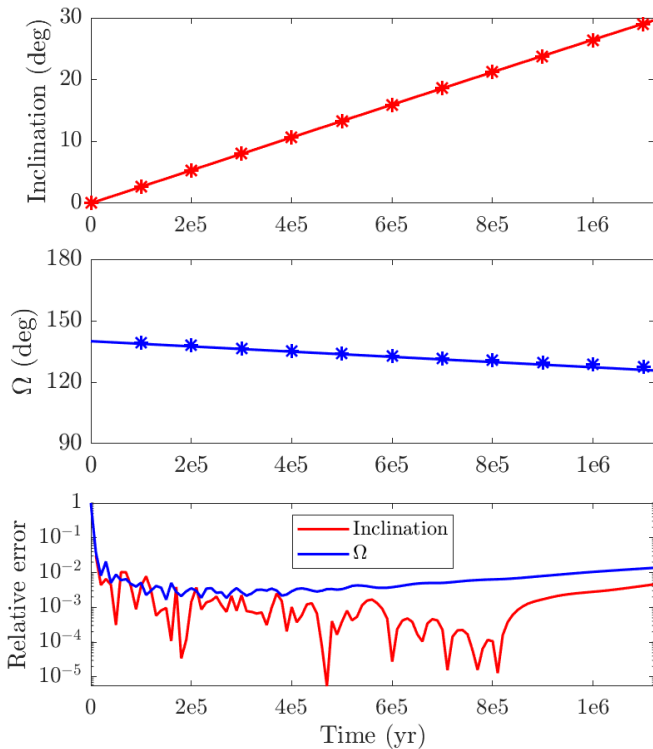


Figure 4.4 – Comparison between the interpolated formulas (4.13)-(4.14) (solid line) and the numerical simulation of Hamiltonian (4.12) (stars) for the evolution of a disk whose mass decreases exponentially and which is perturbed by a wide binary companion. The top panel shows the inclination of the disk while the middle panel shows the longitude of the ascending node. The relative errors between the two formulations are displayed in the bottom panel.

4.2.2.2 Analytical validation of the precession frequency

The frequency obtained in Eq. (4.15) can also be derived analytically, and thus provides a check of its validity. To do so, we assume that the disk can be represented by a continuum of concentric circular annuli. It is useful to introduce the complex inclination W , such as $W(r, t) = i(r, t) \exp(i\Omega)$. The disk is warped if i varies with radius, and twisted if Ω varies with radius. W relates to the variables p and q of Eq. (4.11) as $\text{Re}(W) = q$ and $\text{Im}(W) = p$. Similarly, we represent the binary star by its complex inclination $W_B = i_B \exp(i\Omega_B)$. The disk extends from R_{in} to R_{out} . We assume that the disk surface density goes

as

$$\Sigma(r) = \Sigma_0 \left(\frac{r}{R_{\text{in}}} \right)^{-p} \quad (4.16)$$

and follows a Keplerian rotation around the central star of mass m_A , with a Keplerian frequency n .

A massive companion (in our case a binary star) exerts an external torque onto the disk. If we consider the disk to be a continuum of annuli with radius r , the secular interaction between each of these annuli and the binary star companion is equivalent to that described by the Laplace-Lagrange theory as seen in Section 4.2.2.1. The equation for an annulus of the disk is (Lubow and Ogilvie, 2001):

$$\Sigma r^2 n \frac{\partial W}{\partial t} = i G m_B \Sigma \mathcal{K} (W_B - W). \quad (4.17)$$

Here \mathcal{K} is a symmetric function related to the well-known Laplace coefficients, defined by

$$\mathcal{K}(r, r') = \frac{r r'}{4\pi} \int_0^{2\pi} \frac{\cos \varphi \, d\varphi}{(r^2 + r'^2 - 2 r r' \cos \varphi)^{3/2}}. \quad (4.18)$$

One can show that

$$\mathcal{K}(r, a_B) = \frac{1}{4a_B} \left(\frac{r}{a_B} \right) b_{3/2}^{(1)}. \quad (4.19)$$

At first order in $r < a_B$, one has $b_{3/2}^{(1)} = 3r/a_B$.

In order to get the precession of the whole disk, we multiply Eq. (4.17) by $2\pi r$ and integrate over the radial extent of the disk. We assume that internal physical processes, such as pressure and self-gravity, maintain the disk rigid nodal precession, against the differential precession induced by the binary. In other words, W does not depend on r . We have seen in the previous section how self-gravity can provide a mean to maintain such coherence (see also Batygin et al., 2011), and various authors (see, e.g., Larwood et al., 1996; Zanazzi and Lai, 2018a) have explored how pressure-driven bending waves can have the same effect. We also assume that the disk does not exert a back reaction onto the binary, so that $W_B = 0$ (since the reference plane here is the orbital plane of the binary). For $r < a_B$, we find that

$$\dot{W} = -i \frac{3}{4} \lambda \left(\frac{R_{\text{out}}}{a_B} \right)^3 \frac{m_B}{m_A} n_{\text{out}} W, \quad (4.20)$$

where n_{out} is the Keplerian frequency at the outer edge of the disk, and we have introduced

$$\lambda = \frac{\frac{5}{2} - p}{4 - p} \frac{1 - \eta^{4-p}}{1 - \eta^{5/2-p}}, \quad (4.21)$$

with $\eta = R_{\text{in}}/R_{\text{out}}$. For clarity, let us define the nodal precession frequency ω_{db} as

$$\omega_{\text{db}} = \frac{3}{4} \lambda \frac{m_B}{m_A} \left(\frac{R_{\text{out}}}{a_B} \right)^3 n_{\text{out}}. \quad (4.22)$$

This expression is the same as the one obtained by Zanazzi and Lai (2018b). Then the first-order linear ODE rewrites

$$\dot{W} = -i\omega_{\text{db}}W. \quad (4.23)$$

If the inclination of the disk at $t = 0$ is denoted by i_0 , its longitude of the ascending node by Ω_0 , and therefore the initial complex inclination of the disk by $W_0 = i_0 e^{i\Omega_0}$, the solution of Eq. (4.23) is

$$W(t) = i_0 e^{i(\Omega_0 - \omega_{\text{db}}t)}. \quad (4.24)$$

This implies that the inclination of the disk remains constant (since $|W| = i_0$) and the longitude of the ascending node of the disk precesses as

$$\Omega(t) = \Omega_0 - \omega_{\text{db}}t. \quad (4.25)$$

For the parameters considered in the previous section, namely $m_A = 1 M_{\odot}$, $p = 0.5$, $R_{\text{in}} = 2$ AU, and $R_{\text{out}} = 30$ AU, we find that $\omega_{\text{db}} = 2.7046$, which we can compare to the value of the numerical coefficient of Eq. (4.15): $2 \times 2\pi \times 0.2145 = 2.695$. Note that the frequency has to be doubled since the sinus is in absolute value and we also multiply by a factor 2π to make the link between the ordinary frequency in Eq. (4.15) with the angular frequency from Eq. (4.22). The agreement between the two values is very good. Note also that the influence of R_{in} is somewhat limited in Eq. (4.22), which explains that we did not notice a significant influence of R_{in} on the disk evolution in the numerical simulations of Section 4.2.2.1.

4.2.2.3 Details about the change of coordinates between the orbital plane of the binary and the initial plane of the disk

In Section 4.2.2.2, we analytically determined the evolution of the disk inclination and longitude of the ascending node with respect to the orbital plane of the binary. Here, we aim to explain the particularities highlighted in the formulas (4.13) (i.e., the amplitude of the sinus function) and (4.14) (i.e., the modulo π) of Section 4.2.2.1 regarding the evolution of the disk with respect to the initial disk plane reference frame.

The direction of the angular momentum of the disk can be expressed in the binary companion orbital plane reference frame as (Murray and Dermott,

1999):

$$\begin{pmatrix} \sin i \sin \Omega(t) \\ \sin i \cos \Omega(t) \\ \cos i \end{pmatrix}, \quad (4.26)$$

with i the inclination of the disk and Ω the longitude of the ascending node of the disk. Remember that the inclination is constant in this reference frame. Since our purpose is to express the angles with respect to the initial plane of the disk, we first apply a rotation around the z -axis with an angle equivalent to the initial longitude of the ascending node Ω_0 and then a rotation around the x -axis with the inclination $i = i_0$. We find

$$\begin{pmatrix} \sin i_d(t) \sin \Omega_d(t) \\ -\sin i_d(t) \cos \Omega_d(t) \\ \cos i_d(t) \end{pmatrix} = \begin{pmatrix} 1 & 0 & 0 \\ 0 & \cos i & -\sin i \\ 0 & \sin i & \cos i \end{pmatrix} \begin{pmatrix} \cos \Omega_0 & \sin \Omega_0 & 0 \\ -\sin \Omega_0 & \cos \Omega_0 & 0 \\ 0 & 0 & 1 \end{pmatrix} \begin{pmatrix} \sin i \sin \Omega(t) \\ -\sin i \cos \Omega(t) \\ \cos i \end{pmatrix}, \quad (4.27)$$

with $i_d(t)$ and $\Omega_d(t)$ the inclination and longitude of the ascending node of the disk, respectively, with respect to the initial plane of the disk. Using Eq. (4.25) and some trigonometrical identities, we obtain

$$\begin{pmatrix} \sin i_d(t) \sin \Omega_d(t) \\ -\sin i_d(t) \cos \Omega_d(t) \\ \cos i_d(t) \end{pmatrix} = \begin{pmatrix} \sin i \sin(\omega_{db}t) \\ -\cos i \sin i [1 - \cos(\omega_{db}t)] \\ \frac{1}{2} [1 + \cos(2i) + (1 - \cos(2i)) \cos(\omega_{db}t)] \end{pmatrix} \quad (4.28)$$

The last component of the disk angular momentum vector ranges from $\cos(2i)$ to 1, which explains the amplitude for $i_d(t)$ of $2i_B$ found in Eq. (4.13). Considering that the inclination $i_d(t)$ varies between 0 and π and since the expression of the second component of the vector is constant in sign, the variation of $\Omega_d(t)$ takes place on an interval of length π instead of 2π .

For the sake of completeness, the evolution of the disk in the initial disk plane reference frame, similar to the one of Eqs. (4.13)-(4.14), is then given by

$$\begin{cases} i_d(t) = \arccos \left(\frac{1}{2} [1 + \cos(2i_B) + (1 - \cos(2i_B)) \cos(\omega_{db}t)] \right) \\ \Omega_d(t) = \arctan 2 (\sin(\omega_{db}t), \cos i_B [1 - \cos(\omega_{db}t)]) + \Omega_B. \end{cases} \quad (4.29)$$

4.3 Simulations

In this section, we study the influence of the two additional effects described in the previous section, namely the disk gravitational potential (hereafter, GP)

Table 4.2 – Initial parameters for the simulations. The orbital elements are expressed with respect to the initial plane of the disk.

	Central star	Planet	Binary companion
mass	$1 M_{\odot}$	$U[1;5] M_{\text{Jup}}$	$1 M_{\odot}$
a (AU)		20	1000
e		$U[0.001;0.01]$	$10^{-3}, 0.1, 0.3, 0.5$
i ($^{\circ}$)		$U[0.01;0.1]$	$10^{-3}, 10, 20, 30, 40,$ 50, 60, 70
Ω ($^{\circ}$)		10^{-3}	10^{-3}
ω ($^{\circ}$)		$U[0;360]$	10^{-3}
M ($^{\circ}$)		10^{-3}	10^{-3}

and the disk nodal precession caused by a binary companion (hereafter, NP), on the evolution of a migrating giant planet in a S-type binary system. This chapter pursues the study of the previous one, where such effects were not considered.

4.3.1 Parameter set-up

In this chapter, we carried out 3200 numerical simulations of the evolution of a single giant planet migrating in a S-type wide binary system. The study is carried out with the symplectic N -body code adapted for a migrating planet in binary star systems presented in Chapter 2 and already used in Chapter 3. As in the previous section, the wide binary companion is located at a distance of 1000 AU. Regarding the disk parameters, we fix the disk inner edge to 0.05 AU, the outer edge to 30 AU, and the surface profile density proportional to $r^{-0.5}$. The disk mass at $t = 0$ is fixed here to $8 M_{\text{Jup}}$ and $T_0 = 2.8 \times 10^5$ yr, which corresponds to a disk dispersal time of ~ 1 Myr (Mamajek, 2009). Table 4.2 summarizes the mass and orbital parameters considered for the two stars and the giant planet. For the binary companion, we used 8 different inclinations ranging from nearly 0° to 70° , as well as 4 different eccentricities ($10^{-3}, 0.1, 0.3,$ and 0.5). For each combination of eccentricity and inclination values of the binary companion, we randomly drew 100 different initial conditions for the planet by considering uniform distribution for the planetary mass ($m \sim U[1;5] M_{\text{Jup}}$), eccentricity ($e \sim U[0.001;0.01]$), inclination ($i \sim U[0.01^{\circ};0.1^{\circ}]$), and argument of the pericenter ($\omega \sim U[0^{\circ};360^{\circ}]$).

The 3200 simulations were run with and without the GP and NP effects, for comparison. The systems were followed for 5×10^8 yr, with a time step of 5×10^{-3} yr during the disk phase and 10^{-2} yr after the dissipation of the disk.

4.3.2 Typical example

We first present a typical example of the evolution of a migrating giant planet perturbed by a wide binary companion on an eccentric (0.3) and inclined (40°) orbit. Fig. 4.5 displays the time evolution of the orbital elements of the planet during the disk phase for four different models: when the GP and NP are both included (blue curves), when the GP only is included (red curves), when the NP only is included (black curves), and finally when the GP and NP are not considered (cyan curves).

While the planetary semi-major axis decreases due to the Type-II migration, the GP acting on the migrating planet tends to excite the planetary eccentricity and thus compete with the eccentricity damping associated with the Type-II migration. We can easily observe the gradual lowering of the damping effect associated to the decrease of the disk mass. Regarding the inclination of the planet, when both the GP and NP effects are present (blue curves), the planet closely follows the evolution of the disk, whose inclination and nodal precession computed from Eqs. (4.13)-(4.14) are indicated in Fig. 4.5 with magenta curves. The mutual inclination between the planet and the disk is also shown in the bottom panel and confirms that the planet stays in the disk during the whole disk phase when both effects are considered. When NP only is included (black curve), the disk and the planet are gravitationally decoupled and precess at different rates in the binary plane.

In Fig. 4.6, the same system evolution is shown in the invariant Laplace plane. In this reference plane, the Lidov-Kozai resonance can be easily identified from the libration of the planetary argument of the pericenter. We observe that, when the GP is not considered, the argument of the pericenter rapidly librates around 90° , which indicates a capture of the planet in a Lidov-Kozai resonant state with the binary companion. On the contrary, the GP prevents the planet to be locked into the Lidov-Kozai resonance during the disk phase. This example clearly shows that GP is the dominant effect acting on the dynamics of a migrating planet when compared to the nodal precession, as previously envisioned in the discussion of Roisin and Libert (2021).

4.3.3 Results

We now study the final parameters distribution of the 3200 simulations carried out in this chapter. In particular, to further study the GP and NP effects, we are interested in the planetary orbital values at the dispersal of the disk. In Fig. 4.7, we report the inclination of the planet at the dissipation of the disk with respect to the initial inclination of the binary companion, with circle symbol indicating inclinations in the initial disk plane reference frame. As previously, the blue color refers to simulations with GP and NP,

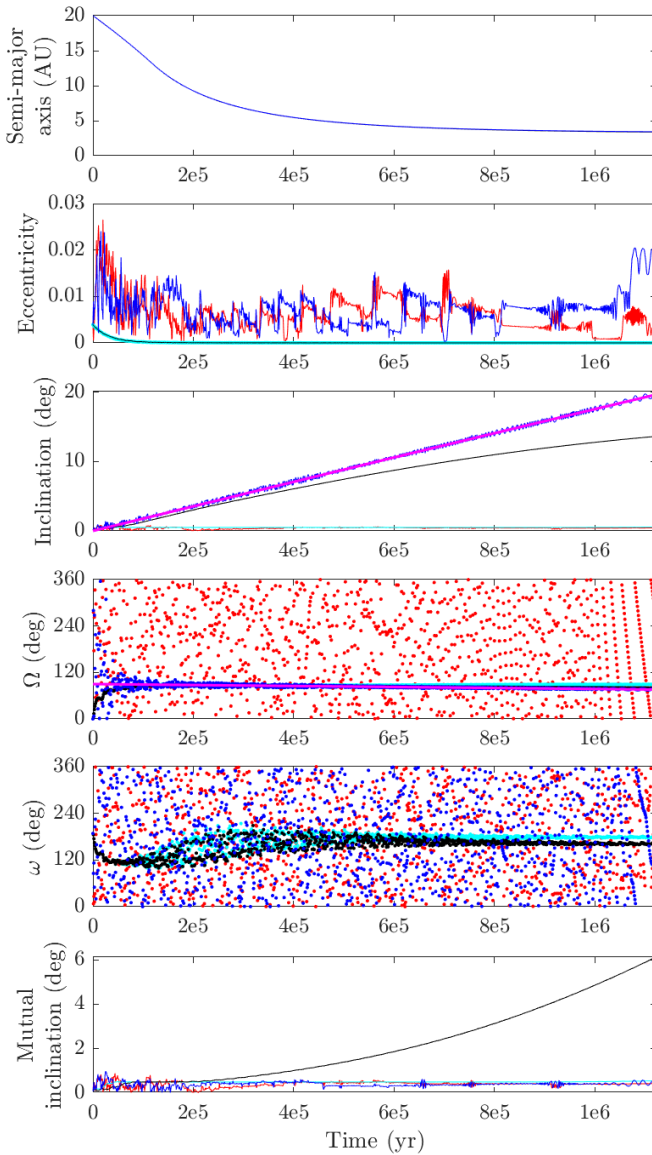


Figure 4.5 – Typical evolution of a migrating giant planet in the presence of a distant binary companion when GP and NP effects are considered (blue curve). All elements are measured with respect to the initial disk plane. The cyan curves present the system evolving without GP/NP, the red curves with GP only, and the black lines with NP only. The magenta lines represent the disk evolution predicted through the formulas (4.13)-(4.14). Initial parameters are $e_B = 0.3$, $i_B = 40^\circ$, $m = 1.53 M_{\text{Jup}}$, and $\omega = 188^\circ$.

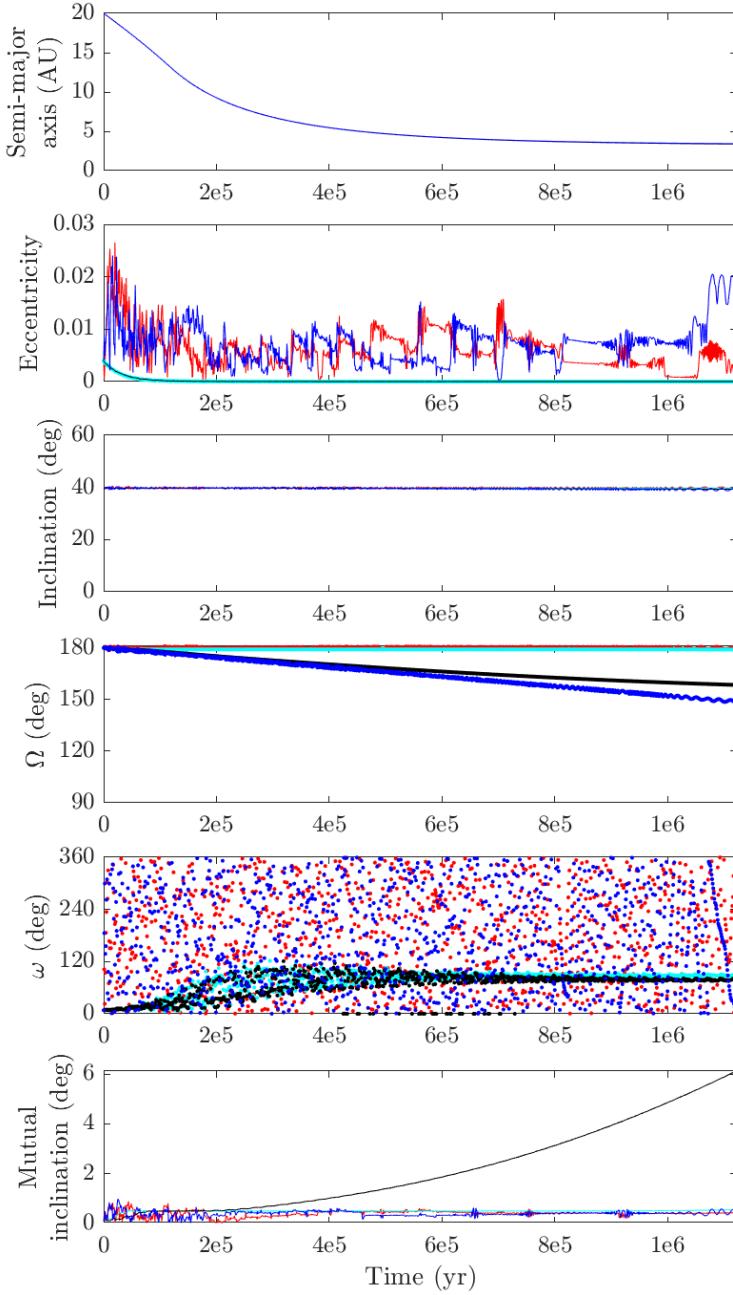


Figure 4.6 – Same as Fig. 4.5, but with respect to the invariant Laplace plane.

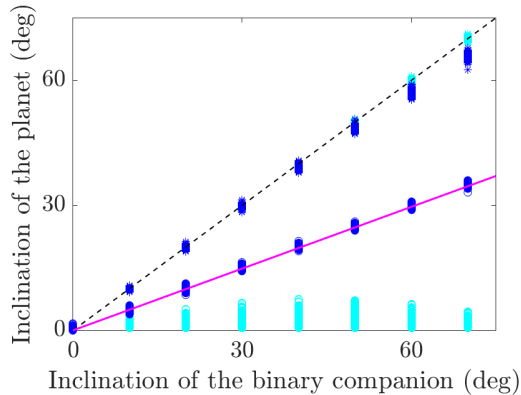


Figure 4.7 – Planetary inclination versus inclination of the binary companion, at the dispersal of the disk. The blue (cyan) color refers to simulations with (without) GP/NP. The circle symbol refers to inclinations in the initial disk plane, and the star symbol in the invariant Laplace plane.

the cyan color to simulations without the two effects, and the magenta line to the disk inclination expected at the dissipation of the disk according to Eq. (4.13). We observe that almost all the planets follow this line when the GP and NP are included, which means that for all the initial parameters of the planet and the binary companion considered, the planet always stays in the disk during the disk phase, as also observed for the typical evolution in the previous section. Using star symbol, we report the inclinations with respect to the invariant Laplace plane. The black dashed line indicates when the planetary and binary inclinations in the Laplace plane are equal, highlighting the systems for which the mutual inclination stays almost constant during the disk phase, since most of the total angular momentum of the system is due to the binary companion. For simulations including GP and NP, we observe a small deviation from the black dashed line for highly inclined binary companions. This is due to the limitation of the Laplace-Lagrange theory used in Section 4.2.2.1 for high inclinations (see the discussion in the supplementary material of Batygin (2012) for more details).

A particular attention was also given to the Lidov-Kozai resonance. In Chapter 3, it was shown that the capture of the migrating planet in a Lidov-Kozai resonant state is far of being automatic when the binary companion is highly inclined. We first studied the percentage of systems ending up in a Lidov-Kozai resonance state (at the end of the simulation, i.e. 5×10^8 yr), for the different inclinations of the binary companion. The results are gathered in Table 4.3. The higher the inclination of the binary companion, the higher the

Table 4.3 – Percentages of the systems ending up in a Lidov-Kozai resonant state, for the different inclinations of the binary companion i_B .

i_B ($^\circ$)	Without GP/NP (%)	With GP/NP (%)
≤ 30	0	0
40	4.5	2.75
50	41.5	28.75
60	22.25	37.5
70	17.5	30.25

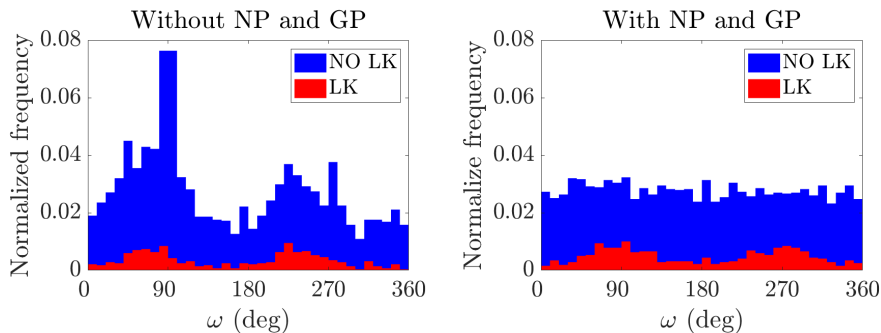


Figure 4.8 – Normalized distribution of the pericenter argument of the planet (in the invariant Laplace plane reference frame) at the dispersal of the disk, for the simulations without GP/NP (left panel) and with GP/NP (right panel).

probability of capture in a Lidov-Kozai resonant state. Note that a planet is considered here as locked in a Lidov-Kozai resonance if its argument of the pericenter librates, in the Laplace reference frame, around 90° or 270° for at least three secular periods.

To further analyse the impact of the disk phase on the capture into a Lidov-Kozai resonance, we also focused on the values of the planet argument of pericenter at the dispersal of the disk. In Fig. 4.8, we show the distribution of the pericenter argument of the planet (in the invariant Laplace plane) at the end of the disk phase, when considering the GP and NP effects (right panel) or not (left panel). The red color indicates that the planets are in a Lidov-Kozai resonant state at the end of the simulation. While accumulations of the pericenter argument around 90° and 270° during the disk phase are clearly visible without the GP and NP effects, these accumulations disappear when considering the two effects. As previously illustrated with the typical evolution shown in Fig. 4.5, it is the GP effect of the disk acting on the planet that suppresses the Lidov-Kozai oscillations induced by the binary companion. The same result

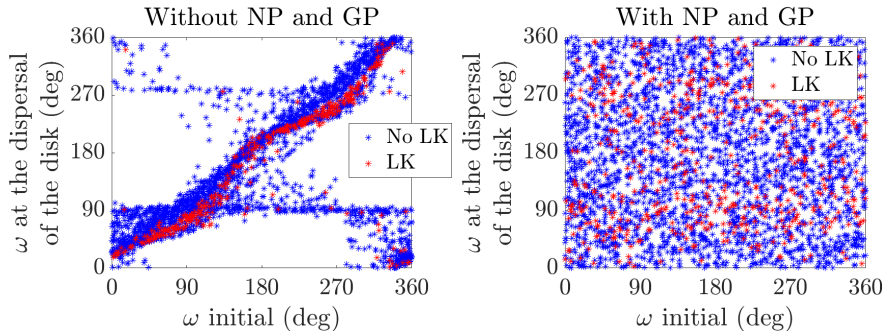


Figure 4.9 – Pericenter argument of the planet at the dispersal of the disk versus initial pericenter argument (in the invariant Laplace plane reference frame), for the simulations without GP/NP (left panel) and with GP/NP (right panel).

can be observed in Fig. 4.9 where the pericenter argument of the planet at the dispersal of the disk is represented as a function of the initial pericenter argument value (in the invariant Laplace plane). On the left panel, when the GP and NP are not included in the simulations, we observe the accumulation to values close to 90° and 270° , typical of the Lidov-Kozai resonance, during the disk phase. This particular shape completely disappears on the right panel where the GP and NP effects of the disk are present.

Once the disk has lost its whole mass, it becomes possible for the planet to fully undergo Lidov-Kozai oscillations driven by the binary, without those being quenched by the disk GP. In Fig. 4.10, we show the inclination of the planet with respect to the argument of its pericenter (in the invariant Laplace plane), at the end of the simulation (i.e., 5×10^8 yr). We see that although the GP and NP effects were considered during the disk phase, the arc-shape curves previously observed in Chapter 3 and associated to the libration islands around the Lidov-Kozai equilibria are still present. As also shown in Table 4.3, there are even slightly more planets evolving in the Lidov-Kozai resonance at the end of the simulations when the GP and NP effects are considered during the disk phase.

4.4 Conclusions

In this chapter, we aimed to study the evolution of a planet migrating in the disk in the presence of a wide binary companion. To do so, we derived new formulas of the evolution of a mass-decreasing disk under the influence of a wide binary companion in the initial disk plane reference frame. These formulas were obtained by splitting the disk in several massive rings adjacent to

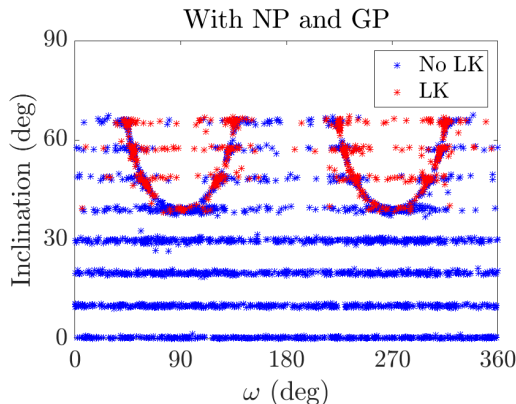


Figure 4.10 – Inclination of the planet as a function of the argument of the pericenter (in the invariant Laplace plane reference frame), at the end of the simulation (5×10^8 yr).

one another and evolving with the classical Laplace-Lagrange secular theory. We implemented this evolution in the N -body code presented in Chapter 3 consisting in an adaptation of the well-known symplectic integrator SyMBA to wide binary systems and including the Type-II migration and eccentricity and inclination damping due to the disk. In this chapter, we also added the influence of the gravitational potential of the disk. Using this new code, we were able to accurately modelize the disk nodal precession around the binary, as well as take into account the gravitational force that the disk exerts on the planet.

We observed that, while the nodal precession has a limited influence on the evolution of a giant planet migrating in a disk, the gravitational potential plays an important role in its evolution. In particular, it acts to keep the planet in the disk and suppress the effect of the Lidov-Kozai resonance induced by the binary companion during the disk phase. Regarding the establishment of the Lidov-Kozai resonance after the disk phase, one third of the planets with a highly inclined binary companion ended up locked in a Lidov-Kozai resonant state, that is roughly the same percentage as in Chapter 3, where the disk gravitational potential acting on the planet and the nodal precession induced by the binary companion on the disk were not considered.

Finally, it is interesting to stress that, even for slightly inclined binary companions, a misalignment between the disk and the spin axis of the primary star is observed, due to the nodal precession induced by the binary companion (see Fig. 4.2). Crida and Batygin (2014) highlighted that the observed distribution of the spin-orbit angles for the hot Jupiters could be explained by giant

planet migration in a disk possibly torqued by a binary companion. Lai (2014) also predicted that a primordial spin-orbit misalignment could be generated between a planet and its parent star in S-type binaries, although their model did not include a planet. Here we are able to confirm their prediction: since the gravitational potential and damping effect of the disk act to maintain the planet in the disk orbital plane during the disk-induced migration phase, a primordial spin-orbit misalignment could also be generated for circumprimary planets with an inclined binary companion. A comparison with observations would be interesting as a future work.

Part III

Two-planet systems

Chapter 5

Resonance captures in binary star systems

5.1 Introduction

In this chapter, we aim to study the influence of a binary companion on the resonance capture of two migrating giant planets in the Type-II regime. To do so, we use the symplectic integrator for S-type planets in binary stars presented in Chapter 2 and which includes the Type-II migration of giant planets during the protoplanetary disk phase with suitable eccentricity and inclination damping as well as the gravitational potential acting on the planets due to the disk and the nodal precession of the disk induced by the binary companion, as described in the previous chapter. This time we focus on two-planet systems and the parts of the code dealing with planetary close encounters (Section 2.1.5.1) and the gravitational interaction between the planets (first term of Eq. (2.41)) are now included.

We first run a set of 3200 simulations considering various initial positions for the two planets embedded in the protoplanetary disk as well as various eccentricities and inclinations for the binary companion. In a second phase, we study more deeply the Lidov-Kozai resonance effect by varying the distance of the binary companion, leading to 6400 new simulations. We pursue all the simulations well after the dispersal of the disk as in the previous chapters to also study the long-term dynamics of the system.

The chapter is organized as follows. Section 5.2 describes the set-up of the simulations, several typical planetary evolutions observed in this work, and the parameter distributions found at the end of the simulations. A parametric

Table 5.1 – Initial parameters for the simulations. The orbital elements are expressed with respect to the initial plane of the disk.

	Central star	Inner planet	Outer planet	Binary companion
mass	$1 M_{\odot}$	$U[1;5] M_{\text{Jup}}$	$U[1;5] M_{\text{Jup}}$	$1 M_{\odot}$
a (AU)		$U[5, 7]$	$U[12, 21]$	1000
e		$U[0.001;0.01]$	$U[0.001;0.01]$	$10^{-3}, 0.1, 0.3, 0.5$
i ($^{\circ}$)		$U[0.01;0.1]$	$U[0.01;0.1]$	$10^{-3}, 10, 20, 30, 40,$ 50, 60, 70
Ω ($^{\circ}$)		$U[0, 360]$	$U[0, 360]$	$U[0, 360]$
ω ($^{\circ}$)		$U[0, 360]$	$U[0, 360]$	$U[0, 360]$
M ($^{\circ}$)		$U[0, 360]$	$U[0, 360]$	$U[0, 360]$

study of the impact of the binary companion is achieved in Section 5.3. In Section 5.4, we compare the results obtain in this chapter with the observational data of S-type planets. Finally our conclusions are given in Section 5.5.

5.2 Wide binary stars

In this section, we describe the 3200 simulations carried out to study the influence of a wide binary companion on the evolution of two giant S-type planets migrating in the disk. This study extends the one performed in the previous chapter by focusing this time on two-planet systems and in particular on the resonance capture between the two planets during the protoplanetary disk phase.

5.2.1 Simulation set-up

For the numerical simulations, we adopted the same mass, semi-major axis, eccentricities and inclinations for the binary companion as in Chapter 4. They are recalled in Table 5.1. Two giant planets with various masses and initial locations are considered. The semi-major axes of the planets are chosen randomly between 5 and 7 AU for the inner planet and between 12 and 21 AU for the outer planet, in order to allow different mean motion resonance captures during the migration. The closest initial location of the two planets is beyond the 2:1 resonance $((12/7)^{3/2} \simeq 2.24)$, while the furthest one is beyond the 8:1 resonance $((21/5)^{3/2} \simeq 8.61)$. The masses, eccentricities, inclinations and arguments of the pericenters of the planets are chosen in the same ranges as in the single planet case. All the other angles are chosen randomly, as shown in

Table 5.1. For each combination of the fixed parameters of the binary companion, we drew 100 different system configurations from the random parameters. Note that in the following, subscripts 1 and 2 refer to the inner planet and outer planet, respectively.

Following, e.g., Libert and Tsiganis (2011a); Teyssandier and Terquem (2014), and Sotiriadis et al. (2017), we apply an inward migration to the outer planet only (this approach favors convergent migration), while the eccentricity and inclination damping due to the disk is applied on both planets. For the integration, we used a time step of 0.005 yr for the disk phase and 0.01 yr for the dynamical evolution after the dispersal of the disk. The simulations were carried out for 100 Myr.

5.2.2 Typical examples

We start by presenting some typical evolutions observed in the simulations. For each system, we will first focus our attention on the disk phase and then switch to the long-term dynamical evolution after the dispersal of the disk.

For the first system presented in Fig. 5.1, we observe that the outer planet (red color) migrates inward (decrease of the semi-major axis) and is captured at about 0.25 Myr in a mean motion resonance (hereafter, MMR) with the inner planet (green color). The ratio between the periods of the two planets indicates the 2:1 MMR, which is confirmed by the libration of both resonant angles $\theta_1 = 2\lambda_2 - \lambda_1 - \varpi_1$ and $\theta_2 = 2\lambda_2 - \lambda_1 - \varpi_2$, with $\lambda = \omega + \Omega + M$ and $\varpi = \omega + \Omega$ being the mean longitude and the longitude of the pericenter, respectively. Due to the capture in MMR, the eccentricity of the inner planet increases while the outer planet is kept on a circular orbit due to its higher mass. The increase in eccentricities is limited due to the eccentricity damping by the disk. The mutual inclination between the planets also slightly increases and is rapidly damped by the disk. As observed in Chapter 4, we see that the disk keeps the planets inside of itself during the whole disk phase.

The dynamical evolution of the system after the dispersal of the disk is presented in Fig. 5.2. We observe that the MMR is preserved during the long-term evolution. No evidence of a Lidov-Kozai resonance with the highly inclined binary companion is observed (in particular no libration of the pericenter arguments around 90° or 270°). This is due to the strong gravitational interaction between the planets, as we will show later in the chapter.

We also notice the linear evolution of the longitude of the ascending node which, coupled with the conservation of the inclinations, corresponds to the nodal precession of the planets due to the binary companion, as observed in Chapter 4 for the disk precession due to the binary companion. The nodal precession of the planets can also be easily observed in the initial disk plane

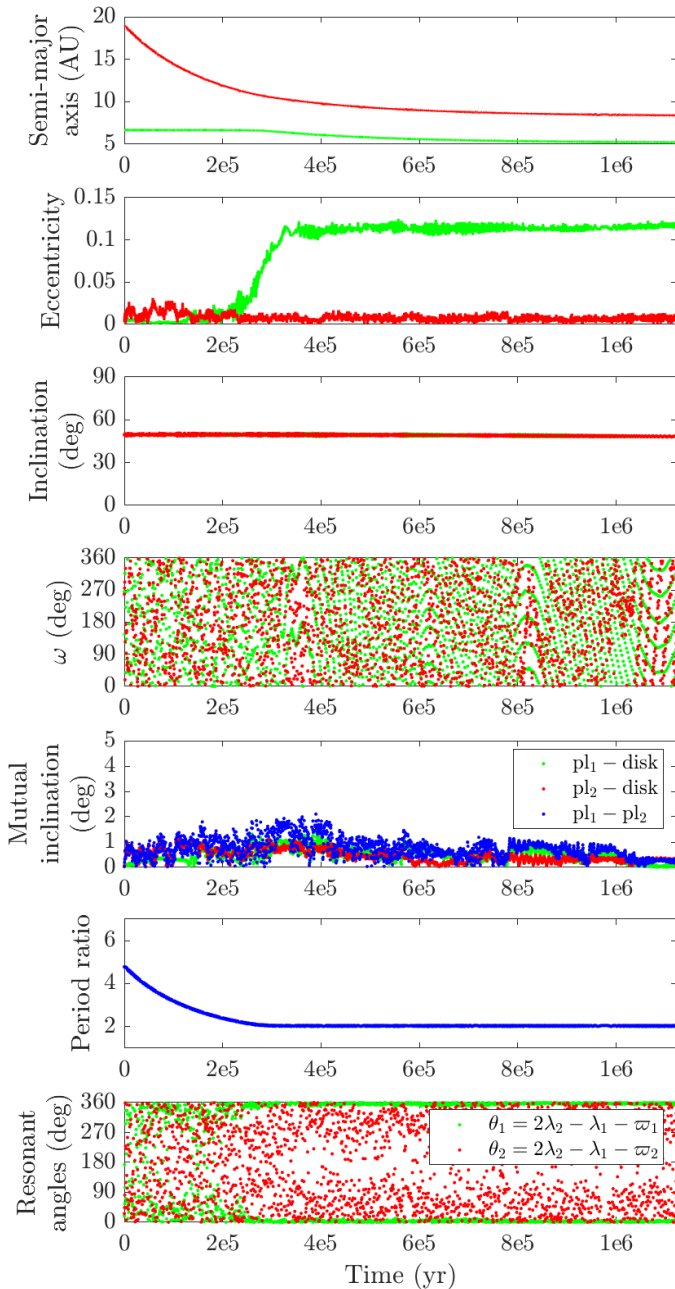


Figure 5.1 – Typical evolution during the disk phase of a system of two giant planets (in the Laplace plane reference frame). The initial parameters (with respect to the disk plane) are $e_B = 10^{-3}$ and $i_B = 50^\circ$ for the binary companion and $a_1 = 6.7$ AU, $m_1 = 1.44 M_{\text{Jup}}$, $a_2 = 18.9$ AU, and $m_2 = 3.55 M_{\text{Jup}}$ for the planets.

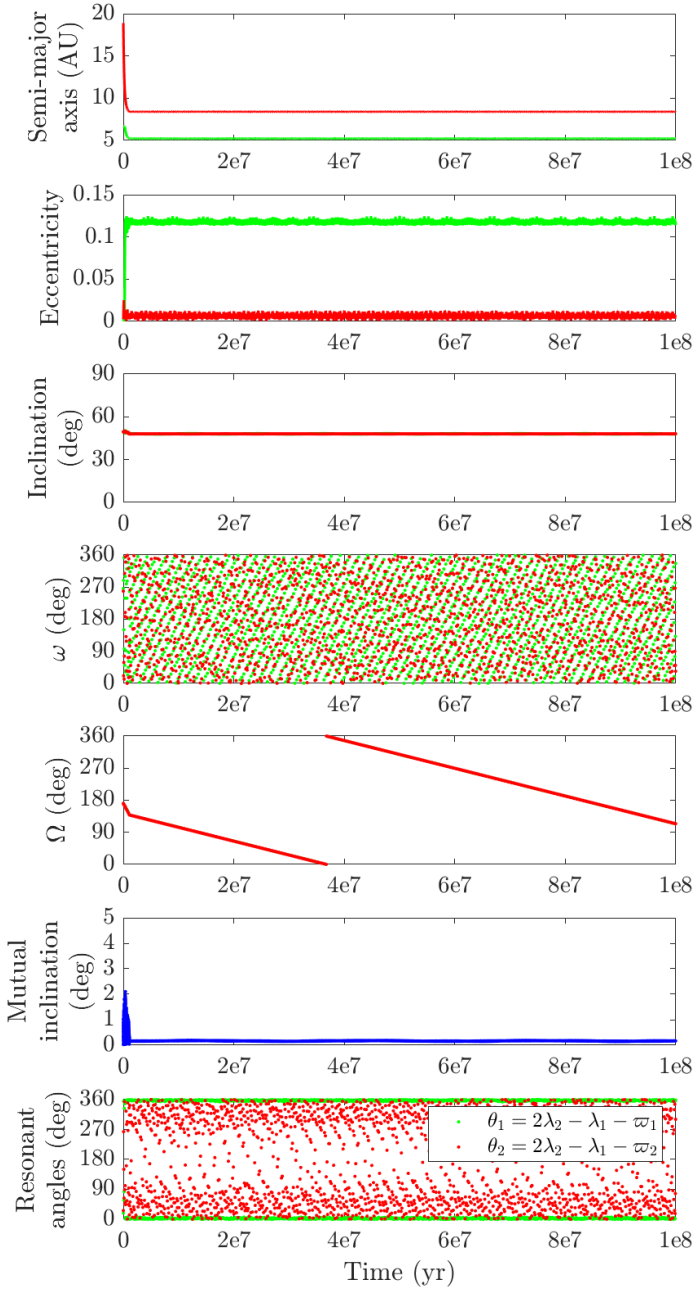


Figure 5.2 – Dynamical evolution of the system presented on Fig. 5.1 after the dispersal of the disk (in the Laplace plane reference frame).

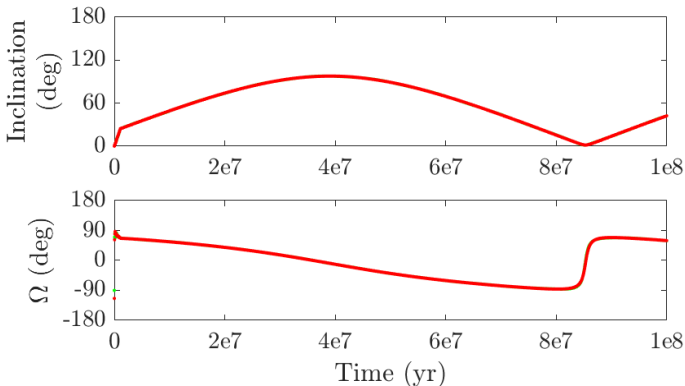


Figure 5.3 – Same inclination evolution as in Fig. 5.2, in the initial disk plane reference frame.

reference frame (Fig. 5.3). We note that the period of the precession is different for the disk and the planets as it can be deduced from the break in the inclination curves at the dissipation of the disk in Fig. 5.3. While an inclination variation between 0 and $2i_B$ is present as expected, we observe that the evolution of the longitude of the ascending node is not linear.

A second system is presented in Fig. 5.4. We observe a behavior similar to the one of the previous system. However, in this case, the eccentricities of both planets increase after the capture in MMR due to their comparable masses. After the disk phase, a scattering event rapidly occurs leading to the ejection of the outer planet. The remaining planet has a behavior similar to the one presented in Chapter 3 for one-planet systems and could potentially be captured in a Lidov-Kozai resonance with the binary companion, as it is the case for the system in Fig. 5.5.

In some cases, the destabilization of the system is observed during the disk phase, as illustrated in Fig. 5.6. At about 0.25 Myr, while the planets evolve in the 3:1 MMR and continue to migrate, a scattering event occurs. The outer planet is scattered to a larger separation and does not evolve in the disk anymore. The evolution of the planets becomes chaotic, as shown in Fig. 5.7. The planets alternate between Lidov-Kozai resonance states and non-resonant evolutions (see the evolution of the arguments of pericenter of both planets), until the ejection of the two planets at ~ 6 Myr.

5.2.3 Parameter distributions

We will now study the system configurations at the dispersal of the disk and at the end of the simulation for the 3200 simulations performed in this work.

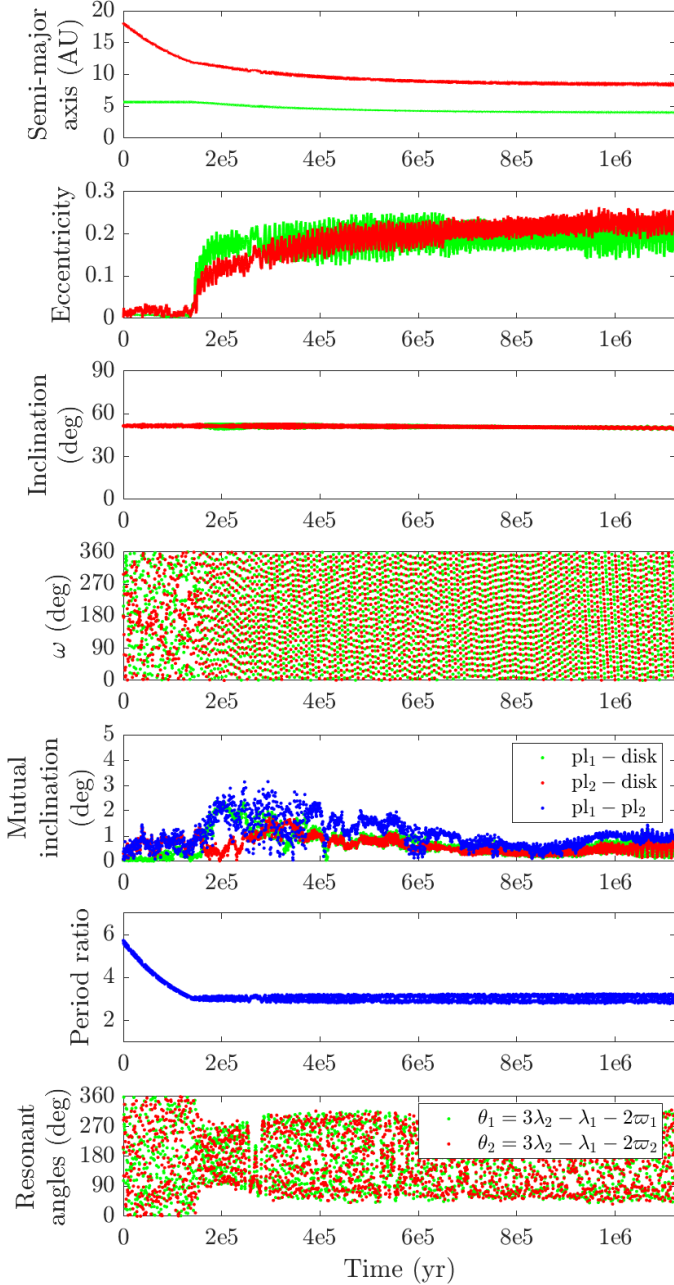


Figure 5.4 – Typical evolution (in the Laplace plane reference frame) of a system of two giant planets experiencing a chaotic evolution after the disk phase (see Fig. 5.5). The initial parameters (with respect to the disk plane) are $e_B = 0.5$ and $i_B = 50^\circ$ for the binary companion and $a_1 = 5.7$ AU, $m_1 = 2.77 M_{\text{Jup}}$, $a_2 = 18.15$ AU, and $m_2 = 2.99 M_{\text{Jup}}$ for the planets.

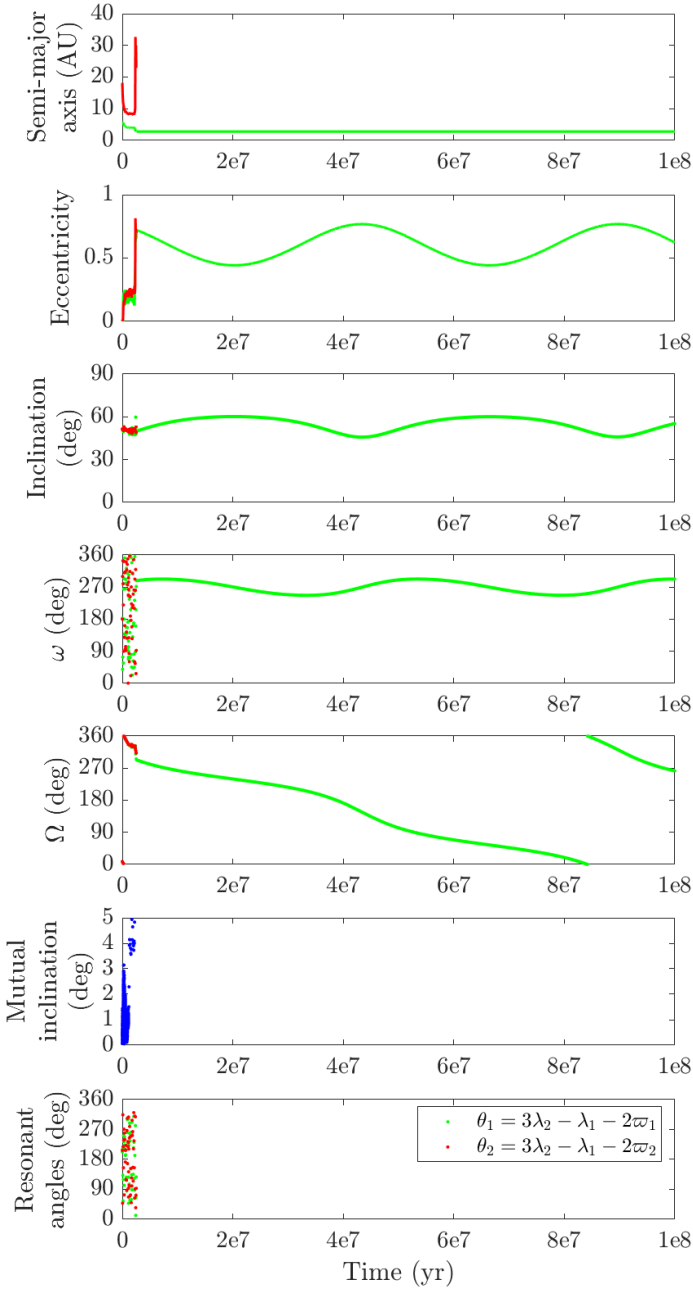


Figure 5.5 – Dynamical evolution of the system presented in Fig. 5.4 after the dispersal of the disk (in the Laplace plane reference frame).

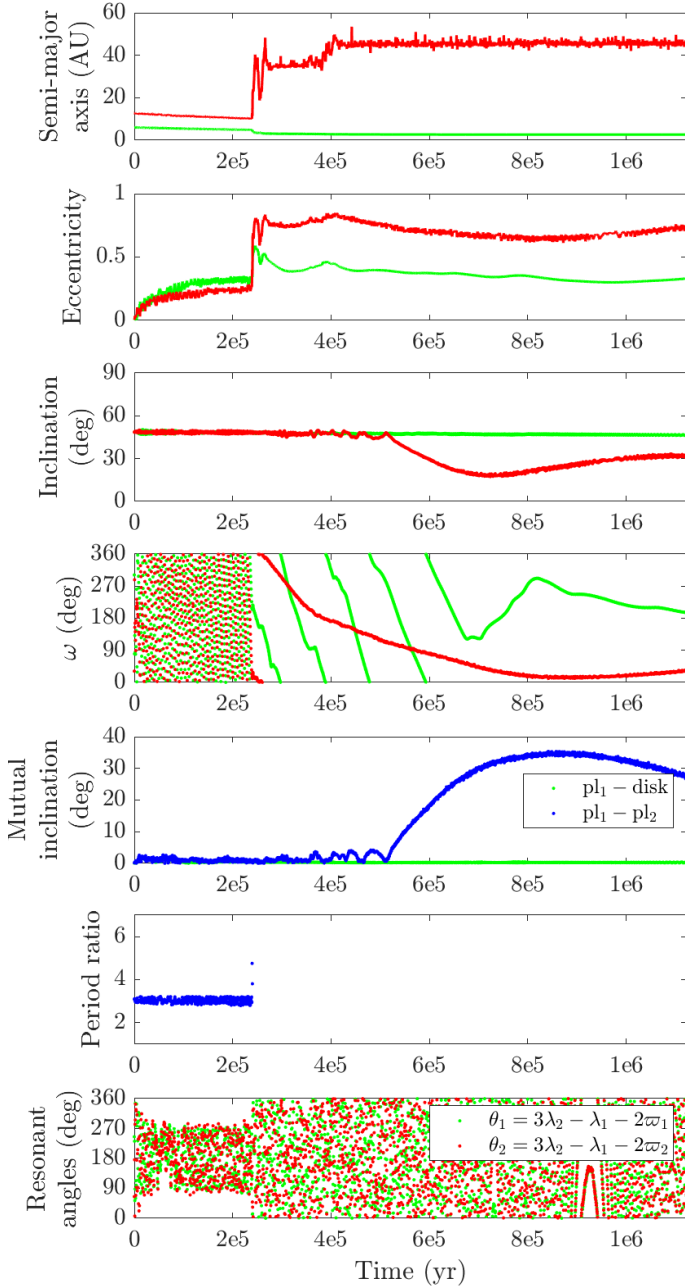


Figure 5.6 – Typical evolution (in the Laplace plane reference frame) of a system of two giant planets experiencing a destabilization during the disk phase. The initial parameters (with respect to the disk plane) are $e_B = 0.1$ and $i_B = 50^\circ$ for the binary companion and $a_1 = 6$ AU, $m_1 = 4.11 M_{\text{Jup}}$, $a_2 = 12.74$ AU, and $m_2 = 3.47 M_{\text{Jup}}$ for the planets.

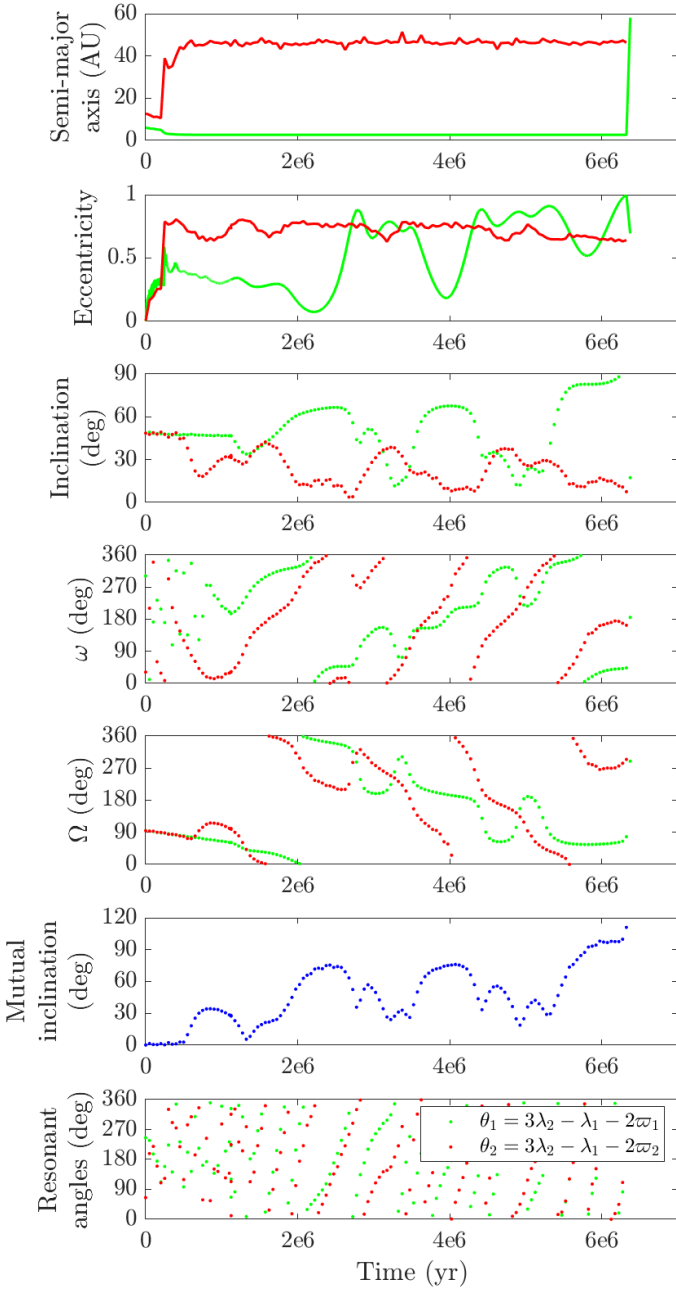


Figure 5.7 – Dynamical evolution of the system presented in Fig. 5.6 after the dispersal of the disk (in the Laplace plane reference frame).

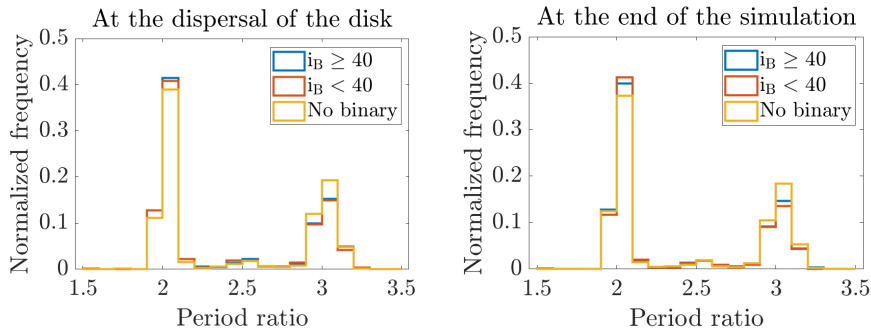


Figure 5.8 – Period ratio distribution of the systems at the dispersal of the disk (left panel) and at the end of the simulation (right panel). The color code refers to the presence of a binary companion and to its inclination value for the systems with a companion.

To further understand the results, we split the simulations in two sets: the systems for which the inclination of the binary companion is strictly below 40° and the ones for which the binary companion is highly inclined ($i_B \geq 40^\circ$). Let us note that we also run the 3200 simulations without the binary companion for comparison.

We first look at the period ratios between the planets to study the MMR captures. We observe in Fig. 5.8 that the two prevalent MMRs seem to be the 2:1 MMR followed by the 3:1 MMR. Several systems seem also trapped in the 5:2 MMR. We also see that the systems with a binary companion (blue and orange curves) tend to be more captured in the 2:1 MMR and less captured in the 3:1 MMR, compared with the systems without a binary companion (yellow curve). As expected, a higher prevalence of first order MMRs is observed due to the gravitational perturbation of the binary companion during the migration. We do not observe any significant influence of the inclination of the binary companion since the histogram for systems with a highly inclined companion (blue curve) looks similar to the one with a less inclined companion (orange curve). Comparing the left and right panels showing the distributions at the dispersal of the disk and at the end of the simulation, respectively, leads us to the conclusion that the systems captured in a MMR stay trapped for a long time (100 Myr in this case), even under the influence of the binary companion. This shows that in the case investigated here, chaotic evolutions after the disk phase are rather limited in two-planet resonant systems. To confirm the previous results, we studied the evolution of the resonant angles for each system. Practically, the planets are considered as trapped in a MMR if at least one of the resonant angles librates with an amplitude of maximum 270° during

Table 5.2 – Percentages of the different system configurations at the dissipation of the disk.

Final systems	MMR	Binary	Binary	No binary
		($i_B \geq 40^\circ$)	($i_B < 40^\circ$)	
2 planets	2:1	53.37	53.87	49.7
	3:1	28.56	27.87	34.4
	5:2	0.68	0.63	1.16
	other MMR	0.15	0.25	1.58
	no MMR	14.5	14.88	10.66
1 planet		2.43	2.5	2.34
no planet		0.31	0	0.16

the 0.2 Myr before the time considered, namely the dissipation of the disk or the end of the simulation. The results on the MMR captures are gathered in Tables 5.2 and 5.3. In Table 5.2, we observe, as previously deduced from the period ratios, that, at the dispersal of the disk, there are more systems trapped in the 2:1 MMR for systems with a binary companion (53.6% against 49.7%) while it is the contrary for the 3:1 MMR (28.2% against 34.4%) and the 5:2 MMR (0.6% against 1.2%). We also note that there are less systems trapped in a MMR with a binary companion than without (14.7% against 10.7%). Let us note that the same percentage of planetary ejections is observed for single star systems and binary star systems. In Table 5.3, we note that the different proportions about the MMR captures observed previously are maintained at the end of the simulations. However, the percentages of final one-planet systems have increased, in particular for binary star systems due to chaotic events occurring after the dispersal of the disk. Examples of chaotic evolution after the disk phase have been shown in Fig. 5.5 and 5.7. Most probably, the two-planet systems are in stable configurations at the end of the simulations. A thorough study of the stability of these systems is left for future work. Note that we do not observe significant differences in Table 5.3 between systems with a highly inclined binary companion and those with a less inclined companion.

The eccentricity distribution of the different systems is shown in Fig. 5.9. We observe that the single star systems tend to have higher eccentricities (orange and blue curves above the yellow curve for eccentricities below 0.25 while the yellow curve is above the two others for higher values). This observation is coherent with the percentages of resonance captures. Indeed, resonance captures are generally followed by an increase of the planetary eccentricities (see the examples of Section 5.2.2). Since the single star systems are more likely to be trapped in a MMR, these systems present higher eccentricities. Again, the

Table 5.3 – Percentages of the different system configurations at the end of the simulation

Final systems	MMR	Binary ($i_B \geq 40^\circ$)	Binary ($i_B < 40^\circ$)	No binary
2 planets	2:1	53.44	54.06	49.8
	3:1	26.63	25	33.03
	5:2	0.56	0.25	0.72
	other MMR	0.12	0.26	1.65
	no MMR	12.81	13	9.78
1 planet		6.06	7.43	4.9
no planet		0.38	0	0.16

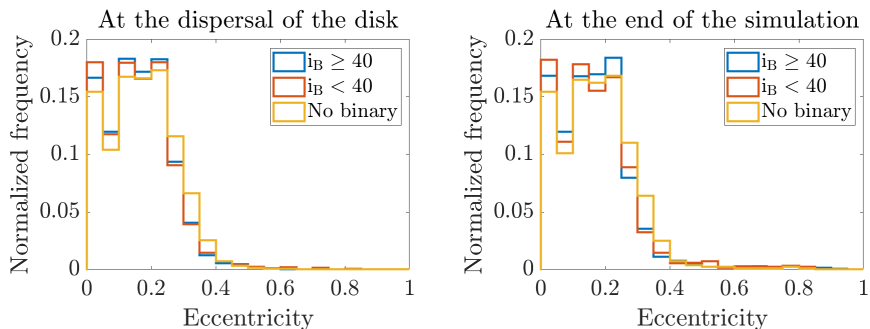


Figure 5.9 – Eccentricity distribution of the systems at the dispersal of the disk (left panel) and at the end of the simulation (right panel).

similar profile between the curves on the left panel (at the dispersal of the disk) and on the right panel (at the end of the simulation) leads us to say that the binary companion has a limited influence on the system even after the dispersal of the disk, in the case investigated here.

In Fig. 5.10, we show the distribution of the mutual inclination between the planets. We observe mutual inclination values slightly higher for systems including a binary companion. However, most of the mutual inclinations are below 5° . Only 3% of the systems have a mutual inclination above 5° in binary star systems. Again, we could expect an influence of the binary companion leading to a significant increase of the mutual inclinations. It is not the case here even after the dispersal of the disk since the right panel looks similar to the left one. We also do not notice an influence of the inclination of the binary companion since the blue histogram is similar to the orange one. The distribution in mutual inclination is consistent with the eccentricity distribution in Fig 5.9.

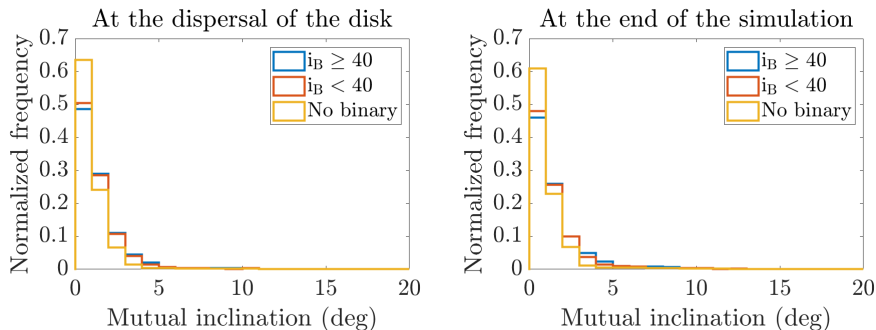


Figure 5.10 – Distribution of the mutual inclination between the two planets at the dispersal of the disk (left panel) and at the end of the simulation (right panel).

It has been reported that while inclination-type resonance mainly operates for large eccentricities (Thommes and Lissauer, 2003; Libert and Tsiganis, 2009b; Teyssandier and Terquem, 2014; Sotiriadis and Libert, 2020), inclination excitation can also be present at small to moderate eccentricities in systems with more than two planets (Libert et al., 2018). This mechanism could also explain the mutual inclinations above 5° observed in Fig. 5.10. An example of a highly mutually inclined system is shown in Fig. 5.11. We first observe a temporary capture in a 3:1 MMR, before a second capture in a 5:2 MMR. The eccentricities increase to moderate values and the inclinations suddenly grow at 9×10^5 yr. It seems that the system at this time enters an inclination-type resonance increasing the mutual inclination of the planets. To understand better the inclination increase, we display at the bottom panel of Fig. 5.11 the evolution of the angle $\theta_{i_1^2} = 5\lambda_2 - 2\lambda_1 - \varpi_1 - 2\Omega_1$ and the evolution of the inclination (in logarithmic scale). We see that the inclination increases in correlation with the libration of the inclination-type resonant angle $\theta_{i_1^2}$.

To further analyze the influence of the binary companion, in particular the Lidov-Kozai mechanism, we now focus on the pericenter argument of the planets. Fig. 5.12 displays the pericenter argument distributions at the dissipation of the disk (left panel) and at the end of the simulation (right panel). We do not notice any specific pattern associated to the Lidov-Kozai resonance (i.e. accumulations around 90 or 270°). The graph in the left panel is similar to the right panel of Fig. 4.8 in which the Lidov-Kozai resonance was suppressed by the gravitational effect of the disk. Regarding the evolution after the disk phase (right panel of Fig. 5.12), the gravitational interaction between the two planets seems to overcome the effect of the binary companion and the establishment of a Lidov-Kozai resonant evolution in highly inclined binary systems. We will

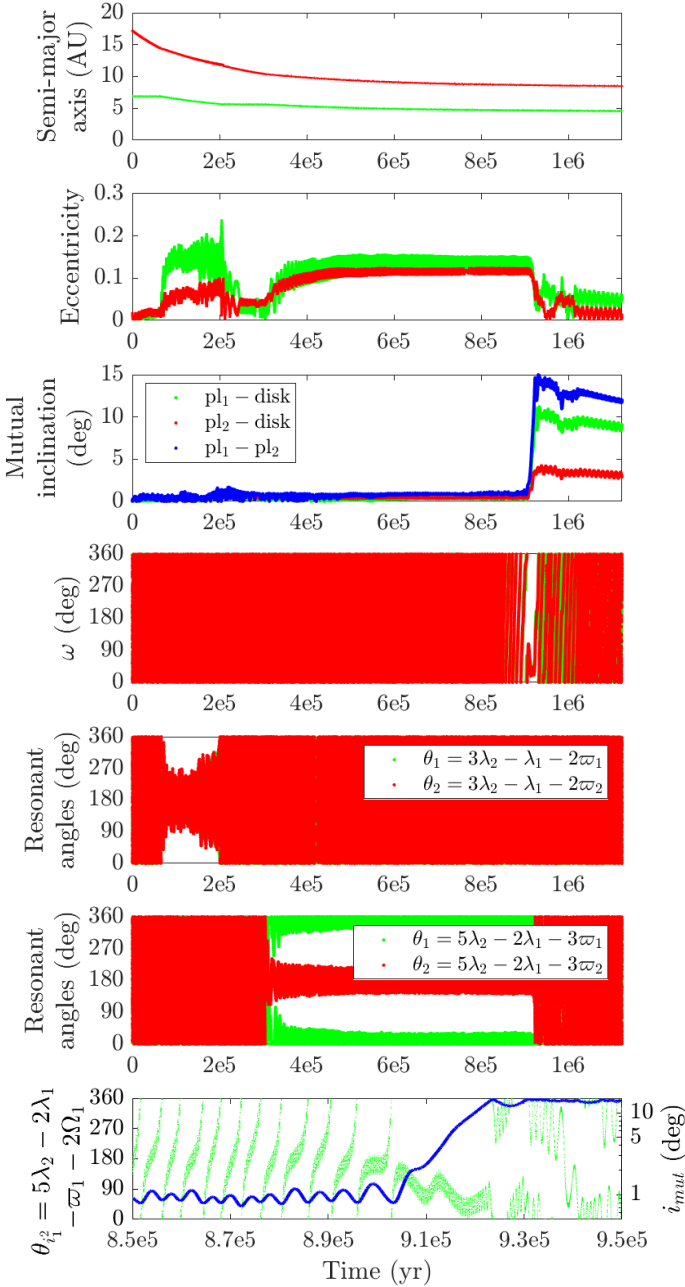


Figure 5.11 – Typical evolution (in the Laplace plane reference frame) of a system of two giant planets experiencing an inclination-type resonance during the disk phase. The initial parameters (with respect to the disk plane) are $e_B = 0.5$ and $i_B = 0.001^\circ$ for the binary companion and $a_1 = 6.86$ AU, $m_1 = 1.64 M_{\text{Jup}}$, $a_2 = 17.1$ AU, and $m_2 = 3.79 M_{\text{Jup}}$ for the planets.

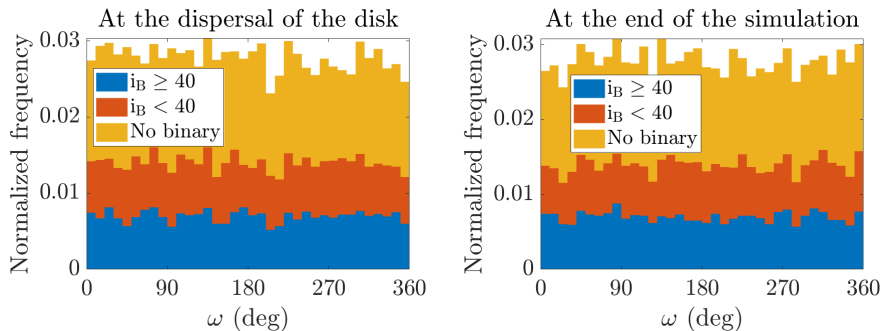


Figure 5.12 – Pericenter argument distribution for the systems at the dispersal of the disk (left panel) and at the end of the simulation (right panel). The pericenter arguments are given in the Laplace plane reference frame.

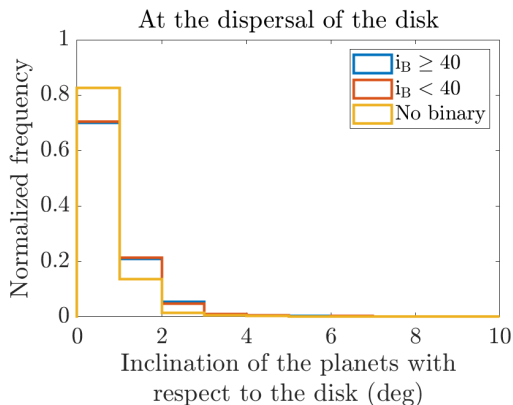


Figure 5.13 – Distribution of the mutual inclination between the planets and the disk at the dispersal of the disk.

further study this observation in the next section. Note that we also numerically investigated the libration of the pericenter arguments in the same way as in the two previous chapters and observed that only the systems suffering from an ejection possibly ended with a planet locked in the Lidov-Kozai resonance.

Fig. 5.13 presents the mutual inclination between the planet and the disk at the dispersal of the disk. As observed in the previous section, the disk almost keeps the planets in itself during the disk phase thanks to the gravitational potential of the disk and the disk inclination damping. We note that the planets tend to be slightly more misaligned with respect to the disk in systems with a binary companion but this misalignment is not significant (less than 4°).

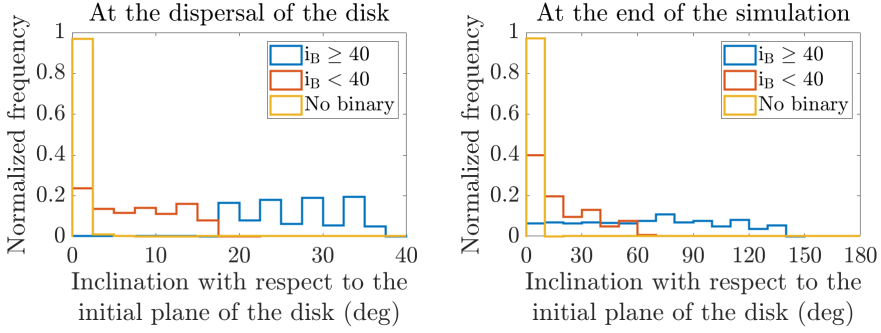


Figure 5.14 – Inclination distribution at the dissipation of the disk (left panel) and at the end of the simulation (right panel). The inclinations are given in the initial disk plane reference frame.

In Fig. 5.14, we display the planetary inclinations with respect to the initial plane of the disk. We observe in the left panel displaying the inclinations at the dispersal of the disk, that for binary star systems the planetary inclinations are proportional to the inclination of the binary companion. This is coherent with the precession of the disk due to the binary companion, which induces a periodic variation with an amplitude equal to $2i_B$ (see Fig. 4.2 of Chapter 4). Since the planets tend to stay coupled with the disk as seen in Fig. 5.13, they follow the nodal precession of the disk, which explains the inclination distribution in the left panel of Fig. 5.14. On the right panel, we observe that the inclination is amplified during the dynamical phase. This is a consequence of the nodal precession induced by the binary companion acting this time on the coupled planets, as observed in Fig. 5.3. Remark that this precession has the same amplitude as the one of the disk induced by the binary companion calculated in the previous chapter. Note also that the nodal frequency depends on the orbital parameters of the planets leading to a more uniform spread than in the left panel. Moreover, on the right panel, we observe that the normalized frequencies decrease with the inclination. This effect comes from the amplitude of the nodal precession. Indeed, we have 400 systems for each inclination of the binary, whose planetary inclinations are uniformly spread between 0 and $2i_B$, leading to an accumulation around the smallest values. The nodal precession induced by the binary companion thus creates a misalignment between the spin axis of the primary star and the angular momentum of the planets.

5.3 Importance of the Lidov-Kozai effect for two-planet systems

In this section, we study more precisely the articulation between the Lidov-Kozai effects caused by the binary companion and the gravitational interaction between the two giant planets.

5.3.1 State of the art

It has been shown that all effects inducing a precession of the pericenter of a planet faster than the one induced by the Lidov-Kozai resonance act to suppress it. It is the case with, e.g., general relativity, tidal and rotational bulges or, as here, gravitational interaction with another planet (Wu and Murray, 2003; Fabrycky and Tremaine, 2007; Takeda et al., 2008). The timescale associated to the Lidov-Kozai resonance with a binary companion, τ_{LK} , can be approximated by (Kiseleva et al., 1998)

$$\tau_{\text{LK}} = \frac{2}{3\pi} \frac{P_B^2}{P} (1 - e_B^2)^{3/2} \frac{m_A + m + m_B}{m_B}, \quad (5.1)$$

where P_B and P are the orbital period of the binary companion and the planet, respectively, e_B the eccentricity of the binary, and m_A and m the mass of the primary star and the planet, respectively. The timescale of the pericenter precession induced by the gravitational interaction between two planets, denoted τ_{pl} , is more tricky but can be approximated under some assumptions as shown by Takeda et al. (2008). By using the Laplace-Lagrange secular theory, the timescale can be approximated by means of the eigenvalues of the following matrix (Murray and Dermott, 1999; Takeda et al., 2008) :

$$A = \begin{pmatrix} c_1 & -c_0 c_1 \\ -c_0 c_2 & c_2 \end{pmatrix} \quad (5.2)$$

with

$$\begin{aligned} c_0 &= \frac{b_{3/2}^{(2)}(\alpha)}{b_{3/2}^{(1)}(\alpha)} \\ c_1 &= \frac{1}{4} n_1 \frac{m_2}{m_A + m_1} \alpha^2 b_{3/2}^{(1)}(\alpha) \\ c_2 &= \frac{1}{4} n_2 \frac{m_1}{m_A + m_2} \alpha^2 b_{3/2}^{(1)}(\alpha), \end{aligned} \quad (5.3)$$

where $b_{3/2}^{(1)}(\alpha)$ and $b_{3/2}^{(2)}(\alpha)$ are the Laplace coefficient of the first and second kind, respectively, $\alpha = \frac{a_1}{a_2}$, and n_j the planetary mean motions ($j = 1, 2$). The

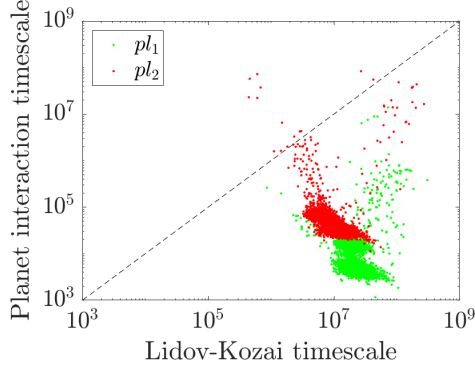


Figure 5.15 – Timescale of the pericenter precession due to the gravitational interaction between the planets versus the Lidov-Kozai timescale due to the binary companion. The green and red colors refer to the inner planet and outer planet, respectively.

expressions of the eigenvalues are (Zhou and Sun, 2003):

$$g_+ = \frac{1}{2} \left(c_1 + c_2 + \sqrt{(c_1 - c_2)^2 + 4c_0^2 c_1 c_2} \right) \quad (5.4)$$

$$g_- = \frac{1}{2} \left(c_1 + c_2 - \sqrt{(c_1 - c_2)^2 + 4c_0^2 c_1 c_2} \right). \quad (5.5)$$

The timescale of the pericenter precession τ_{p1} for each planet is thus given by $2\pi/g_+$ and $2\pi/g_-$ with the highest value associated with the most massive planet. This approximation is accurate under the condition presented in Takeda et al. (2008) :

$$\frac{\alpha}{1 - 3q\sqrt{\alpha}/b_{3/2}^{(1)}(\alpha)} \ll 1 \quad (5.6)$$

with $q = m_2/m_1$. In our work, the condition is not always fulfilled but even when it is not the case, the formula will anyway give us an indication about the order of magnitude of the precession timescale.

The timescales discussed here are shown in Fig. 5.15 for the 3200 simulations of the previous section with the system parameters at the dispersal of the disk. As previously observed, for nearly all the systems, the Lidov-Kozai timescale is much longer than the timescale associated with the gravitational interaction between the planets, which explains that the influence of the binary is very limited in the simulations of the previous section. Note that for systems close to the identity line, the dominant effect is unsure.

Table 5.4 – Initial parameters for the second set of simulations. The orbital elements are expressed with respect to the initial plane of the disk.

	Central star	Inner planet	Outer planet	Binary companion
mass	$1 M_{\odot}$	$U[1;5] M_{\text{Jup}}$	$U[0.65;5] M_{\text{Jup}}$	$1 M_{\odot}$
a (AU)		$U[7.5, 10.5]$	$U[20, 30]$	250, 500, 750, 1000
e		$U[0.001;0.01]$	$U[0.001;0.01]$	10^{-3} , 0.1, 0.3, 0.5
i ($^{\circ}$)		$U[0.01;0.1]$	$U[0.01;0.1]$	10^{-3} , 10, 20, 30, 40, 50, 60, 70
Ω ($^{\circ}$)		$U[0, 360]$	$U[0, 360]$	$U[0, 360]$
ω ($^{\circ}$)		$U[0, 360]$	$U[0, 360]$	$U[0, 360]$
M ($^{\circ}$)		$U[0, 360]$	$U[0, 360]$	$U[0, 360]$

5.3.2 Second set of simulations

Based on the observations related to Fig. 5.15, we aim to realize a parametric study to identify the parameter values leading to an increase of the ratio between the precession timescale τ_{pl} and the Lidov-Kozai timescale τ_{LK} . Following Eq. (5.1), to reduce the Lidov-Kozai timescale, we will decrease the semi-major axis of the binary companion by adopting the values 250 AU, 500 AU, and 750 AU. Note that when the binary companion is closer to the primary star, our disk model will suffer from some limitations that will be discussed in detail in Section 5.3.4. We will also increase the initial semi-major axes of the planets by multiplying their range of values by 1.5 such that their orbital period will be longer at the dispersal of the disk. A last change will consist in decreasing the lower bound on the planetary masses to $0.65 M_{\text{Jup}}$. The new parameters are gathered in Table 5.4. For each combination of the parameters of the binary, we randomly draw 50 different initial conditions for the planetary parameters, as previously done. In total we ran 8000 simulations (single star simulations included).

We now study the system configurations resulting from the second set of simulations. In Fig. 5.16, we reproduce the same plot as in Fig. 5.15 for the different semi-major axes of the binary companion considered here. We see that the smaller the semi-major axis of the binary, the closer the systems to the dashed line of equal timescales. As a result, the impact of the binary companion will be stronger for simulations with $a_B = 250$ AU and $a_B = 500$ AU. Note that those results are consistent with what was expected from Eqs. (5.1), (5.4) and (5.5).

About the mean motion resonances, a variation in the initial semi-major axes of the planets leads to a modification of their migration rates and thus

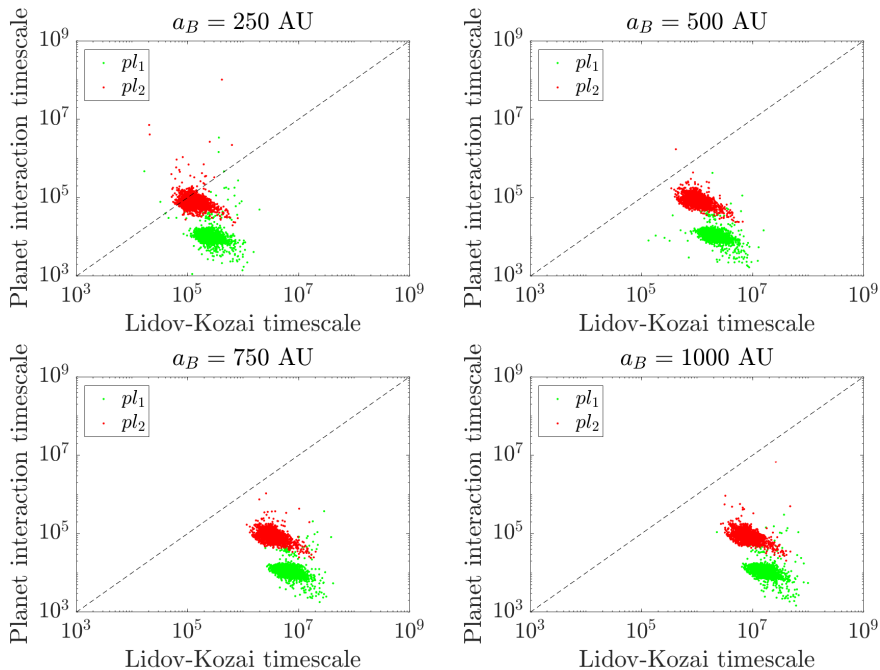


Figure 5.16 – Same as Fig. 5.15 for the different semi-major axes of the binary companion.

the MMR captures. Almost all the resonant systems are trapped in the 2:1 MMR. Tables 5.5 and 5.6 show the different system configurations found at the dispersal of the disk and at the end of the simulation, respectively. During the disk phase, the conclusions are similar to the ones made in Section 5.2, apart from the slightly higher number of ejections for the systems with a binary companion at 250 AU. At the end of the simulation, a lot of ejections are reported for the simulations with $a_B = 250$ AU. For all the other binary semi-major axes, the influence of the binary companion is still quite limited. In the next section, we will therefore focus our attention on the systems with the binary companion at 250 AU.

5.3.3 Parameter distributions for $a_B = 250$ AU

We noticed that contrary to the previous cases, when the binary companion is at 250 AU, the inclination of the planets with respect to the binary plane was modified during the disk phase. In the previous cases, the planets were maintained in the disk whose inclination with respect to the binary companion was almost constant (see Fig. 4.7). In this case, as it can be seen in Fig. 5.17,

Table 5.5 – Percentages of the different system configurations at the dissipation of the disk for the second set of simulations.

	250 AU	500 AU	750 AU	1000 AU	No binary
2 planets - MMR	87.81	90.94	90.75	90.68	91.31
2 planets - no MMR	9.75	8.62	8.68	8.63	8.37
1 planet	2	0	0	0	0
no planet	0.44	0.44	0.57	0.69	0.32

Table 5.6 – Same as Table 5.5, but at the end of the simulation

	250 AU	500 AU	750 AU	1000 AU	No binary
2 planets - MMR	57	89.44	90.31	90.5	91.12
2 planets - no MMR	5.25	7.44	8.31	7.87	7.94
1 planet	33.94	2.56	0.82	0.94	0.63
no planet	3.81	0.56	0.56	0.69	0.31

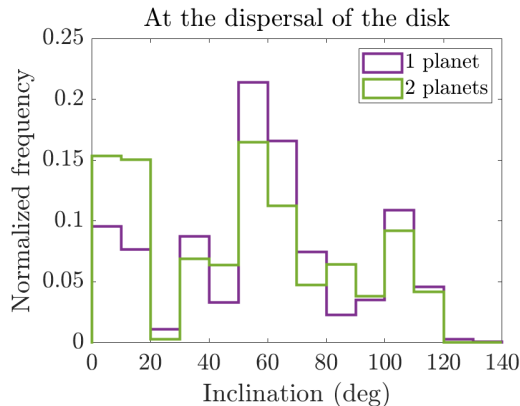


Figure 5.17 – Inclination of the planets at the dissipation of the disk with respect to the Laplace reference plane. The color code indicates the number of planets in the system at the end of the simulation.

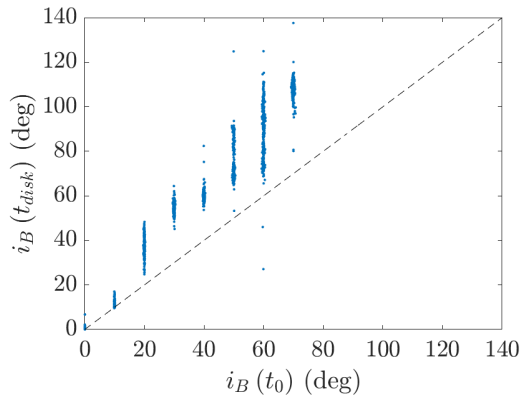


Figure 5.18 – Mutual inclination between the planets and the binary companion at the dispersal of the disk versus the initial value.

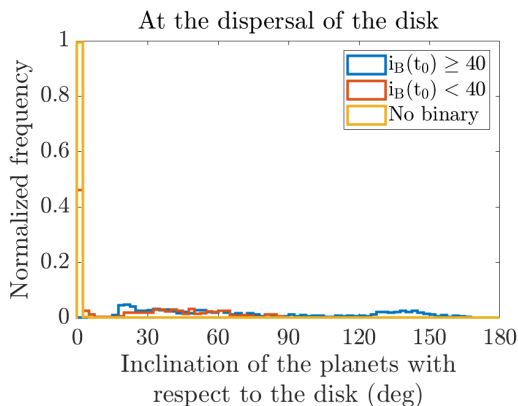


Figure 5.19 – Same as Fig. 5.13 with the binary companion at 250 AU.

the planetary inclinations do not stay close to the typical values chosen initially for the inclination of the binary in Table 5.4. While they are more spread, there is still a correlation with the inclination of the binary companion, as it can be observed in Fig. 5.18 showing the mutual inclination between the planets and the binary companion at the dispersal of the disk (denoted $i_B(t_{disk})$) versus the initial value ($i_B(t_0)$). These changes are caused by the decoupling between the evolutions of the disk and the planets, as illustrated in Fig. 5.19 where we present the distribution of the mutual inclination between the planets and the disk at the dispersal of the disk. Note that in the following, the analysis of the parameter distributions will be based on the inclinations of the binary companion at the dispersal of the disk for the long-term evolution. The groups

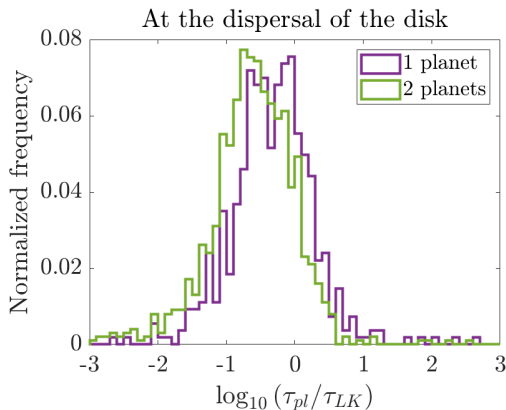


Figure 5.20 – Normalized frequency of the logarithm of the ratio between the timescale of the gravitational interaction between the planets and the Lidov-Kozai timescale. The color code refers to the number of planets in the system at the end of the simulation.

presented in the distributions at the dispersal of the disk will still depend on the initial inclinations of the binary companion.

In Fig. 5.20, we observe that the systems ending with one planet (purple curve) have a mean ratio between τ_{pl} and τ_{LK} higher than the one of systems with two planets at the end of the simulation (green curve). As expected, it shows that systems with both timescales roughly similar experience more planetary ejections.

Fig. 5.21 presents the eccentricity distribution. We observe that systems with a binary companion (cyan curve) tend to be slightly more eccentric than the ones without companion (yellow curve). In particular, at the end of the simulations, the presence of the binary companion can result in highly eccentric planetary orbits. They mainly result from scattering events and ejections during the long-term evolution, as it can be seen in Fig. 5.22. Indeed, for the simulations ending with two planets (right panel), the eccentricity distribution is similar to the one without binary companion and most of the eccentricities are below 0.2. However, almost all the systems with only one planet remaining (left panel) present very eccentric configurations. Note that in Fig. 5.22 we also see that the inclination of the binary companion influences the planetary eccentricities, since we observe that the majority of the highly eccentric systems have a binary companion with an inclination higher than 40° .

About the mutual inclinations between the planets, we do not observe significant differences between Fig. 5.10 and Fig. 5.23. The number of high mutual inclinations is reduced at the end of the simulations (right panel) because many

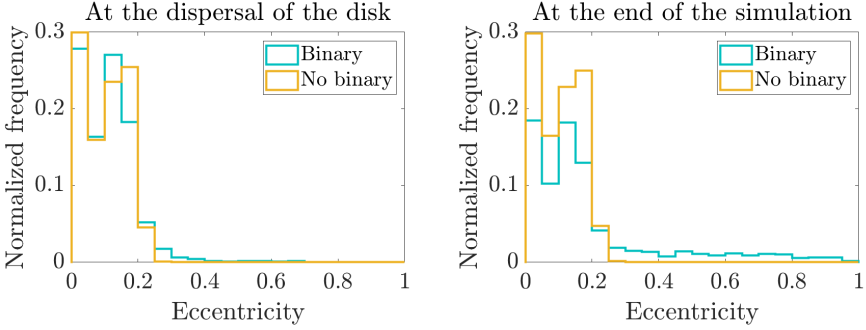


Figure 5.21 – Same as Fig. 5.9 with the binary companion at 250 AU.

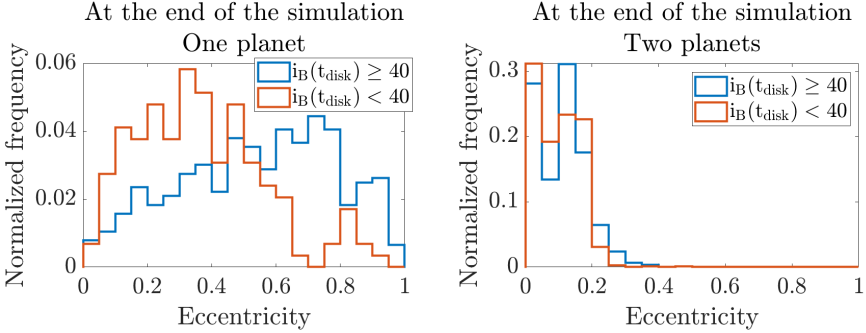


Figure 5.22 – Same as the right panel of Fig. 5.21 with the right and left panels associated with systems composed of one and two planets at the end of the simulation, respectively.

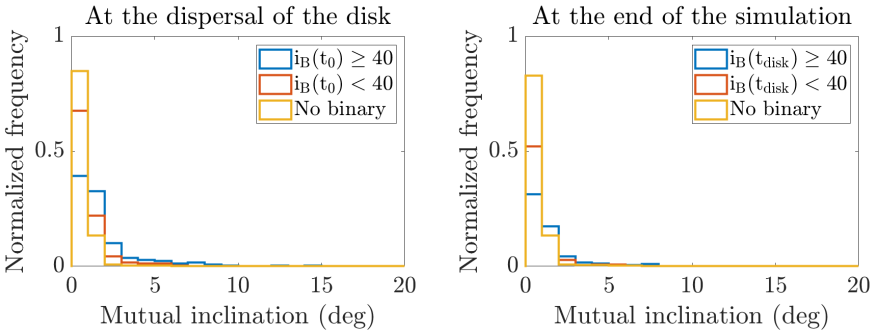


Figure 5.23 – Same as Fig. 5.10 with the binary companion at 250 AU.

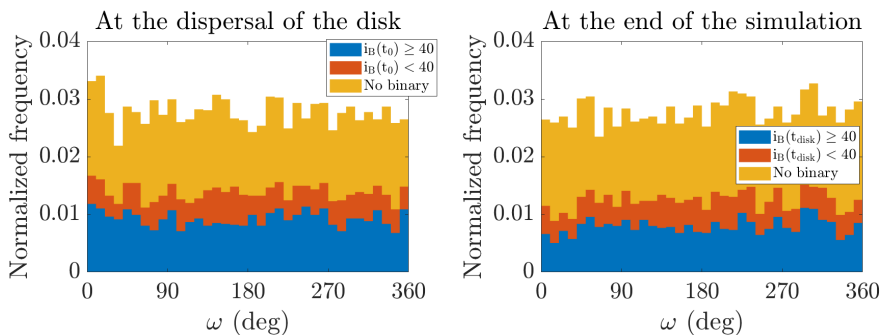


Figure 5.24 – Same as Fig. 5.12 with the binary companion at 250 AU.

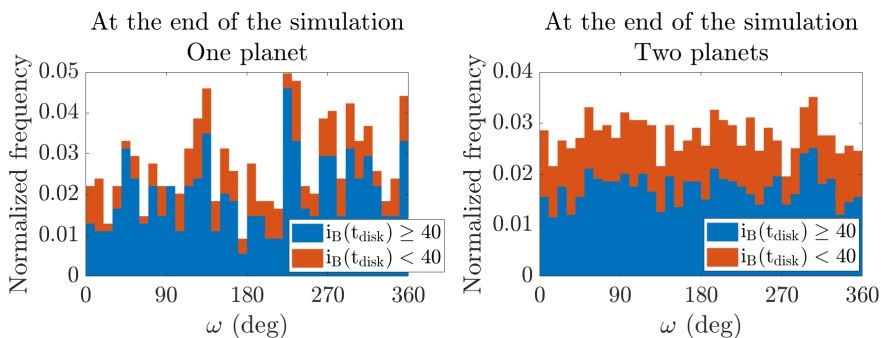


Figure 5.25 – Same as the right panel of Fig. 5.24 with the right and left panels associated with systems composed of one and two planets at the end of the simulation, respectively.

systems have experienced a planetary ejection in their long-term evolution.

As previously, to study the Lidov-Kozai resonance, we display the distribution of the pericenter arguments in Fig. 5.24. The results look quite similar as in Fig. 5.12, with no influence of the Lidov-Kozai resonance. However, if we split the analysis for systems ending with one or two planets, we notice in Fig. 5.25 that the distribution of the systems ending with one planet only (left panel) presents two peaks centered at 90° and 270° , similarly to the ones observed in the previous chapters. Such accumulations are not present for the systems ending with two planets (right panel). A study of the libration of the arguments of pericenters for each system individually, in the same way as previously done, leads us to the observation that no system with two planets end up with one of the planets locked in the Lidov-Kozai resonance. For the one-planet systems, the percentage of the systems locked in the Lidov-Kozai resonance is similar to the one observed in the previous chapter, namely $\sim 30\%$.

In conclusion, we observed that a binary companion close enough to strongly influence the planets will tend to destabilize the system and lead to the ejection of a planet in about one third of the cases. The ejection will possibly induce high eccentricity and evidences of Lidov-Kozai resonance for the remaining planet.

5.3.4 Limitations of the model

In this section we discuss the possible limitations of our disk model for the parameters of the second set of simulations. Indeed, in the whole manuscript, we have assumed that the disk is uniform thanks to the disk self-gravity. Considering closer binary companions as made in the previous section could have the effect to overcome the disk self-gravity and lead to deformations of the disk. Using the code of Section 4.2.2.1 to estimate the nodal precession of the disk with the Laplace-Lagrange theory, we study in Fig. 5.26 the uniformity of the disk for the different semi-major axes of the binary companion considered here. Note that we fix the inclination of the binary companion to $i_B = 60^\circ$ arbitrarily, but the results are similar whatever the chosen inclination. We see that the disk remains uniform for the binary companion at 750 AU and 1000 AU. On the contrary, the disk uniformity is not maintained for 250 AU and 500 AU. This does not mean that the disk is not uniform in this case, but the self-gravity is not sufficient alone to ensure it. Hydrodynamical effects such as radial pressure force and viscous diffusion (e.g., Papaloizou and Terquem, 1995; Larwood et al., 1996) could play a role and keep the disk uniform. For instance, it has been shown that if the wave crossing time in the disk is shorter than the precession time due to the binary companion, the rigidity of the disk could be maintained (Zanazzi and Lai, 2018a). Investigations of such effects is left for future work.

Moreover, the disk could experience Lidov-Kozai cycles due to the presence of the binary companion (see, e.g., Martin et al., 2014; Fu et al., 2015; Zanazzi and Lai, 2017). Batygin et al. (2011) showed that the cycles could be suppressed by the self-gravity of the disk if the disk is massive enough. It could not be the case here since we consider an exponential decrease of the disk mass. In addition, Lidov-Kozai cycles in the disk could lead to eccentric orbits and the hypothesis of the Laplace-Lagrange theory requiring annuli without intersections could not be verified in this case.

Nevertheless, most of the results of the second set of simulations were very similar whatever the semi-major axis considered for the binary companion. The differences observed for $a_B = 250$ AU mainly arise during the dynamical phase after the dispersal of the disk. This phase does not suffer from the limitations in the disk model presented in this section. We therefore conclude that despite

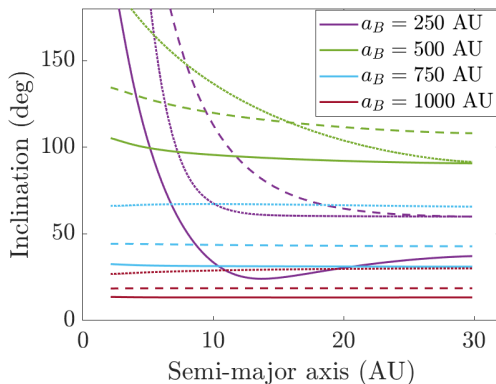


Figure 5.26 – Time evolution of the inclination of the disk as a function of the semi-major axis, for different binary semi-major axes (in the initial disk plane reference frame). The color code refers to the different semi-major axes and the line type to different times. The solid line stands for $t=0.5$ Myr, the dashed line for $t=0.75$ Myr and the dotted line for $t=1.123$ Myr. The inclination of the binary i_B is fixed to 60° .

those limitations, our results are quite robust.

5.4 Comparison with observations

In this section we compare our results with the observations for S-type planets from Rein (2012) presented in Chapter 1. The semi-major axis and mass distributions are influenced by the choices made in the initial parameters, therefore they can not be compared. The comparison of the cumulative eccentricities is made in Fig. 5.27. The eccentricity distribution of Rein (2012) for giant S-type planets is shown by the green curve, while the one of all the detected giant planets is indicated by the black curve. As previously noticed in Chapter 1, the S-type planets are more eccentric. We observe in our simulations that, for the systems with a binary companion at 1000 AU (blue curve) and without binary companion (yellow curve), nearly all the eccentricities are below ~ 0.2 , since the two-planet systems are weakly perturbed during their long-term evolution. For the one-planet systems with a binary companion at 1000 AU analyzed in Chapter 4 (purple curve), high eccentricities can be reached in the presence of a highly inclined binary companion, while binary companions with $i_B < 40^\circ$ do not excite the initial quasi-circular orbits of the planets. As seen in the previous section, two-planet systems with a close binary companion at 250 AU

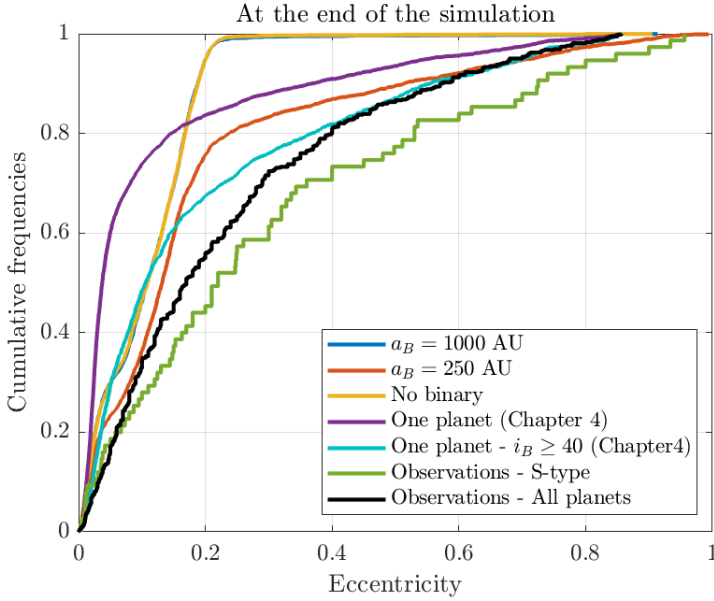


Figure 5.27 – Cumulative eccentricity of the planets found in our simulations and in the observations (Rein, 2012). See text for more detail.

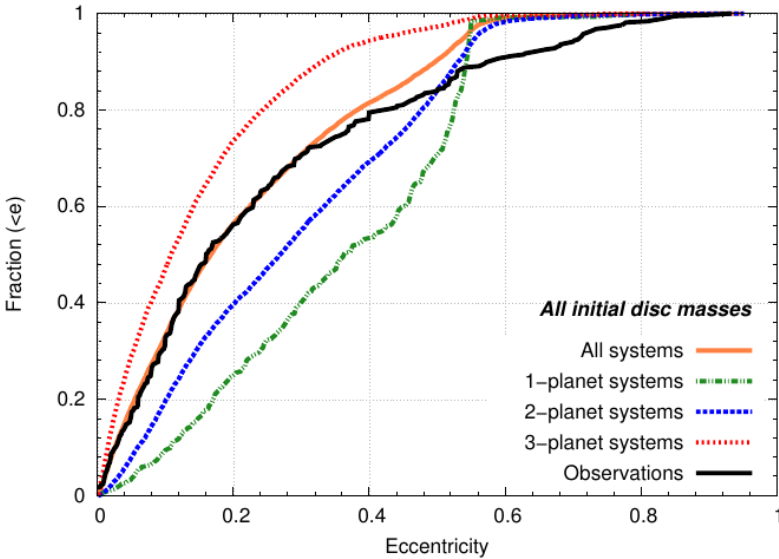


Figure 5.28 – Cumulative eccentricity from Sotiriadis et al. (2017).

can also generate high eccentricities for the planets. As a result, we have shown that the high eccentricities observed for S-type planets in Fig. 5.27 can be explained by highly inclined binary companions in case of single planet systems and by close binary companions in case of multi-planet systems. Let us note that such mechanisms could also explain the lack of eccentric orbits found in the formation studies around single stars, like in Sotiriadis et al. (2017), when compared to all the detected exoplanets (see Fig. 5.28).

Several observations of misalignment between the stellar spin axis and the orbital angular momentum of hot Jupiters have been reported (Wright et al., 2011; Albrecht et al., 2012). A classical scenario to explain this misalignment is the Lidov-Kozai cycles associated to a highly inclined binary companion (e.g., Naoz and Fabrycky, 2014). In this work we observed misalignment induced by the nodal precession of the planets due to their interaction with the binary companion, whatever the inclination of the binary companion. Note that this effect was extensively studied during the disk phase (see, e.g., Batygin and Adams, 2013; Lai, 2014; Spalding and Batygin, 2014; Zanazzi and Lai, 2018b) but continues even after the dissipation of the disk (Boué and Fabrycky, 2014). The nodal precession effect could lead to possibly strong misalignments even for planets further away of the star than the hot Jupiters. Note that in this work we considered the spin axis of the star as fixed and parallel to the disk angular momentum at the beginning of the simulation. Of course, it is a strong assumption since the disk would most likely precess before the formation of the giant planets and would be misaligned. Moreover, the spin axis of the host star could also be chaotic and not constant, as shown by Storch et al. (2014) for a primary star under the influence of a hot Jupiter for example.

5.5 Conclusions

In this chapter, we studied the impact of a binary companion on the migration of two giant planets in a protoplanetary disk. The eccentricity and inclination damping induced by the disk, its gravitational potential, and the nodal precession induced by the binary companion on the disk were all considered here. We observed that for a wide binary companion, the gravitational potential of the disk suppressed the impact of the binary companion during the disk phase, as observed in the previous chapter. In addition, the gravitational interaction between the planets which evolve in a mean motion resonance established during their migration in the disk, acts to reduce the impact of the binary companion after the dissipation of the disk.

In a second phase, we studied the impact of the binary companion when reducing its distance to the planets. The influence of the closer binary com-

panion leads to planetary ejections in more than 30% of the simulations during the dynamical evolution of the system after the dispersal of the disk. Those ejections usually leave the remaining planets with high eccentricity. This could give an additional explanation for the existence of many S-type planets detected with high eccentricity values, the other scenario being the influence of a highly inclined binary companion in one-planet systems (see Chapter 4). Note that the existence of a binary companion goes along with possible planetary spin-orbit misalignment due to the nodal precession induced by the companion, as observed in this chapter.

Conclusions and perspectives

In this work, we studied the migration of giant planets in a protoplanetary disk under the influence of a wide binary companion. In the first part of the work, we studied the evolution of a single giant planet while a second planet was added in the system in the second part. To realize this study, we modified the well-known symplectic integrator SyMBA to include a wide binary companion and included the Type-II migration of the planets as well as the eccentricity and inclination damping due to the disk. The disk gravitational potential acting on the planet and the nodal precession induced by the binary companion on the disk were also considered. For this last effect, we derived new approximate formulas for the evolution of the disk's inclination and longitude of the ascending node, in the case of a rigidly precessing disk with a decreasing mass and perturbed by a wide binary companion, which are suitable for N -body simulations. Thousands of simulations were realized with different physical and orbital parameters for the planets and several eccentricity and inclination values for the binary companion.

Regarding the disk phase, we observed that a single planet feels the influence of a highly inclined binary companion through the Lidov-Kozai mechanism when the gravitational potential of the disk is not considered. However, the gravitational and damping forces exerted by the disk on the planet tend to keep the latter in the midplane of the disk and surpass the effect of the binary companion by preventing the planet from getting locked into the Lidov-Kozai resonance during the disk phase. We also confirmed that because of the nodal precession induced by the binary companion, a primordial spin-orbit misalignment could be generated for circumprimary planets with an inclined binary companion. It would be interesting to further investigate the possibility of spin-orbit misalignment in the case of hot Jupiters, for which observations of such misalignment were made. Moreover, we showed that if the influence of the

binary companion surpasses the gravitational influence of the disk, a decoupling between the planets and the disk can occur, as it was illustrated for a binary companion at 250 AU. However, in this case, since the assumptions made on our model could be violated, further investigation is required to confirm the results.

After the dispersal of the disk, we show that a capture in a Lidov-Kozai resonant state is far from automatic when the binary companion star is highly inclined, since only 36% of the single planet systems end up locked in the resonance at the end of the simulations. Nevertheless, in the presence of a highly inclined binary companion, all the planetary evolutions are strongly influenced by the Lidov-Kozai resonance and the non-resonant evolutions present high eccentricity and inclination variations associated with circulation around the Lidov-Kozai islands. In the presence of a second planet in the system, the gravitational interaction between the two giant planets, which evolve in a mean-motion resonance established during their migration in the disk, acts to reduce the impact of the wide binary companion, in particular the establishment of the Lidov-Kozai resonance with the binary companion. However, for closer binary companions, we reported planetary ejections in more than 30% of the simulations, leaving the remaining planets of the system with high eccentricity and potentially inside of Lidov-Kozai in the case of an inclined binary companion. Let us note that in two-planet systems, a coupled nodal precession of the planets induced by the binary companion was observed in the long-term evolution of the system.

Our work sets a framework for the study of the formation of giant planets in binary star systems and their long-term evolution. Nevertheless, several aspects of our modelization require further investigation. The influence of additional effects such as general relativity or stellar oblateness could also be studied, in particular in the case of hot Jupiters. It would also be interesting to investigate the influence of the parameter values of the disk as well as different disk mass models. A possible extension of our work consists in the inclusion of a third planet in the system and the study of the long-term stability of the systems with a chaos detector. This could be achieved with the tool designed and briefly presented in Appendix A. Also a thorough dynamical study of the 3D planetary configurations found in our simulations could be performed. Finally, further analysis of detected binary star systems, like the 55 Cancri system made of 5 planets orbiting a primary star under the influence of a wide binary companion, could be carried out. Since it is currently estimated that about half of the Sun-like stars are part of multiple-star systems, we believe that the complete understanding of the influence of a wide binary companion on the planetary eccentricities and inclinations is very important to fully explain the observational parameter distributions of the exoplanets.

Appendix A

Chaos detector for planetary systems

During the thesis, a collaboration on the long-term stability of single star systems was achieved and consisted in the numerical validation of the analytical results of Volpi et al. (2019). To do so, the implementation of the Mean Exponential Growth factor of Nearby Orbits (MEGNO) chaos detector (Cincotta et al., 2003) was completed in the SyMBA code (for single star systems). We briefly present hereafter the implementation of the MEGNO and the context of the study.

Let $\mathcal{H}(\mathbf{p}, \mathbf{q})$ with $\mathbf{p}, \mathbf{q} \in \mathbb{R}^n$ be an autonomous hamiltonian of n degrees of freedom. The hamiltonian vector field can be expressed as

$$\dot{\mathbf{x}} = J\nabla_{\mathbf{x}}\mathcal{H} \tag{A.1}$$

where $\mathbf{x} = \begin{pmatrix} \mathbf{p} \\ \mathbf{q} \end{pmatrix} \in \mathbb{R}^{2n}$ and $J = \begin{pmatrix} 0_n & -I_n \\ I_n & 0_n \end{pmatrix}$, being I_n and 0_n the identity and null $n \times n$ matrices, respectively. In order to compute the MEGNO chaos indicator, we need to compute the evolution of the deviation vector $\delta(t)$. This vector satisfies the variational equations

$$\dot{\delta}(t) = J\nabla_{\mathbf{x}}^2\mathcal{H}\delta(t), \tag{A.2}$$

being $\nabla_{\mathbf{x}}^2\mathcal{H}$ the Hessian matrix of the hamiltonian. As in Cincotta et al. (2003), the Mean Exponential Growth Factor is defined as

$$Y(t) = \frac{2}{t} \int_0^t \frac{\delta(s)}{\delta(s)} ds \tag{A.3}$$

where $\delta(s)$ is the Euclidian norm of the deviation vector. We also calculated in the code the mean MEGNO, i.e., the time-averaged MEGNO :

$$\bar{Y}(t) = \frac{1}{t} \int_0^t Y(s) ds. \quad (\text{A.4})$$

The limit for $t \rightarrow \infty$ provides a good characterisation of the orbits. In particular,

- $\lim_{t \rightarrow \infty} \bar{Y}(t) = 0$ for stable periodic orbits,
- $\lim_{t \rightarrow \infty} \bar{Y}(t) = 2$ for quasi-periodic orbits and for orbits close to stable periodic ones,
- for irregular orbits, $\bar{Y}(t)$ diverges with time.

To calculate the evolution of the tangent vectors for MEGNO, a big effort was done to keep the symplectic structure of the code. To do so, we first noticed that the system modeling the tangent vectors $\dot{\delta}(t) = J \nabla_{\mathbf{x}}^2 \mathcal{H} \delta(t)$ is Hamiltonian. Indeed, as presented in Libert et al. (2011), using the Hamiltonian $\mathcal{K} = \frac{1}{2} \delta(t)^T \nabla_{\mathbf{x}}^2 \mathcal{H} \delta(t)$, Eq. (A.2) can be written in Hamiltonian equations. Using this structure, we can evolve the system using a symplectic integrator as presented in Chapter 2. Our goal was to merge the evolutions of the system and the tangent vectors to keep the evolution symplectic. Briefly, we first considered the Hamiltonian of the system and the one of the tangent vectors with respect to the moment and then the Hamiltonian of the tangent vector with respect to the positions (see Skokos and Gerlach, 2010, for more details).

Our implementation of the MEGNO chaos detector was successfully used for single star systems. Indeed, to date, more than 600 multi-planetary systems have been discovered, but our knowledge of the systems is usually far from complete due to the limitations of the detection techniques. In particular, for planetary systems discovered with the radial velocity (RV) method, the inclinations of the orbital planes, and thus the mutual inclinations and planetary masses, are unknown. Volpi et al. (2019) constrained the spatial configuration of several RV-detected extrasolar systems. Through an analytical study based on a first-order secular hamiltonian expansion, they identified ranges of values for the orbital inclinations and the mutual inclinations which ensure the long-term stability of the system pursuing the original work of Libert and Tsiganis (2009b). We contributed to this work by performing validation of the analytical results. The time-consuming numerical explorations that we carried out with the MEGNO chaos detector showed the accuracy of the simplified analytical approach up to high mutual inclinations, as it can be observed in Section 4.3 of Volpi et al. (2019) (in particular Fig. 7) that we attach below for the sake of completeness.

The 3D secular dynamics of radial-velocity-detected planetary systems

Mara Volpi, Arnaud Roisin, and Anne-Sophie Libert

Abstract

Aims. To date, more than 600 multi-planetary systems have been discovered. Due to the limitations of the detection methods, our knowledge of the systems is usually far from complete. In particular, for planetary systems discovered with the radial velocity (RV) technique, the inclinations of the orbital planes, and thus the mutual inclinations and planetary masses, are unknown. Our work aims to constrain the spatial configuration of several RV-detected extrasolar systems that are not in a mean-motion resonance.

Methods. Through an analytical study based on a first-order secular Hamiltonian expansion and numerical explorations performed with a chaos detector, we identified ranges of values for the orbital inclinations and the mutual inclinations, which ensure the long-term stability of the system. Our results were validated by comparison with n-body simulations, showing the accuracy of our analytical approach up to high mutual inclinations ($\sim 70^\circ$ - 80°).

Results. We find that, given the current estimations for the parameters of the selected systems, long-term regular evolution of the spatial configurations is observed, for all the systems, i) at low mutual inclinations (typically less than 35°) and ii) at higher mutual inclinations, preferentially if the system is in a Lidov-Kozai resonance. Indeed, a rapid destabilisation of highly mutually inclined orbits is commonly observed, due to the significant chaos that develops around the stability islands of the Lidov-Kozai resonance. The extent of the Lidov-Kozai resonant region is discussed for ten planetary systems (HD 11506, HD 12661, HD 134987, HD 142, HD 154857, HD 164922, HD 169830, HD 207832, HD 4732, and HD 74156).

Key words. celestial mechanics - planets and satellites: dynamical evolution and stability - methods: analytical - planetary systems

1 Introduction

The number of detected multi-planetary systems continually increases. Despite the rising number of discoveries, our knowledge of the physical and orbital parameters of the systems is still partial due to the limitations of the observational techniques. Nevertheless, it is important to acquire a deeper knowledge of the detected extrasolar systems, in particular a more accurate understanding of the architecture of the systems. Regarding the two-planet systems detected via the radial velocity (RV) method, we have fairly precise data about the planetary mass ratio, the semi-major axes, and the eccentricities. However, we have no information either on the orbital inclinations i (i.e. the angles the planetary orbits form with the plane of the sky) – which means that only minimal planetary masses can be inferred – or on the mutual inclination between the planetary orbital planes i_{mut} . This raises questions about possible three-dimensional (3D) configurations of the detected planetary systems. Let us note that a relevant clue to the possible existence of 3D systems has been provided for ν Andromedae c and d , whose mutual inclination between the orbital planes is estimated to be 30° (Deitrick et al., 2015).

A few studies on the dynamics of extrasolar systems have been devoted to the 3D problem. Analytical works by Michtchenko et al. (2006), Libert and Henrard (2007), and Libert and Henrard (2008) investigated the secular evolution of 3D exosystems that are not in a mean-motion resonance. They showed that mutually inclined planetary systems can be long-term stable. In particular, these works focused on the analysis of the equilibria of the 3D planetary three-body problem, showing the generation of stable Lidov-Kozai (LK) equilibria (Lidov, 1962; Kozai, 1962) through bifurcation from a central equilibrium, which itself becomes unstable at high mutual inclination. Thus, around the stability islands of the LK resonance, which offers a secular phase-protection mechanism and ensures the stability of the system, chaotic motion of the planets occurs, limiting the possible 3D configurations of planetary systems.

Using n-body simulations, Libert and Tsiganis (2009a) investigated the possibility that five extrasolar two-planet systems, namely ν Andromedae, HD 12661, HD 169830, HD 74156, and HD 155358, are actually in a LK-resonant state for mutual inclinations in the range $[40^\circ, 60^\circ]$. They showed that the physical and orbital parameters of four of the systems are consistent with a LK-type orbital motion, at some specific values of the mutual inclination, while around 30% – 50% of the simulations generally lead to chaotic motion. The work also suggests that the extent of the LK-resonant region varies significantly for each planetary system considered.

Extensive long-term n-body integrations of five hierarchical multi-planetary systems (HD 11964, HD 38529, HD 108874, HD 168443, and HD 190360) were

performed by Veras and Ford (2010). They showed a wide variety of dynamical behaviour when assuming different inclinations of the orbital plane with respect to the line of sight and mutual inclinations between the orbital planes. They often reported LK oscillations for stable highly inclined systems.

In Dawson and Chiang (2014), the authors presented evidence that several eccentric warm Jupiters discovered with eccentric giant companions are highly mutually inclined (i.e. with a mutual inclination in the range $[35^\circ, 65^\circ]$). For instance, this is the case of the HD 169830 and HD 74156 systems, which will also be discussed in the present work.

Recently, Volpi et al. (2018) used a reverse KAM method (Kolmogorov, 1954; Arnol'd, 1963; Moser, 1962) to estimate the mutual inclinations of several low-eccentric RV-detected extrasolar systems (HD 141399, HD 143761, and HD 40307). This analytical work addressed the long-term stability of planetary systems in a KAM sense, requiring that the algorithm constructing KAM invariant tori is convergent. This demanding condition leads to upper values of the mutual inclinations of the systems close to $\sim 15^\circ$.

In the spirit of Libert and Tsiganis (2009a), the aim of the present work is to determine the possible 3D architectures of RV-detected systems by identifying ranges of values for the mutual inclinations that ensure the long-term stability of the systems. Particular attention will be given to the possibility of the detected extrasolar systems being in a LK-resonant state, since it offers a secular phase-protection mechanism for mutually inclined systems, even though the two orbits may suffer large variations both in eccentricity and inclination. Indeed, the variations occur in a coherent way, such that close approaches do not occur and the system remains stable.

To reduce the number of unknown parameters to take into account, we use an analytical approach, expanding the Hamiltonian of the three-body problem in power series of the eccentricities and inclinations. Being interested in the long-term stability of the system, we consider its secular evolution, averaging the Hamiltonian over the fast angles. Thanks to the adoption of the Laplace plane, we can further reduce the expansion to two degrees of freedom. It was shown in previous works (see for example Libert and Henrard, 2007; Libert and Sansottera, 2013) that if the planetary system is far from a mean-motion resonance, the secular approximation at the first order in the masses is accurate enough to describe the evolution of the system. Such an analytical approach is of interest for the present purpose, since, being faster than pure n -body simulations which also consider small-period effects, it allows us to perform an extensive parametric exploration at a reasonable computational cost. Moreover, in the present work we will show that the analytical expansion is highly reliable, fulfilling its task up to high values of the mutual inclination.

The goal of the present work is twofold. On the one hand, we study the

3D secular dynamics of ten RV-detected extrasolar systems, identifying for each one the values in the parameter space (i_{mut}, i) that induce a LK-resonant behaviour of the system. On the other hand, through numerical explorations performed with a chaos detector, we identify the ranges of values for which a long-term stability of the orbits is observed, unveiling for each system the extent of the chaotic region around the LK stability islands.

The paper is organised as follows. In Sect. 2, we describe the analytical secular approximation and discuss its accuracy to study the 3D dynamics of planetary systems in Sect. 3, as well as the methodology of our parametric study. The question of possible 3D configurations of RV-detected planetary systems is addressed in Sect. 4. Our results are finally summarised in Sect. 5.

2 Analytical secular approximation

We focus on the three-body problem of two exoplanets revolving around a central star. The indexes 0, 1, and 2 refer to the star, the inner planet, and the outer planet, respectively. Since the total angular momentum vector \mathbf{C} is an integral of motion of the problem, we adopt as a reference plane the constant plane orthogonal to \mathbf{C} , the so-called Laplace plane. In this plane, the Hamiltonian formulation of the problem no longer depends on the two angles Ω_1 and Ω_2 , but only on their constant difference $\Omega_1 - \Omega_2 = \pi$. Thus, thanks to the reduction of the nodes, the problem is reduced to four degrees of freedom. We adopt the Poincaré variables,

$$\begin{aligned}\Lambda_i &= \beta_i \sqrt{\mu_i a_i}, & \xi_i &= \sqrt{2\Lambda_i} \sqrt{1 - \sqrt{1 - e_i^2}} \cos \omega_i, \\ \lambda_i &= M_i + \omega_i, & \eta_i &= -\sqrt{2\Lambda_i} \sqrt{1 - \sqrt{1 - e_i^2}} \sin \omega_i,\end{aligned}\tag{1}$$

where a , e , ω , and M refer to the semi-major axis, eccentricity, argument of the pericenter, and mean anomaly, respectively, and with

$$\mu_i = \mathcal{G}(m_0 + m_i), \quad \beta_i = \frac{m_0 m_i}{m_0 + m_i},\tag{2}$$

for $i = 1, 2$. Moreover, we consider the parameter D_2 (as defined in Robutel, 1995)

$$D_2 = \frac{(\Lambda_1 + \Lambda_2)^2 - C^2}{\Lambda_1 \Lambda_2},\tag{3}$$

which measures the difference between the actual norm of the total angular momentum vector \mathbf{C} and the one the system would have if the orbits were circular and coplanar (by definition, D_2 is quadratic in eccentricities and inclinations).

We introduce the translation $L_j = \Lambda_j - \Lambda_j^*$, where Λ_j^* is the value of Λ_j for the observed semi-major axis a_j , for $j = 1, 2$. We then expand the Hamiltonian in power series of the variables \mathbf{L} , $\boldsymbol{\xi}$, $\boldsymbol{\eta}$, and the parameter D_2 and in Fourier series of $\boldsymbol{\lambda}$, as in Volpi et al. (2018),

$$H(D_2, \mathbf{L}, \boldsymbol{\lambda}, \boldsymbol{\xi}, \boldsymbol{\eta}) = \sum_{j_1=1}^{\infty} h_{j_1,0}^{(\text{Kep})}(\mathbf{L}) + \sum_{s=0}^{\infty} \sum_{j_1=0}^{\infty} \sum_{j_2=0}^{\infty} D_2^s h_{s;j_1,j_2}(\mathbf{L}, \boldsymbol{\lambda}, \boldsymbol{\xi}, \boldsymbol{\eta}), \quad (4)$$

where

- $h_{j_1,0}^{(\text{Kep})}$ is a homogeneous polynomial function of degree j_1 in \mathbf{L} ;
- $h_{s;j_1,j_2}$ is a homogeneous polynomial function of degree j_1 in \mathbf{L} , degree j_2 in $\boldsymbol{\xi}$ and $\boldsymbol{\eta}$, and with coefficients that are trigonometric polynomials in $\boldsymbol{\lambda}$.

As we are interested in the secular evolution of the system, the Hamiltonian can be averaged over the fast angles,

$$H(D_2, \boldsymbol{\xi}, \boldsymbol{\eta}) = \sum_{j=0}^{ORDECC/2} \mathcal{C}_{j,m,n} D_2^j \sum_{m+n=0}^{ORDECC-j} \boldsymbol{\xi}^m \boldsymbol{\eta}^n, \quad (5)$$

where *ORDECC* indicates the maximal order in eccentricities considered, here fixed to 12. When the system is far from a mean-motion resonance, such an analytical approach at first order in the masses is accurate enough to describe the secular evolution of extrasolar systems (see for example Libert and Santossera, 2013). The Hamiltonian formulation Eq. (5) has only two degrees of freedom, with the semi-major axes being constant in the secular approach.

3 Parametric study

In the following, we describe the parametric study carried out in the present work. The selection of the systems considered here is described in Sect. 3.1, and the accuracy of the analytical expansion for the secular evolution of the selected systems is discussed in Sect. 3.2.

3.1 Methodology

The present work aims to identify the possible 3D architectures of RV-detected extrasolar systems. From the online database exoplanets.eu, we selected all the two-planet systems that fulfil the following criteria: (a) the period of the inner planet is longer than 45 days (no tidal effects induced by the

star); (b) the semi-major axis of the outer planet is smaller than 10 AU (systems with significant planet-planet interactions); (c) the system is not close to a mean-motion resonance; (d) the planetary eccentricities are lower than 0.65; (e) the masses of the planets are smaller than $10 M_J$. The orbital parameters of the ten selected systems are listed in Table 1, as well as the reference from which they have been derived.

In this work, the secular evolutions of the systems are considered when varying the mutual inclination i_{mut} and the orbital plane inclination i with respect to the plane of the sky. It is important to note that, although the inclinations i_1 and i_2 of the two orbital planes may differ, we decided here to set the same value i for both planes. Thus both masses are varied using the same scaling factor $\sin i$.

In the general reference frame, the following relation holds:

$$\cos i_{mut} = \cos i_1 \cos i_2 + \sin i_1 \sin i_2 \cos \Delta\Omega, \quad (6)$$

being $\Delta\Omega = \Omega_1 - \Omega_2$. It should be noted that Eq. (6) can be solved if $i_{mut} \leq 2i$, thus for a given value of i it determines boundaries for the compatible values of i_{mut} . Since $i_1 = i_2 = i$, having fixed the values of i_{mut} , we can determine the value of the longitudes of the nodes by setting $\Omega_1 = \Delta\Omega$ and $\Omega_2 = 0$, thus obtaining the complete set of initial conditions. A consequent change of coordinates to the Laplace plane is finally performed by using the following relations valid in the Laplace plane:

$$\begin{aligned} \Lambda_1 \sqrt{1 - e_1^2} \cos i_{L1} + \Lambda_2 \sqrt{1 - e_2^2} \cos i_{L2} &= C, \\ \Lambda_1 \sqrt{1 - e_1^2} \sin i_{L1} + \Lambda_2 \sqrt{1 - e_2^2} \sin i_{L2} &= 0, \end{aligned} \quad (7)$$

where i_{L1} and i_{L2} denote the orbital inclinations in the Laplace-plane reference frame.

For our parametric study, we varied the value of the mutual inclination i_{mut} from 0° to 80° with an increasing step of 0.5° , while the common orbital plane inclination i runs from 5° to 90° with an increasing step of 5° . As the coefficients $\mathcal{C}_{j,m,n}$ in Eq. (5) depend on \mathbf{L} , and therefore on the masses of the planets, we recomputed them for each value of i . Regarding the integration of the secular approach, we fixed the integration time to 10^6 yr with an integration step of 1 yr, and the energy preservation was monitored along the integration.

3.2 Accuracy of the analytical approach

Before discussing the results of our parametric study, we need to ensure that the Hamiltonian formulation, Eq. (5), provides an accurate description of the planetary dynamics for all sets of parameters considered in the study,

Table 1 – Orbital parameters of the selected systems.

System	$m \sin i (M_J)$	$M_{\text{Star}} (M_{\odot})$	a	e	ω	References
HD 11506	b 3.44 c 0.82	1.19	2.43 0.639	0.22 0.42	257.8 234.9	Tuomi and Kotiranta (2009)
HD 12661	b 2.3 (± 0.19) c 1.57 (± 0.07)	1.07	0.831 (± 0.048) 2.56 (± 0.17)	0.378 (± 0.0077) 0.031 (± 0.022)	296 (± 1.5) 165 (± 0.0)	Wright et al. (2009)
HD 134987	b 1.59 c 0.82	1.07	0.81 5.8	0.233 0.12	252.7 195	Jones et al. (2010)
HD 142	b 1.25 (± 0.15) c 5.3 (± 0.7)	1.1	1.02 (± 0.03) 6.8 (± 0.5)	0.17 (± 0.06) 0.21 (± 0.07)	327 (± 26) 250 (± 20)	Wittenmyer et al. (2012)
HD 154857	b 2.24 c 2.58	1.718	1.291 5.36	0.46 0.06	57 32	Wittenmyer et al. (2014)
HD 164922	b 0.3385 c 0.0406	0.874	2.115 0.3351	0.126 0.22	129 81	Fulton et al. (2016)
HD 169830	b 2.88 c 4.04	1.4	0.81 3.6	0.31 0.33	148 252	Mayor et al. (2004)
HD 207832	b 0.56 c 0.73	0.94	0.57 2.112	0.13 0.27	130.8 121.6	Haghighipour et al. (2012)
HD 4732	b 2.37 c 2.37	1.74	1.19 4.6	0.13 0.23	35 118	Sato et al. (2013)
HD 74156	b 1.778 c 7.997	1.24	0.2916 3.82	0.638 0.3829	175.35 268.9	Feng et al. (2015)

in particular for high values of the mutual inclination i_{mut} . As already shown in previous papers (e.g. Libert and Henrard (2005) for the coplanar problem, Libert and Henrard (2007) for the 3D problem), the series of the secular terms converge better than the full perturbation. However, the higher the value of D_2 , the weaker the convergence, as expected. In the following, we discuss the numerical convergence of the expansion for the selected extrasolar systems, also called *convergence au sens des astronomes*, as opposed to the mathematical convergence (Poincaré, 1893).

Table 2 lists, for the ten systems, the contributions to the Hamiltonian value of the terms from order 2 to order 12 in eccentricities and inclinations (i.e. $j + m + n$ in Eq. (5)). The entries are the sums of the terms appearing at a given order, computed at the orbital parameters given in Table 1 and at $i = 50^\circ$ and $i_{mut} = 50^\circ$, in order to evaluate the *convergence au sens des astronomes* at high mutual inclination. The numerical convergence of the expansion at high mutual inclination is obvious for most of the systems. However, when the decrease of the terms is less marked, we should keep in mind that results at higher mutual inclinations should be analysed with caution. Moreover, the last column of Table 1 gives an estimation of the remainder of the truncated expansion. It shows the relative error between the secular Hamiltonian computed by numerical quadrature and our polynomial formulation (Eq. 5), confirming the previous observations.

To further illustrate the accuracy of our analytical approach, we show in Fig. 1 the evolutions of HD 12661 given by the analytical expansion (Eq. 5) (red curves) for the mutual inclinations $i_{mut} = 20^\circ, 40^\circ, 50^\circ$, and 80° (i is fixed to 50°), and compare them to the evolutions obtained by the numerical integration of the three-body problem with the SWIFT package (Levison and Duncan (1994), blue curves). Although the numerical convergence observed in Table 2 is not excellent for HD 12661, the agreement of the analytical approach with the numerical integration of the full problem is very good. The dynamical evolutions are well reproduced up to high values of the mutual inclination ($i_{mut} = 20^\circ, 40^\circ, 50^\circ$). Only small differences in the periods are observed and can be attributed to the short-period terms not considered in our secular formulation. For very high values ($i_{mut} = 80^\circ$), the dynamical evolutions given by the two methods no longer coincide, but follow the same trend. As will be shown in Sect. 4.3, the orbits are generally chaotic at such high mutual inclinations.

Table 2 – Convergence *au sens des astronomes* for the ten systems. The value H_j corresponds to the sum of all the terms of the Hamiltonian given by Eq. (5) of order j in eccentricities and inclinations. The last column gives the relative error between the secular Hamiltonian computed by numerical quadrature and the expansion of Eq. (5). The values are computed for the initial condition $(i_{mut}, i) = (50^\circ, 50^\circ)$.

System	H_2	H_4	H_6	H_8	H_{10}	H_{12}	H_{12}/H_2	Relative error
HD 11506	9.47e-06	1.66e-05	6.31e-06	7.15e-06	2.46e-06	4.73e-07	$\mathcal{O}(10^{-2})$	1.62e-04
HD 12661	3.76e-05	7.24e-05	7.33e-05	3.96e-05	9.69e-06	9.25e-07	$\mathcal{O}(10^{-2})$	1.42e-04
HD 134987	4.42e-07	2.61e-08	1.53e-09	1.90e-10	1.09e-11	1.62e-12	$\mathcal{O}(10^{-6})$	1.10e-05
HD 142	4.27e-06	1.67e-06	1.40e-07	1.93e-08	1.58e-09	5.53e-10	$\mathcal{O}(10^{-4})$	1.34e-04
HD 154857	2.67e-05	2.23e-07	1.20e-07	7.54e-08	1.36e-08	2.10e-09	$\mathcal{O}(10^{-4})$	9.33e-05
HD 164922	1.24e-07	9.67e-09	4.53e-10	2.99e-11	5.95e-13	1.41e-13	$\mathcal{O}(10^{-6})$	1.03e-05
HD 169830	7.01e-06	2.40e-05	6.51e-09	7.36e-06	2.75e-06	6.26e-07	$\mathcal{O}(10^{-1})$	1.46e-04
HD 207832	9.15e-07	6.85e-07	2.08e-07	1.79e-07	4.94e-08	6.47e-09	$\mathcal{O}(10^{-2})$	5.28e-05
HD 4732	6.22e-06	1.35e-06	7.42e-08	8.36e-08	1.48e-08	1.44e-09	$\mathcal{O}(10^{-4})$	7.58e-05
HD 74156	2.93e-05	1.65e-05	4.68e-06	5.36e-05	3.24e-05	1.62e-05	$\mathcal{O}(10^{-1})$	1.01e-04

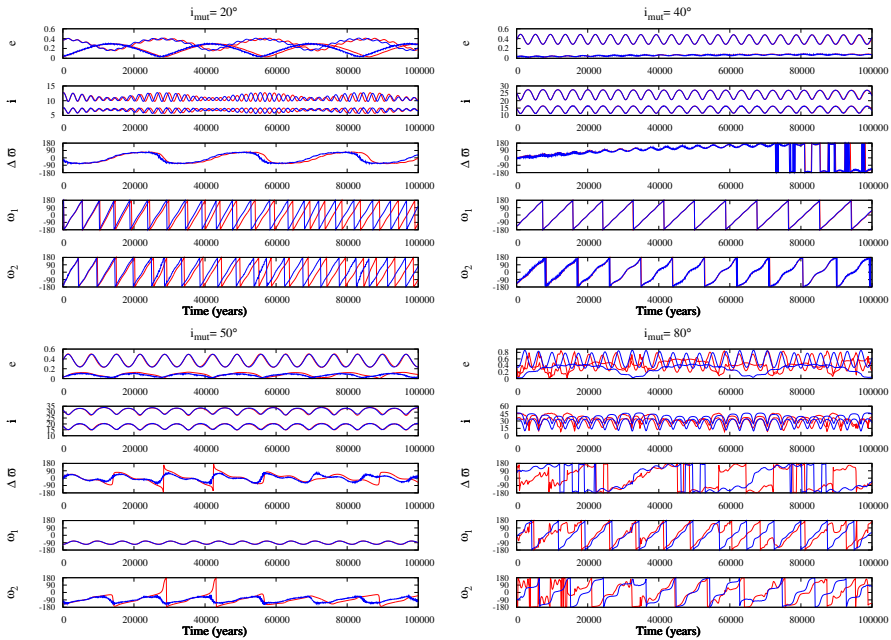


Figure 1 – Dynamical evolutions of HD 12661 system given by the analytical expansion (in red) and by n-body simulations (in blue), for $i_{mut} = 20^\circ$ (top left), 40° (top right), 50° (bottom left), and 80° (bottom right). The inclination of the orbital plane is fixed to $i = 50^\circ$.

4 Results

The question of the 3D secular dynamics of RV-detected planetary systems is addressed here in two directions. Firstly, we focus on identifying the inclination values for which a LK-resonant regime is observed in our parametric study. Secondly, the long-term stability of the mutually inclined systems is unveiled by means of a chaos detector.

4.1 Extent of the Lidov-Kozai regions

Regarding the possible 3D configurations of extrasolar systems, we are particularly interested in the LK resonance. This protective mechanism ensures that the system remains stable, despite large eccentricities and inclination variations. It is characterised, in the Laplace-plane reference frame, by the coupled variation of the eccentricity and the inclination of the inner planet, and the libration of the argument of the pericenter of the same planet around $\pm 90^\circ$ (Lidov, 1962; Kozai, 1962).

As a first example, we investigate the dynamics of the HD 12661 extrasolar system. In the left panel of Fig. 2, we show, for varying (i_{mut}, i) values, the maximal eccentricity of the inner planet reached during the dynamical evolution of the system,

$$\max e_1 = \max_t e_1(t), \quad (8)$$

being $e_1(t)$ the eccentricity of the inner planet at time t . Let us note that this quantity is often used to determine the regularity of planetary orbits, since for low ($e < 0.2$) and high ($e > 0.8$) eccentricity values it is generally found to be in good agreement with chaos indicators (see for instance Funk et al., 2011). On the right panel, we report, for all the considered (i_{mut}, i) values, the libration amplitude of the angle ω_1 , defined as

$$\text{libr_ampl}(\omega_1) = \max_t \omega_1(t) - \min_t \omega_1(t). \quad (9)$$

This value will serve as a guide for the detection of the LK-resonant behaviour characterised by the libration of ω_1 , and thus by a small value of $\text{libr_ampl}(\omega_1)$.

When following an horizontal line in Fig. 2, the mutual inclination i_{mut} varies while the orbital inclination i , and thus the planetary masses, are kept fixed. On the other hand, the inclination of the common orbital plane decreases when moving down along a vertical line, while the planetary masses increase accordingly. As previously stated, this implies the recomputation of the coefficients $\mathcal{C}_{j,m,n}$ of Eq. (5). Let us recall that all (i_{mut}, i) pairs cannot be considered here since, for fixed $i_1 = i_2 = i$ values, Eq. (6) cannot be solved for all the mutual inclinations.

We see that the eccentricity variations of 3D configurations of HD 12661 are small⁽¹⁾ for low mutual inclinations (blue in the left panel of Fig. 2) and become large for high mutual inclinations (red). Additionally, the argument of the pericenter ω_1 circulates for low i_{mut} values (light blue in the right panel of Fig. 2) and librates for high i_{mut} values (dark blue). Thus, for high mutual inclinations, the system is in a LK-resonant state.

To visualise the different dynamics, we draw, for a given D_2 value, the level curves of the Hamiltonian (Eq. 5) in the representative plane $(e_1 \sin \omega_1, e_2 \sin \omega_2)$ where both pericenter arguments are fixed to $\pm 90^\circ$ (see Libert and Henrard (2007) for more details on the representative plane). This plane is neither a phase portrait nor a surface of section, since the problem is four dimensional. However, nearly all the orbits will cross the representative plane at several points of intersection on the same energy curve. Figure 3 shows the representative planes of HD 12661 for $i_{mut} = 20^\circ$ (i.e. $D_2 = 0.35$, left panel), 40° (i.e. $D_2 = 0.67$, middle panel), and 50° (i.e. $D_2 = 0.90$, right panel), the inclination

(1). The initial inner eccentricity is 0.377.

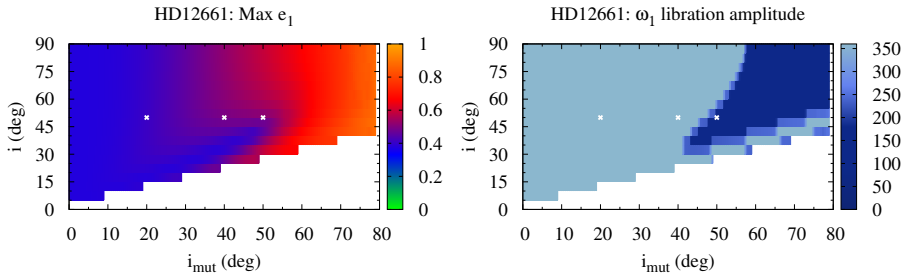


Figure 2 – Long-term evolution of HD 12661 system when varying the mutual inclination i_{mut} (x -axis) and the inclination of the orbital plane i (y -axis), both expressed in degrees. Left panel: Maximal eccentricity of the inner planet, as defined by Eq. (8). Right panel: Libration amplitude of the argument of the pericenter ω_1 (in degrees), as defined by Eq. (9). The three highlighted points are related to the representative planes shown in Fig. 3.

of the orbital plane being fixed to 50° . These three system configurations are also indicated with white crosses in Fig. 2 and their dynamical evolutions are those presented in Fig. 1.

For low values of i_{mut} , circular orbits ($e_1 = e_2 = 0$) constitute a point of stable equilibrium (left panel of Fig. 3). As we increase the mutual inclination (central and right panels of Fig. 3), the central equilibrium becomes unstable and bifurcates into the two stable LK equilibria. The red crosses represent the intersections of the evolution of the mutually inclined HD 12661 system with the representative plane. For low mutual inclinations, the crosses are located on both sides of the representative plane, so the argument of the inner pericenter circulates. For $i_{mut} = 50^\circ$ (right panel of Fig. 3), the crosses are inside the LK island in the left side of the representative plane, associated with the libration of ω_1 around 270° (as can also be observed in the bottom left dynamical evolution shown in Fig. 1). We see that the corresponding white cross on the right side of Fig. 2 is likewise located inside the dark blue region of the LK resonance.

The critical value of the mutual inclination, which corresponds to the change of stability of the central equilibrium, depends on the mass and semi-major axis ratios (see e.g. Libert and Henrard, 2007) and is typically around $40^\circ - 45^\circ$ for mass ratios between 0.5 and 2. For increasing mutual inclinations, the stable LK equilibria reach higher inner eccentricity values and the orbit of the considered system possibly crosses the representative plane inside a LK island. Therefore, the dark blue LK region in Fig. 2 starts around $40^\circ - 55^\circ$, the exact

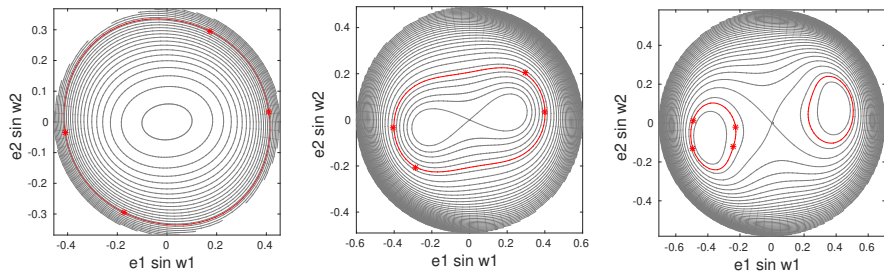


Figure 3 – Representative plane for HD 12661 system, having fixed the inclination of the orbital plane to $i = 50^\circ$, for $i_{mut} = 20^\circ$ (left panel), $i_{mut} = 40^\circ$ (middle panel), and $i_{mut} = 50^\circ$ (right panel). The level curve of Hamiltonian relative to the orbital parameters of HD 12661 is highlighted in red. The crosses indicate the intersections of the orbit with the representative plane.

value for the change of dynamics depending on the inclination of the orbital plane since the expansion (Eq. 5) depends on the inclination i via the planetary mass.

Let us note that, even if the numerical convergence of the analytical expansion of the HD 12661 system is not excellent (see Table 2), the LK-resonant region perfectly matches the one obtained with n-body simulations additionally performed for validation, except at very high mutual inclinations ($i_{mut} \geq 70^\circ$). Indeed, for the HD 12661 and HD 74156 systems, a destabilisation of the orbits is observed at very high mutual inclinations and slightly reduces the stable LK region.

A second example is shown in Fig. 4 for the HD 11506 system. The LK region is now located at smaller mutual inclinations, making visible the right border of the LK region. For each i value, the interval of mutual inclinations associated with the libration of the angle ω_1 begins at $\sim 40^\circ$, whereas its amplitude depends on i . No spatial configuration of HD 11506 can be found in a LK-resonant state for a mutual inclination higher than 65° .

Let us note that some additional dark blue points can be observed for low values of the inclinations of the orbital plane i . These systems are close to the separatrix of the LK resonance and will be destabilised on a longer timescale, as will be shown in the next section.

In Fig. 5 we display the libration amplitude of the argument of the pericenter of the inner planet for the ten systems considered here. All the graphs do show a LK region. In other words, all the selected RV-detected systems, when considered with a significant mutual inclination, have physical and or-

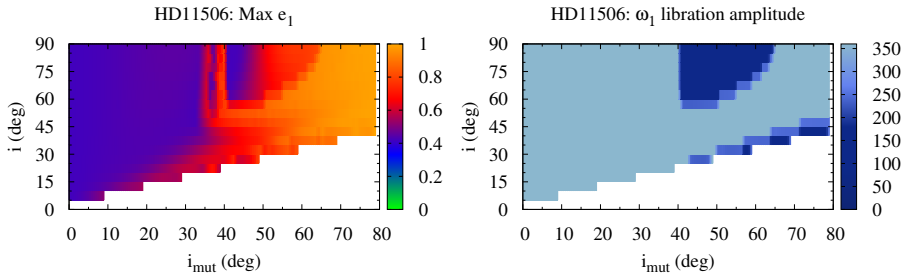


Figure 4 – Same as Fig. 2 for HD 11506 system.

Table 3 – Extent of the LK region for the ten systems. For each system, we indicate the minimum i_{mut} (second column) and i (third column) values of the LK region where libration of ω_1 is observed in Fig. 5, the percentage of initial conditions for which a LK-resonant state is observed (fourth column), and the percentage of initial conditions classified as chaotic by the chaos indicator (fifth column).

System	$\min i_{mut}$ ($^\circ$)	$\min i$ ($^\circ$)	LK (%)	chaos (%)
HD 11506	41	30	15	39
HD 12661	43	30	24	49
HD 134987	46	30	13	–
HD 142	44	30	11	2
HD 154857	41	30	10	2
HD 164922	43	30	23	–
HD 169830	45	25	23	19
HD 207832	50	35	17	20
HD 4732	49	35	12	15
HD 74156	41	30	20	2

bit parameters compatible with a LK-resonant state. Table 3 summarises information on the extent of the LK region for each system. The second and third columns display the minimum values of the mutual inclination i_{mut} (with an accuracy of 1°) and the orbital inclination i , respectively, for which a libration of the argument of the pericenter ω_1 is observed. The percentage of initial conditions inside the (dark blue) LK region is given in the fourth column. The last column reports the percentage of chaos in the whole set of initial conditions and will be discussed in Sect. 4.3.

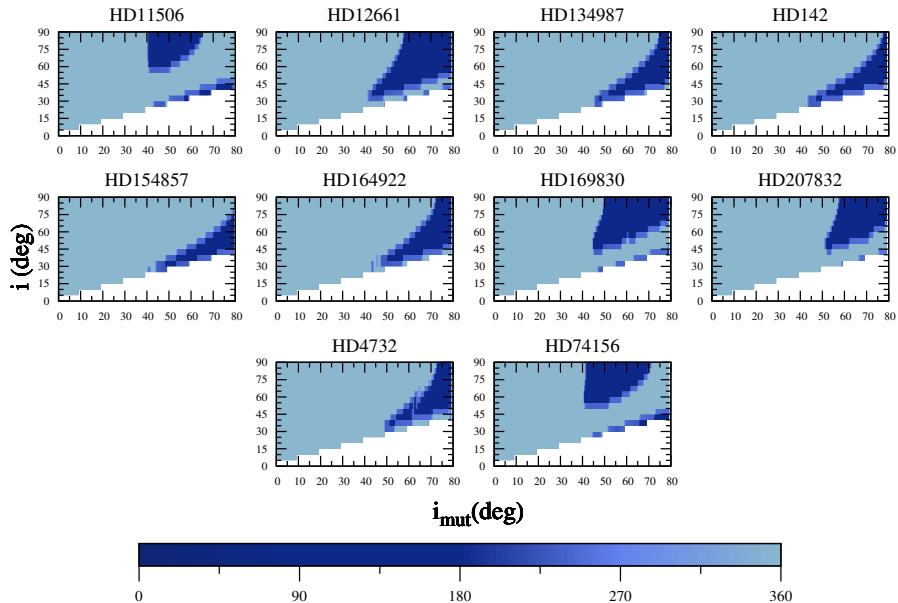


Figure 5 – Libration amplitude of ω_1 for the ten systems considered here, when varying the mutual inclination i_{mut} (x -axis) and the inclination of the orbital plane i (y -axis).

4.2 Sensitivity to observational uncertainties

So far, we have considered the nominal values of the orbital parameters given by the observations. However, due to the limitations of the detection techniques, observational data come with relevant uncertainties, and to explore the influence of such uncertainties on the previous results is relevant. As typical examples, we show in Fig. 6 the extent of the LK region for the HD 12661 and HD 142 systems, when considering extremal orbital parameters within the confidence regions given by the observations, instead of the best-fit parameter values. The errors on each orbital parameter are listed in Table 1 for both planetary systems. Two extremal cases are examined in the following, where the minimal/maximal values are adopted for all the parameters simultaneously.

In the case of the HD 12661 system, the location and extent of the LK region are very similar when adopting the minimal values (top left panel of Fig. 6), the nominal values (top middle), and the maximal values (top right) of the orbital parameters. Concerning HD 142, the situation is quite different. We observe, in the bottom panels of Fig. 6, a significant variation of the LK region

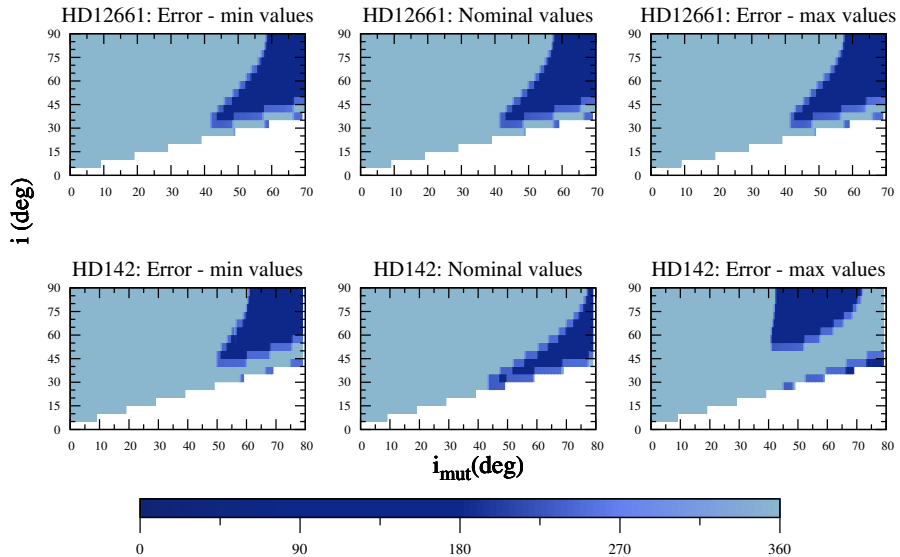


Figure 6 – Libration amplitude of ω_1 , as in Fig. 5, for the HD 12661 (top) and HD 142 (bottom) systems, when considering the minimal values (left), the nominal values (middle), and the maximal values (right) of the orbital parameters.

in its extent and shape, probably due to the greater size of the observational errors on the different orbital elements.

As a result, the location and extent of the LK resonance regions are sensitive to observational uncertainties in the orbital elements, especially when they are significant, and this should be taken into account in detailed studies of the selected systems. Nevertheless, we stress that, when considering extremal values within the confidence regions, the dynamics remains qualitatively the same, with the existence of stable LK islands at high mutual inclinations for both systems.

4.3 Stability of planetary systems

In this section, we aim to determine if the LK-resonant state of a 3D planetary system is essential to ensure its long-term stability. To do so, we have used the Mean Exponential Growth factor of Nearby Orbits (MEGNO) chaos indicator, briefly described in the following (for an extensive discussion on the

properties of the MEGNO, see Cincotta and Simo, 2000; Maffione et al., 2011).

Let $H(\mathbf{p}, \mathbf{q})$ with $\mathbf{p}, \mathbf{q} \in \mathbb{R}^N$ be an autonomous Hamiltonian of N degrees of freedom. The Hamiltonian vector field can be expressed as

$$\dot{\mathbf{x}} = J\nabla_{\mathbf{x}}\mathcal{H}\mathbf{x}, \quad (10)$$

where $\mathbf{x} = \begin{pmatrix} \mathbf{p} \\ \mathbf{q} \end{pmatrix} \in \mathbb{R}^{2N}$ and $J = \begin{bmatrix} 0_N & -1_N \\ 1_N & 0_N \end{bmatrix}$, being 1_N and 0_N the unitary and null $N \times N$ matrices, respectively. In order to apply the MEGNO chaos indicator, we need to compute the evolution of deviation vectors $\boldsymbol{\delta}(t)$. These vectors satisfy the variational equations

$$\dot{\boldsymbol{\delta}}(t) = J\nabla_{\mathbf{x}}^2\mathcal{H}\boldsymbol{\delta}(t), \quad (11)$$

being $\nabla_{\mathbf{x}}^2\mathcal{H}$ the Hessian matrix of the Hamiltonian. As in Cincotta and Simo (2000), the Mean Exponential Growth Factor is defined as

$$Y(t) = \frac{2}{t} \int_0^t \frac{\dot{\delta}(s)}{\delta(s)} ds, \quad (12)$$

where $\delta(s)$ is the Euclidean norm of $\boldsymbol{\delta}(s)$. We consider here the mean MEGNO, that is, the time-averaged MEGNO,

$$\bar{Y}(t) = \frac{1}{t} \int_0^t Y(s) ds. \quad (13)$$

The limit for $t \rightarrow \infty$ provides a good characterisation of the orbits. The MEGNO chaos indicator is particularly convenient since we have:

- $\lim_{t \rightarrow \infty} \bar{Y}(t) = 0$ for stable periodic orbits,
- $\lim_{t \rightarrow \infty} \bar{Y}(t) = 2$ for quasi-periodic orbits and for orbits close to stable periodic ones,
- for irregular orbits, $\bar{Y}(t)$ diverges with time.

For each set of initial conditions we choose the initial deviation vector $\boldsymbol{\delta}(0)$ as a random unitary vector. We then study its evolution along the orbit and compute the corresponding evolution of the mean MEGNO. Two main factors have motivated the choice of this chaos indicator. First, it requires the study of the evolution of only one deviation vector, saving valuable computational time. Second, it returns an absolute value, as it classifies each orbit independently.

As previously noted, the LK-resonant state is surrounded by a chaotic zone associated with the bifurcation of the central equilibrium at null eccentricities. Therefore, a chaos indicator can be useful to highlight the extent of the chaotic zone and identify with precision the (i_{mut}, i) values ensuring the regularity of the orbits for a long time.

On the left panel of Fig. 7, we show the values of the mean MEGNO for HD 11506 computed with our analytical approach. We can appreciate how

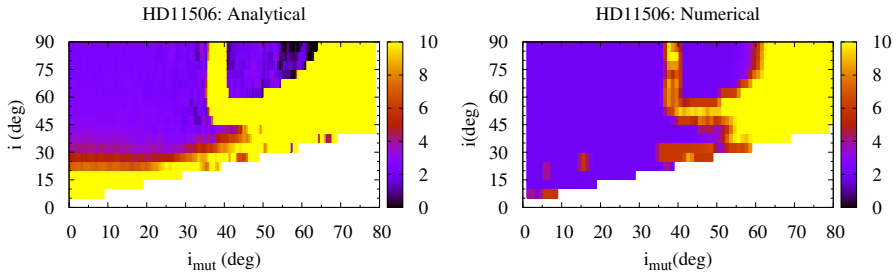


Figure 7 – Mean MEGNO values for the HD 11506 system given by our analytical approach (left panel) and n-body simulations (right panel).

the region at high inclinations characterised as regular by the mean MEGNO (purple) clearly superimposes with the LK-resonant region identified in Fig 4. The surrounding chaotic region displayed in yellow extends up to high mutual inclinations, showing that highly mutually inclined configurations of the HD 11506 system can only be expected in a LK-resonant state. Regarding low mutual inclinations, nearly all spatial configurations present regular motion up to a mutual inclination of $\sim 35^\circ$, where the LK resonance comes into play.

A comparison with n-body simulations (short-period effects included) is given in the right panel of Fig. 7, where numerical integrations have been carried out with SWIFT (for every 1° instead of 0.5° to reduce the computational cost). The two panels look very similar, showing that our secular approach is reliable for systems that are far from a mean-motion resonance.

Similar observations can be made for the ten extrasolar systems considered here. In Fig. 8, the chaotic region associated to a mean MEGNO value greater than eight with our analytical approach, is indicated in white on the plot showing the libration amplitude of ω_1 (Fig. 5). Also, more information on the extent of the chaotic zone for each system can be found in the last column of Table 3. The chaotic region around the stable LK islands is broad for half of the systems (HD 11506, HD 12661, HD 169830, HD 207832, and HD 4732), moderate for the HD 142, HD 15487, and HD 74156 systems, and not significant for the HD 134987 and HD 164922 systems, given the integration timescale and the grid of initial conditions considered. For the first category of systems, long-term regular evolutions of the orbits are only possible for low mutual inclinations and, for higher mutual inclinations, in the LK region, while in the two other cases regular evolutions are also observed at high mutual inclinations outside the LK regions.

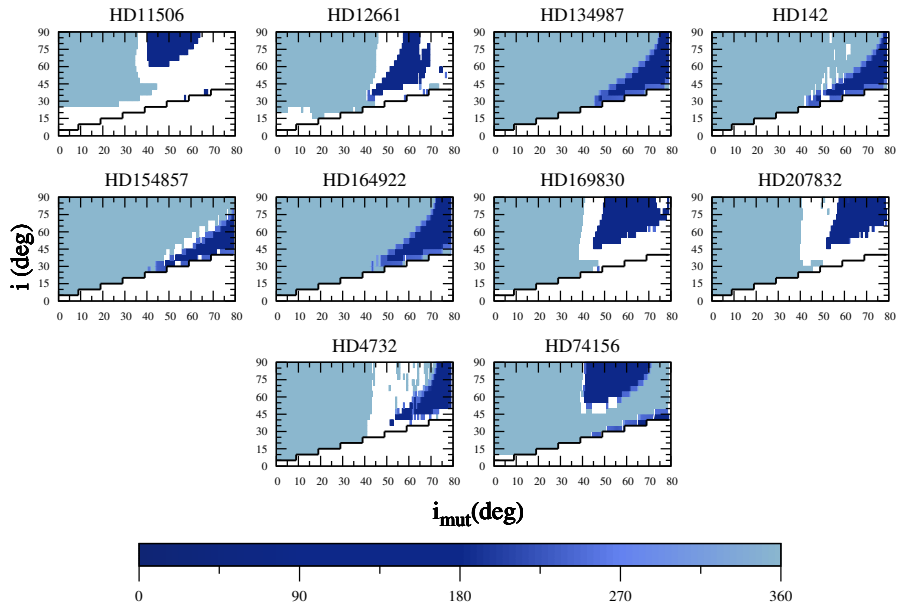


Figure 8 – Same as Fig. 5, where the initial system parameters leading to chaotic motion (defined by the mean MEGNO value greater than 8) are coloured in white (above the black curve).

5 Conclusions

In this work, we studied the possibility for ten RV-detected exoplanetary systems to be in a 3D configuration. Using a secular Hamiltonian approximation (expansion in eccentricities and inclinations), we studied the secular dynamics of possible 3D planetary configurations of the systems. In particular, we determined ranges of orbital and mutual inclinations for which the system is in a LK-resonant state. Our results were compared with n-body simulations, showing the accuracy of the analytical approach up to very high inclinations ($\sim 70^\circ - 80^\circ$). We showed that all the systems considered here might be in a LK-resonant state for a sufficiently mutually inclined orbit. By means of the MEGNO chaos indicator, we revealed the extent of the chaotic zone surrounding the stability islands of the LK resonance. Long-term regular evolutions of the orbits are possible i) at low mutual inclinations and ii) at high mutual inclinations, preferentially in the LK region, due to the significant extent of the chaotic zone in many systems.

It should be stressed that the present work excludes systems whose inner

planet is close to the star. For those systems, relativistic effects have to be considered and we leave for future work how their inclusion will influence the extent of the LK region.

Bibliography

- Abramowitz, M. and Stegun, I. A. (1972). *Handbook of Mathematical Functions*. U.S. Government Printing Office.
- Adams, F. C., Ruden, S. P., and Shu, F. H. (1989). *Eccentric Gravitational Instabilities in Nearly Keplerian Disks*. *The Astrophysical Journal*, 347:959.
- Agol, E. and Fabrycky, D. C. (2018). *Transit-Timing and Duration Variations for the Discovery and Characterization of Exoplanets*, pages 797–816. Springer.
- Albrecht, S., et al. (2012). *Obliquities of Hot Jupiter Host Stars: Evidence for Tidal Interactions and Primordial Misalignments*. *The Astrophysical Journal*, 757(1):18.
- Armitage, P. J. (2009). *Astrophysics of Planet Formation*. Cambridge University Press.
- Armitage, P. J. (2019). *Physical Processes in Protoplanetary Disks*, pages 1–150. Springer Berlin Heidelberg.
- Arnol'd, V. I. (1963). *Proof of a Theorem of A. N. KOLMOGOROV on the Invariance of Quasi-Periodic Motions Under Small Perturbations of the Hamiltonian*. *Russian Mathematical Surveys*, 18:9–36.
- Artymowicz, P. and Lubow, S. H. (1994). *Dynamics of binary-disk interaction. 1: Resonances and disk gap sizes*. *The Astrophysical Journal*, 421:651–667.
- Baruteau, C., et al. (2014). *Planet-Disk Interactions and Early Evolution of Planetary Systems*. In H. Beuther, R. S. Klessen, C. P. Dullemond, and T. Henning, editors, *Protostars and Planets VI*, page 667.

- Bataille, M., Libert, A.-S., and Correia, A. C. M. (2018). *Dynamical evolution of triple-star systems by Lidov–Kozai cycles and tidal friction*. Monthly Notices of the Royal Astronomical Society, 479(4):4749–4759. ISSN 0035-8711.
- Batygin, K. (2012). *A primordial origin for misalignments between stellar spin axes and planetary orbits*. Nature, 491:418–420.
- Batygin, K. and Adams, F. C. (2013). *Magnetic and Gravitational Disk-Star Interactions: An Interdependence of PMS Stellar Rotation Rates and Spin-Orbit Misalignments*. The Astrophysical Journal, 778(2):169.
- Batygin, K., Morbidelli, A., and Tsiganis, K. (2011). *Formation and evolution of planetary systems in presence of highly inclined stellar perturbers*. Astronomy & Astrophysics, 533:A7.
- Bazsó, Á., et al. (2017). *Dynamics and habitability in circumstellar planetary systems of known binary stars*. Monthly Notices of the Royal Astronomical Society, 466:1555–1566.
- Beaugé, C. and Nesvorný, D. (2012). *Multiple-planet Scattering and the Origin of Hot Jupiters*. The Astrophysical Journal, 751(2):119.
- Benacquista, M. (2012). *An Introduction to the Evolution of Single and Binary Stars*. Undergraduate Lecture Notes in Physics. Springer, 2013 edition. ISBN 1441999906,9781441999900.
- Birnstiel, T., Ormel, C. W., and Dullemond, C. P. (2011). *Dust size distributions in coagulation/fragmentation equilibrium: numerical solutions and analytical fits*. Astronomy & Astrophysics, 525:A11.
- Bitsch, B. and Kley, W. (2011). *Evolution of inclined planets in three-dimensional radiative discs*. Astronomy & Astrophysics, 530:A41.
- Bitsch, B., Lambrechts, M., and Johansen, A. (2015). *The growth of planets by pebble accretion in evolving protoplanetary discs*. Astronomy & Astrophysics, 582:A112.
- Bitsch, B., et al. (2013). *Highly inclined and eccentric massive planets. I. Planet-disc interactions*. Astronomy & Astrophysics, 555:A124.
- Bitsch, B., et al. (2018). *Pebble-isolation mass: Scaling law and implications for the formation of super-Earths and gas giants*. Astronomy & Astrophysics, 612:A30.
- Boss, A. P. (1997). *Giant planet formation by gravitational instability*. Science, 276:1836–1839.

- Boss, A. P. (2003). *Rapid Formation of Outer Giant Planets by Disk Instability*. The Astrophysical Journal, 599(1):577–581.
- Boué, G. and Fabrycky, D. C. (2014). *Compact Planetary Systems Perturbed by an Inclined Companion. II. Stellar Spin-Orbit Evolution*. The Astrophysical Journal, 789(2):111.
- Bourbaki, N. (1972). *Eléments de Mathématiques: Groupes et Algèbres de Lie*. Hermann Ed.
- Campbell, B., Walker, G. A. H., and Yang, S. (1988). *A search for substellar companions to solar-type stars*. The Astrophysical Journal, 331:902–921.
- Chambers, J. (2006). *A semi-analytic model for oligarchic growth*. Icarus, 180(2):496–513.
- Chambers, J. E. and Cassen, P. (2002). *The effects of nebula surface density profile and giant-planet eccentricities on planetary accretion in the inner solar system*. Meteoritics & Planetary Science, 37(11):1523–1540.
- Chambers, J. E. and Wetherill, G. W. (1998). *Making the Terrestrial Planets: N-Body Integrations of Planetary Embryos in Three Dimensions*. Icarus, 136(2):304–327.
- Chambers, J. E., Wetherill, G. W., and Boss, A. P. (1996). *The Stability of Multi-Planet Systems*. Icarus, 119(2):261–268.
- Chambers, J. E., et al. (2002). *Symplectic integrator algorithms for modeling planetary accretion in binary star systems*. The Astronomical Journal, 123:2884–2894.
- Chatterjee, S., et al. (2008). *Dynamical Outcomes of Planet-Planet Scattering*. The Astrophysical Journal, 686(1):580–602.
- Chokshi, A., Tielens, A. G. G. M., and Hollenbach, D. (1993). *Dust Coagulation*. The Astrophysical Journal, 407:806.
- Cincotta, P. M., Giordano, C. M., and Simó, C. (2003). *Phase space structure of multi-dimensional systems by means of the mean exponential growth factor of nearby orbits*. Physica D Nonlinear Phenomena, 182(3-4):151–178.
- Cincotta, P. M. and Simo, C. (2000). *Simple tools to study global dynamics in non-axisymmetric galactic potentials - I*. Astronomy and Astrophysics, Supplement, 147(2):205–228. ISSN 0365-0138.

- Cresswell, P., et al. (2007). *On the evolution of eccentric and inclined protoplanets embedded in protoplanetary disks*. *Astronomy & Astrophysics*, 473(1):329–342.
- Crida, A. and Batygin, K. (2014). *Spin-orbit angle distribution and the origin of (mis)aligned hot Jupiters*. *Astronomy & Astrophysics*, 567:A42.
- Crida, A. and Morbidelli, A. (2007). *Cavity opening by a giant planet in a protoplanetary disc and effects on planetary migration*. *Monthly Notices of the Royal Astronomical Society*, 377(3):1324–1336.
- Danby, J. (1988). *Fundamentals of celestial mechanics*. Willmann-Bell, second edition.
- D’Angelo, G. and Lissauer, J. J. (2018). *Formation of Giant Planets*, pages 2319–2344. Springer.
- Dawson, R. I. and Chiang, E. (2014). *A class of warm Jupiters with mutually inclined, apsidally misaligned close friends*. *Science*, 346:212–216.
- Deeg, H. J. and Alonso, R. (2018). *Transit Photometry as an Exoplanet Discovery Method*, pages 633–658. Springer.
- Deitrick, R., et al. (2015). *The Three-dimensional Architecture of the ν Andromedae Planetary System*. *The Astrophysical Journal*, 798(1):46.
- Dominik, C. and Tielens, A. G. G. M. (1997). *The physics of dust coagulation and the structure of dust aggregates in space*. *The Astrophysical Journal*, 480(2):647–673.
- Duncan, M. J., Levison, H. F., and Lee, M. H. (1998). *A Multiple Time Step Symplectic Algorithm for Integrating Close Encounters*. *The Astronomical Journal*, 116:2067–2077.
- Duquennoy, A. and Mayor, M. (1991). *Multiplicity among solar-type stars in the solar neighbourhood. II - Distribution of the orbital elements in an unbiased sample*. *Astronomy & Astrophysics*, 248:485–524.
- Eggleton, P. and Kiseleva, L. (1995). *An Empirical Condition for Stability of Hierarchical Triple Systems*. *The Astrophysical Journal*, 455:640.
- Fabrycky, D. and Tremaine, S. (2007). *Shrinking binary and planetary orbits by kozai cycles with tidal friction*. *The Astrophysical Journal*, 669(2):1298–1315.
- Feng, Y. K., et al. (2015). *The California Planet Survey IV: A Planet Orbiting the Giant Star HD 145934 and Updates to Seven Systems with Long-period Planets*. *The Astrophysical Journal*, 800:22.

- Fisher, R. T. (2004). *A Turbulent Interstellar Medium Origin of the Binary Period Distribution*. The Astrophysical Journal, 600(2):769–780.
- Fu, W., Lubow, S. H., and Martin, R. G. (2015). *The Kozai-Lidov Mechanism in Hydrodynamical Disks. II. Effects of Binary and Disk Parameters*. The Astrophysical Journal, 807(1):75.
- Fulton, B. J., et al. (2016). *Three Temperate Neptunes Orbiting Nearby Stars*. The Astrophysical Journal, 830:46.
- Funk, B., et al. (2011). *On the influence of the Kozai mechanism in habitable zones of extrasolar planetary systems*. Astronomy & Astrophysics, 526:A98.
- Garaud, P. and Lin, D. N. C. (2007). *The effect of internal dissipation and surface irradiation on the structure of disks and the location of the snow line around sun-like stars*. The Astrophysical Journal, 654(1):606–624.
- Girichidis, P., et al. (2020). *Physical Processes in Star Formation*. Space Science Reviews, 216(4):68.
- Gladman, B. (1993). *Dynamics of Systems of Two Close Planets*. Icarus, 106(1):247–263.
- Goldreich, P. and Tremaine, S. (1979). *The excitation of density waves at the Lindblad and corotation resonances by an external potential*. The Astrophysical Journal, 233:857–871.
- Goldreich, P. and Tremaine, S. (1980). *Disk-satellite interactions*. The Astrophysical Journal, 241:425–441.
- Goldreich, P. and Ward, W. R. (1973). *The Formation of Planetesimals*. The Astrophysical Journal, 183:1051–1062.
- Gomes, R., et al. (2005). *Origin of the cataclysmic Late Heavy Bombardment period of the terrestrial planets*. Nature, 435(7041):466–469.
- Goodwin, S. P., Whitworth, A. P., and Ward-Thompson, D. (2004). *Simulating star formation in molecular cloud cores. I. The influence of low levels of turbulence on fragmentation and multiplicity*. Astronomy & Astrophysics, 414:633–650.
- Gorti, U., Hollenbach, D., and Dullemond, C. P. (2015). *The Impact of Dust Evolution and Photoevaporation on Disk Dispersal*. The Astrophysical Journal, 804(1):29.
- Greenberg, R., et al. (1978). *Planetesimals to planets: Numerical simulation of collisional evolution*. Icarus, 35(1):1–26.

- Haghighipour, N. (2010). Planets in Binary Star Systems, volume 366. Springer.
- Haghighipour, N. and Raymond, S. N. (2007). *Habitable Planet Formation in Binary Planetary Systems*. The Astrophysical Journal, 666:436–446.
- Haghighipour, N., et al. (2012). *The Lick-Carnegie Survey: A New Two-planet System around the Star HD 207832*. The Astrophysical Journal, 756:91.
- Hahn, J. M. (2003). *The Secular Evolution of the Primordial Kuiper Belt*. The Astrophysical Journal, 595(1):531–549.
- Hatzes, A. P., et al. (2003). *A Planetary Companion to γ Cephei A*. The Astrophysical Journal, 599:1383–1394.
- He, M. Y. and Petrovich, C. (2018). *On the stability and collisions in triple stellar systems*. Monthly Notices of the Royal Astronomical Society, 474(1):20–31.
- Helled, R., et al. (2014). *Giant Planet Formation, Evolution, and Internal Structure*. In H. Beuther, R. S. Klessen, C. P. Dullemond, and T. Henning, editors, Protostars and Planets VI, page 643.
- Holman, M. J. and Wiegert, P. A. (1999). *Long-term stability of planets in binary systems*. The Astronomical Journal, 117(1):621.
- Huré, J.-M. and Hersant, F. (2011). *The newtonian potential of thin disks*. Astronomy & Astrophysics, 531:A36.
- Innanen, K. A., et al. (1997). *The Kozai Mechanism and the Stability of Planetary Orbits in Binary Star Systems*. The Astronomical Journal, 113:1915.
- Ivanov, P. B., Papaloizou, J. C. B., and Polnarev, A. G. (1999). *The evolution of a supermassive binary caused by an accretion disc*. Monthly Notices of the Royal Astronomical Society, 307(1):79–90.
- Izidoro, A. and Raymond, S. N. (2018). Formation of Terrestrial Planets, pages 2365–2424. Springer.
- Johansen, A. and Lacerda, P. (2010). *Prograde rotation of protoplanets by accretion of pebbles in a gaseous environment*. Monthly Notices of the Royal Astronomical Society, 404(1):475–485.
- Johansen, A., et al. (2014). *The Multifaceted Planetesimal Formation Process*. In H. Beuther, R. S. Klessen, C. P. Dullemond, and T. Henning, editors, Protostars and Planets VI, page 547.

- Johansen, A., et al. (2015). *Growth of asteroids, planetary embryos, and Kuiper belt objects by chondrule accretion*. *Science Advances*, 1:1500109.
- Jones, H. R. A., et al. (2010). *A long-period planet orbiting a nearby Sun-like star*. *Monthly Notices of the Royal Astronomical Society*, 403:1703–1713.
- Jurić, M. and Tremaine, S. (2008). *Dynamical Origin of Extrasolar Planet Eccentricity Distribution*. *The Astrophysical Journal*, 686(1):603–620.
- Kaib, N. A., Raymond, S. N., and Duncan, M. (2013). *Planetary system disruption by Galactic perturbations to wide binary stars*. *Nature*, 493:381–384.
- Kiseleva, L. G., Eggleton, P. P., and Mikkola, S. (1998). *Tidal friction in triple stars*. *Monthly Notices of the Royal Astronomical Society*, 300(1):292–302.
- Kley, W. and Haghighipour, N. (2014). *Modeling circumbinary planets: The case of Kepler-38*. *Astronomy & Astrophysics*, 564:A72.
- Kokubo, E. and Ida, S. (1998). *Oligarchic Growth of Protoplanets*. *Icarus*, 131(1):171–178.
- Kokubo, E. and Ida, S. (2000). *Formation of Protoplanets from Planetesimals in the Solar Nebula*. *Icarus*, 143(1):15–27.
- Kolmogorov, A. N. (1954). *On preservation of conditionally periodic motions under a small change in the Hamiltonian function*. *Dokl. Akad. Nauk SSSR*, 98(4):527–530.
- Kozai, Y. (1962). *Secular perturbations of asteroids with high inclination and eccentricity*. *The Astronomical Journal*, 67:591.
- Kraus, A. L. and Ireland, M. J. (2012). *LkCa 15: A Young Exoplanet Caught at Formation?* *The Astrophysical Journal*, 745:5.
- Krijt, S., et al. (2015). *Erosion and the limits to planetesimal growth*. *Astronomy & Astrophysics*, 574:A83.
- Krijt, S., et al. (2016). *A panoptic model for planetesimal formation and pebble delivery*. *Astronomy & Astrophysics*, 586:A20.
- Lai, D. (2014). *Star-disc-binary interactions in protoplanetary disc systems and primordial spin-orbit misalignments*. *Monthly Notices of the Royal Astronomical Society*, 440(4):3532–3544.
- Lambrechts, M. and Johansen, A. (2012). *Rapid growth of gas-giant cores by pebble accretion*. *Astronomy & Astrophysics*, 544:A32.

- Larwood, J. D., et al. (1996). *The tidally induced warping, precession and truncation of accretion discs in binary systems: three-dimensional simulations*. Monthly Notices of the Royal Astronomical Society, 282(2):597–613.
- Laskar, J. and Robutel, P. (2001). *High order symplectic integrators for perturbed hamiltonian systems*. Celestial Mechanics and Dynamical Astronomy, 80:39–62.
- Lee, M. H. and Peale, S. J. (2002). *Dynamics and origin of the 2:1 orbital resonances of the GJ 876 planets*. The Astrophysical Journal, 567:596–609.
- Lega, E., Morbidelli, A., and Nesvorný, D. (2013). *Early dynamical instabilities in the giant planet systems*. Monthly Notices of the Royal Astronomical Society, 431(4):3494–3500.
- Levison, H. and Morbidelli, A. (2007). *Models of the collisional damping scenario for ice giant planets and kuiper belt formation*. Icarus, 189:196–212.
- Levison, H. F. and Agnor, C. (2003). *The role of giant planets in terrestrial planet formation*. The Astronomical Journal, 125(5):2692–2713.
- Levison, H. F. and Duncan, M. J. (1994). *The long-term dynamical behavior of short-period comets*. Icarus, 108:18–36.
- Levison, H. F. and Duncan, M. J. (2000). *Symplectically Integrating Close Encounters with the Sun*. The Astronomical Journal, 120(4):2117–2123.
- Libert, A.-S. and Henrard, J. (2005). *Analytical Approach to the Secular Behaviour of Exoplanetary Systems*. Celestial Mechanics and Dynamical Astronomy, 93:187–200.
- Libert, A.-S. and Henrard, J. (2007). *Exoplanetary systems: The role of an equilibrium at high mutual inclination in shaping the global behavior of the 3-D secular planetary three-body problem*. Icarus, 191:469–485.
- Libert, A.-S. and Henrard, J. (2008). *Secular frequencies of 3-D exoplanetary systems*. Celestial Mechanics and Dynamical Astronomy, 100:209–229.
- Libert, A.-S., Hubaux, C., and Carletti, T. (2011). *The Global Symplectic Integrator: an efficient tool for stability studies of dynamical systems. Application to the Kozai resonance in the restricted three-body problem*. Monthly Notices of the Royal Astronomical Society, 414:659–667.
- Libert, A.-S. and Sansottera, M. (2013). *On the extension of the Laplace-Lagrange secular theory to order two in the masses for extrasolar systems*. Celestial Mechanics and Dynamical Astronomy, 117:149–168.

- Libert, A.-S., Sotiriadis, S., and Antoniadou, K. I. (2018). *Influence of periodic orbits on the formation of giant planetary systems*. *Celestial Mechanics and Dynamical Astronomy*, 130(2):19.
- Libert, A. S. and Tsiganis, K. (2009a). *Kozai resonance in extrasolar systems*. *Astronomy & Astrophysics*, 493:677–686. ISSN 0004-6361.
- Libert, A. S. and Tsiganis, K. (2009b). *Trapping in high-order orbital resonances and inclination excitation in extrasolar systems*. *Monthly Notices of the Royal Astronomical Society*, 400(3):1373–1382.
- Libert, A. S. and Tsiganis, K. (2011a). *Formation of '3D' multiplanet systems by dynamical disruption of multiple-resonance configurations*. *Monthly Notices of the Royal Astronomical Society*, 412(4):2353–2360.
- Libert, A.-S. and Tsiganis, K. (2011b). *Trapping in three-planet resonances during gas-driven migration*. *Celestial Mechanics and Dynamical Astronomy*, 111(1-2):201–218.
- Lidov, M. L. (1962). *The evolution of orbits of artificial satellites of planets under the action of gravitational perturbations of external bodies*. *Planetary Space Science*, 9:719–759.
- Lin, D. N. C. and Papaloizou, J. (1986a). *On the Tidal Interaction between Protoplanets and the Primordial Solar Nebula. II. Self-Consistent Nonlinear Interaction*. *The Astrophysical Journal*, 307:395.
- Lin, D. N. C. and Papaloizou, J. (1986b). *On the Tidal Interaction between Protoplanets and the Protoplanetary Disk. III. Orbital Migration of Protoplanets*. *The Astrophysical Journal*, 309:846.
- Lissauer, J. J. (1993). *Planet formation*. *Annual Review of Astronomy & Astrophysics*, 31:129–174.
- Lubow, S. H. and Martin, R. G. (2016). *The Evolution of Planet-Disk Systems that are Mildly Inclined to the Orbit of a Binary Companion*. *The Astrophysical Journal*, 817:30.
- Lubow, S. H. and Ogilvie, G. I. (2001). *Secular Interactions between Inclined Planets and a Gaseous Disk*. *The Astrophysical Journal*, 560(2):997–1009.
- Maffione, N. P., Giordano, C. M., and Cincotta, P. M. (2011). *Testing a fast dynamical indicator: The MEGNO*. *International Journal of Non-Linear Mechanics*, 46(1):23–34. ISSN 00207462.

- Mamajek, E. E. (2009). *Initial Conditions of Planet Formation: Lifetimes of Primordial Disks*. In T. Usuda, M. Tamura, and M. Ishii, editors, *Exoplanets and Disks: Their Formation and Diversity*, volume 1158 of *American Institute of Physics Conference Series*, pages 3–10.
- Marchal, C. and Bozis, G. (1982). *Hill Stability and Distance Curves for the General Three-Body Problem*. *Celestial Mechanics*, 26(3):311–333.
- Mardling, R. A. and Aarseth, S. J. (2001). *Tidal interactions in star cluster simulations*. *Monthly Notices of the Royal Astronomical Society*, 321(3):398–420.
- Martin, R. G., et al. (2014). *The Kozai-Lidov Mechanism in Hydrodynamical Disks*. *Astrophysical Journal Letters*, 792:L33.
- Martin, R. G., et al. (2016). *Planet-disc evolution and the formation of Kozai-Lidov planets*. *Monthly Notices of the Royal Astronomical Society*, 458:4345–4353.
- Marzari, F., Baruteau, C., and Scholl, H. (2010). *Planet-planet scattering in circumstellar gas disks*. *Astronomy & Astrophysics*, 514:L4.
- Marzari, F. and Gallina, G. (2016). *Stability of multiplanet systems in binaries*. *Astronomy & Astrophysics*, 594:A89.
- Marzari, F., et al. (2005). *Jumping Jupiters in Binary Star Systems*. *The Astrophysical Journal*, 618:502–511.
- Matsumoto, Y., Nagasawa, M., and Ida, S. (2012). *The orbital stability of planets trapped in the first-order mean-motion resonances*. *Icarus*, 221(2):624–631.
- Mayor, M., et al. (2004). *The CORALIE survey for southern extra-solar planets. XII. Orbital solutions for 16 extra-solar planets discovered with CORALIE*. *Astronomy & Astrophysics*, 415:391–402.
- McKee, C. F. and Ostriker, E. C. (2007). *Theory of Star Formation*. *Annual Review of Astronomy & Astrophysics*, 45(1):565–687.
- Michtchenko, T. A., Ferraz-Mello, S., and Beaugé, C. (2006). *Modeling the 3-D secular planetary three-body problem. Discussion on the outer ν Andromedae planetary system*. *Icarus*, 181(2):555–571. ISSN 00191035.
- Moorhead, A. and Ford, E. B. (2009). *Type II Migration of Planets on Eccentric Orbits*. In *Bulletin of the American Astronomical Society*, volume 41, page 895. American Astronomical society.

- Morbidelli, A., et al. (2005). *Chaotic capture of Jupiter's Trojan asteroids in the early Solar System*. *Nature*, 435(7041):462–465.
- Morbidelli, A., et al. (2012). *Building Terrestrial Planets*. *Annual Review of Earth and Planetary Sciences*, 40(1):251–275.
- Morbidelli, A., et al. (2016). *Fossilized condensation lines in the Solar System protoplanetary disk*. *Icarus*, 267:368–376.
- Moser, J. (1962). *On invariant curves of area-preserving mapping of an annulus*. *Matematika*, 6(5):51–68.
- Murray, C. D. and Dermott, S. F. (1999). *Solar system dynamics*. Cambridge University Press.
- Mustill, A. J. and Wyatt, M. C. (2011). *A general model of resonance capture in planetary systems: first- and second-order resonances*. *Monthly Notices of the Royal Astronomical Society*, 413(1):554–572.
- Naoz, S. and Fabrycky, D. C. (2014). *Mergers and Obliquities in Stellar Triples*. *The Astrophysical Journal*, 793(2):137.
- Nelson, R. P., et al. (2000). *The migration and growth of protoplanets in protostellar discs*. *Monthly Notices of the Royal Astronomical Society*, 318(1):18–36. ISSN 0035-8711.
- Oka, A., Nakamoto, T., and Ida, S. (2011). *Evolution of Snow Line in Optically Thick Protoplanetary Disks: Effects of Water Ice Opacity and Dust Grain Size*. *The Astrophysical Journal*, 738(2):141.
- Ormel, C. W. and Klahr, H. H. (2010). *The effect of gas drag on the growth of protoplanets. Analytical expressions for the accretion of small bodies in laminar disks*. *Astronomy & Astrophysics*, 520:A43.
- Papaloizou, J. C. B. and Larwood, J. D. (2000). *On the orbital evolution and growth of protoplanets embedded in a gaseous disc*. *Monthly Notices of the Royal Astronomical Society*, 315:823–833.
- Papaloizou, J. C. B., Nelson, R. P., and Masset, F. (2001). *Orbital eccentricity growth through disc-companion tidal interaction*. *Astronomy & Astrophysics*, 366:263–275.
- Papaloizou, J. C. B. and Terquem, C. (1995). *On the dynamics of tilted discs around young stars*. *Monthly Notices of the Royal Astronomical Society*, 274(4):987–1001.

- Peale, S. J. (1976). *Orbital resonance in the solar system*. Annual Review of Astronomy & Astrophysics, 14:215–246.
- Picogna, G. and Marzari, F. (2015). *Decoupling of a giant planet from its disk in an inclined binary system*. Astronomy & Astrophysics, 583:A133.
- Pilat-Lohinger, E., Funk, B., and Dvorak, R. (2003). *Stability limits in double stars. A study of inclined planetary orbits*. Astronomy & Astrophysics, 400:1085–1094.
- Poincaré, H. (1893). Les méthodes nouvelles de la mécanique céleste: Méthodes de MM. Newcomb, Glydén, Lindstedt et Bohlin. 1893. Les méthodes nouvelles de la mécanique céleste. Gauthier-Villars et fils.
- Pollack, J. B., et al. (1996). *Formation of the Giant Planets by Concurrent Accretion of Solids and Gas*. Icarus, 124(1):62–85.
- Press, W. H., et al. (1992). Numerical recipes in fortran 77. The art of scientific computing, pages 718–726. Press Syndicate of the University of Cambridge, deuxième édition.
- Queloz, D., et al. (2000). *The CORALIE survey for southern extra-solar planets. I. A planet orbiting the star Gliese 86*. Astronomy & Astrophysics, 354:99–102.
- Quillen, A. C. (2006). *Reducing the probability of capture into resonance*. Monthly Notices of the Royal Astronomical Society, 365(4):1367–1382.
- Quintana, E. V., et al. (2007). *Terrestrial planet formation around individual stars within binary star systems*. The Astrophysical Journal, 660(1):807.
- Rabl, G. and Dvorak, R. (1988). *Satellite-type planetary orbits in double stars - A numerical approach*. Astronomy & Astrophysics, 191:385–391.
- Rafikov, R. R. and Silsbee, K. (2015). *Planet Formation in Stellar Binaries. I. Planetesimal Dynamics in Massive Protoplanetary Disks*. The Astrophysical Journal, 798:69.
- Raghavan, D., et al. (2010). *A Survey of Stellar Families: Multiplicity of Solar-type Stars*. The Astrophysical Journal Supplement, 190:1–42.
- Rasio, F. A. and Ford, E. B. (1996). *Dynamical instabilities and the formation of extrasolar planetary systems*. Science, 274:954–956.
- Rauch, K. P. and Holman, M. (1999). *Dynamical Chaos in the Wisdom-Holman Integrator: Origins and Solutions*. The Astronomical Journal, 117(2):1087–1102.

- Raymond, S. N. (2006). *The Search for Other Earths: Limits on the Giant Planet Orbits That Allow Habitable Terrestrial Planets to Form*. *Astrophysical Journal Letters*, 643(2):L131–L134.
- Raymond, S. N., Quinn, T., and Lunine, J. I. (2004). *Making other earths: dynamical simulations of terrestrial planet formation and water delivery*. *Icarus*, 168(1):1–17.
- Rein, H. (2012). *A proposal for community driven and decentralized astronomical databases and the Open Exoplanet Catalogue*. arXiv e-prints, arXiv:1211.7121.
- Robutel, P. (1995). *Stability of the planetary three-body problem*. *Celestial Mechanics & Dynamical Astronomy*, 62(3):219–261. ISSN 0923-2958.
- Roisin, A. (2017). Développement d’un intégrateur symplectique pour les systèmes binaires. Application à la formation des systèmes de planètes géantes. Master’s thesis, University of Namur.
- Roisin, A. and Libert, A. S. (2021). *Evolution of a migrating giant planet in the presence of an inclined binary companion*. *Astronomy & Astrophysics*, 645:A138.
- Safronov, V. S. (1972). Evolution of the protoplanetary cloud and formation of the Earth and the planets. Israel Program for Scientific Translations.
- Sato, B., et al. (2013). *A Double Planetary System around the Evolved Intermediate-mass Star HD 4732*. *The Astrophysical Journal*, 762:9.
- Savonije, G. J., Papaloizou, J. C. B., and Lin, D. N. C. (1994). *On tidally induced shocks in accretion discs in close binary systems*. *Monthly Notices of the Royal Astronomical Society*, 268(1):13–28.
- Schwarz, R., et al. (2016). *New prospects for observing and cataloguing exoplanets in well-detached binaries*. *Monthly Notices of the Royal Astronomical Society*, 460(4):3598–3609.
- Shakura, N. I. and Sunyaev, R. A. (1973). *Black holes in binary systems. Observational appearance*. *Astronomy & Astrophysics*, 24:337–355.
- Shu, F. H., Adams, F. C., and Lizano, S. (1987). *Star formation in molecular clouds: observation and theory*. *Annual Review of Astronomy & Astrophysics*, 25:23–81.
- Skokos, C. and Gerlach, E. (2010). *Numerical integration of variational equations*. *Physical Review E*, 82(3):036704.

- Snellgrove, M. D., Papaloizou, J. C. B., and Nelson, R. P. (2001). *On disc driven inward migration of resonantly coupled planets with application to the system around GJ876*. *Astronomy & Astrophysics*, 374:1092–1099.
- Sotiriadis, S. (2017). *Formation of non-coplanar planetary systems*. Ph.D. thesis, University of Namur.
- Sotiriadis, S. and Libert, A.-S. (2020). *Inclination-type resonance in two-planet systems*. *Monthly Notices of the Royal Astronomical Society*, 495(1):192–198.
- Sotiriadis, S., Libert, A.-S., and Raymond, S. N. (2018). *Formation of terrestrial planets in eccentric and inclined giant planet systems*. *Astronomy & Astrophysics*, 613:A59.
- Sotiriadis, S., et al. (2017). *Highly inclined and eccentric massive planets. II. Planet-planet interactions during the disc phase*. *Astronomy & Astrophysics*, 598:A70.
- Spalding, C. and Batygin, K. (2014). *Early Excitation of Spin-Orbit Misalignments in Close-in Planetary Systems*. *The Astrophysical Journal*, 790(1):42.
- Storch, N. I., Anderson, K. R., and Lai, D. (2014). *Chaotic dynamics of stellar spin in binaries and the production of misaligned hot Jupiters*. *Science*, 345(6202):1317–1321.
- Takeda, G., Kita, R., and Rasio, F. A. (2008). *Planetary Systems in Binaries. I. Dynamical Classification*. *The Astrophysical Journal*, 683(2):1063–1075.
- Tanaka, H. and Ward, W. R. (2004). *Three-dimensional Interaction between a Planet and an Isothermal Gaseous Disk. II. Eccentricity Waves and Bending Waves*. *The Astrophysical Journal*, 602(1):388–395.
- Terquem, C. (2013). *The effects of disc warping on the inclination of planetary orbits*. *Monthly Notices of the Royal Astronomical Society*, 435(1):798–808.
- Terquem, C. and Ajmia, A. (2010). *Eccentricity pumping of a planet on an inclined orbit by a disc*. *Monthly Notices of the Royal Astronomical Society*, 404(1):409–414.
- Testi, L., et al. (2014). *Dust Evolution in Protoplanetary Disks*. In H. Beuther, R. S. Klessen, C. P. Dullemond, and T. Henning, editors, *Protostars and Planets VI*, page 339.
- Teyssandier, J. and Terquem, C. (2014). *Evolution of eccentricity and orbital inclination of migrating planets in 2:1 mean motion resonance*. *Monthly Notices of the Royal Astronomical Society*, 443(1):568–583.

- Teyssandier, J., Terquem, C., and Papaloizou, J. C. B. (2013). *Orbital evolution of a planet on an inclined orbit interacting with a disc*. Monthly Notices of the Royal Astronomical Society, 428(1):658–669.
- Thebault, P. and Haghighipour, N. (2015). Planet Formation in Binaries, pages 309–340. Springer.
- Thébault, P., Marzari, F., and Scholl, H. (2006). *Relative velocities among accreting planetesimals in binary systems: The circumprimary case*. Icarus, 183:193–206.
- Thommes, E. W. and Lissauer, J. J. (2003). *Resonant Inclination Excitation of Migrating Giant Planets*. The Astrophysical Journal, 597(1):566–580.
- Tokovinin, A. (2001). *Statistics of multiple stars: some clues to formation mechanisms*. In H. Zinnecker and R. Mathieu, editors, The Formation of Binary Stars, volume 200 of *IAU Symposium*, pages 84–92.
- Tokovinin, A. (2014). *From Binaries to Multiples. II. Hierarchical Multiplicity of F and G Dwarfs*. The Astronomical Journal, 147:87.
- Tokovinin, A. A. (1997). *MSC - a catalogue of physical multiple stars*. Astronomy and Astrophysics Supplement Series, 124:75–84.
- Tsiganis, K., et al. (2005). *Origin of the orbital architecture of the giant planets of the Solar System*. Nature, 435(7041):459–461.
- Tuomi, M. and Kotiranta, S. (2009). *Bayesian analysis of the radial velocities of HD 11506 reveals another planetary companion*. Astronomy & Astrophysics, 496:L13–L16.
- Veras, D. and Ford, E. B. (2010). *Secular Orbital Dynamics of Hierarchical Two-planet Systems*. The Astrophysical Journal, 715:803–822.
- Volpi, M., Locatelli, U., and Sansottera, M. (2018). *A reverse KAM method to estimate unknown mutual inclinations in exoplanetary systems*. Celestial Mechanics and Dynamical Astronomy, 130:36.
- Volpi, M., Roisin, A., and Libert, A.-S. (2019). *The 3D secular dynamics of radial-velocity-detected planetary systems*. Astronomy & Astrophysics, 626:A74.
- Wada, K., et al. (2009). *Collisional Growth Conditions for Dust Aggregates*. The Astrophysical Journal, 702(2):1490–1501.

- Walsh, K. J., et al. (2012). *Populating the asteroid belt from two parent source regions due to the migration of giant planets—“The Grand Tack”*. *Meteoritics and Planetary Science*, 47(12):1941–1947.
- Ward, W. R. (1997). *Protoplanet Migration by Nebula Tides*. *Icarus*, 126(2):261–281.
- Weidenschilling, S. J. (1977). *The Distribution of Mass in the Planetary System and Solar Nebula*. *Astrophysics and Space Science*, 51(1):153–158.
- Weidenschilling, S. J. and Marzari, F. (1996). *Gravitational scattering as a possible origin for giant planets at small stellar distances*. *Nature*, 384(6610):619–621.
- Williams, J. P. and Cieza, L. A. (2011). *Protoplanetary Disks and Their Evolution*. *Annual Review of Astronomy & Astrophysics*, 49(1):67–117.
- Winn, J. N. (2010). *Transits and Occultations*, pages 55–78. University of Arizona Press.
- Wisdom, J. and Holman, M. (1991). *Symplectic maps for the N-body problem*. *The Astronomical Journal*, 102:1528–1538.
- Wittenmyer, R. A., et al. (2012). *The Anglo-Australian Planet Search. XXII. Two New Multi-planet Systems*. *The Astrophysical Journal*, 753:169.
- Wittenmyer, R. A., et al. (2014). *The Anglo-Australian Planet Search. XXIII. Two New Jupiter Analogs*. *The Astrophysical Journal*, 783:103.
- Wright, J. T. (2018). *Radial Velocities as an Exoplanet Discovery Method*, pages 619–632. Springer.
- Wright, J. T., et al. (2009). *Ten New and Updated Multiplanet Systems and a Survey of Exoplanetary Systems*. *The Astrophysical Journal*, 693:1084–1099.
- Wright, J. T., et al. (2011). *The Exoplanet Orbit Database*. *Publications of the Astronomical Society of the Pacific*, 123(902):412.
- Wu, Y. and Murray, N. (2003). *Planet Migration and Binary Companions: The Case of HD 80606b*. *The Astrophysical Journal*, 589(1):605–614.
- Xiang-Gruess, M. and Papaloizou, J. C. B. (2013). *Interaction between massive planets on inclined orbits and circumstellar discs*. *Monthly Notices of the Royal Astronomical Society*, 431(2):1320–1336.

- Xiang-Gruess, M. and Papaloizou, J. C. B. (2014). *Evolution of a disc-planet system with a binary companion on an inclined orbit*. Monthly Notices of the Royal Astronomical Society, 440:1179–1192.
- Xu, Z., Bai, X.-N., and Murray-Clay, R. A. (2017). *Pebble Accretion in Turbulent Protoplanetary Disks*. The Astrophysical Journal, 847(1):52.
- Yoshida, H. (1990). *Construction of higher order symplectic integrators*. Physics Letter A, 150:262–268.
- Youdin, A. N. and Shu, F. H. (2002). *Planetesimal Formation by Gravitational Instability*. The Astrophysical Journal, 580(1):494–505.
- Zanazzi, J. J. and Lai, D. (2017). *Lidov-Kozai Mechanism in Hydrodynamical Disks: Linear Stability Analysis*. Monthly Notices of the Royal Astronomical Society, 467(2):1957–1964.
- Zanazzi, J. J. and Lai, D. (2018a). *Effects of disc warping on the inclination evolution of star-disc-binary systems*. Monthly Notices of the Royal Astronomical Society, 477(4):5207–5219.
- Zanazzi, J. J. and Lai, D. (2018b). *Planet formation in discs with inclined binary companions: can primordial spin-orbit misalignment be produced?* Monthly Notices of the Royal Astronomical Society, 478(1):835–851.
- Zhou, J.-L. and Sun, Y.-S. (2003). *Occurrence and Stability of Apsidal Resonance in Multiple Planetary Systems*. The Astrophysical Journal, 598(2):1290–1300.
- Zsom, A., et al. (2010). *The outcome of protoplanetary dust growth: pebbles, boulders, or planetesimals? II. Introducing the bouncing barrier*. Astronomy & Astrophysics, 513:A57.